MASARYKOVA UNIVERZITA
Přírodovědecká fakulta
Ústav teoretické fyziky a astrofyziky

Diplomová práce

Brno 2023 Daniel Jadlovský

MASARYKOVA
UNIVERZITA
PŘÍRODOVĚDECKÁ FAKULTA
ÚSTAV TEORETICKÉ FYZIKY A ASTROFYZIKY

Studium proměnnosti spektra Betelgeuze

Diplomová práce

Daniel Jadlovský

Vedoucí práce: prof. Mgr. Jiří Krtička, Ph.D. **Brno 2023**

Bibliografický záznam

Autor:	Daniel Jadlovský Přírodovědecká fakulta, Masarykova univerzita Ústav teoretické fyziky a astrofyziky
Název práce:	Studium proměnnosti spektra Betelgeuze
Studijní program:	PřF N-FYZ Fyzika
Studijní obor:	PřF ASTRO Astrofyzika
Vedoucí práce:	prof. Mgr. Jiří Krtička, Ph.D.
Akademický rok:	2022/2023
Počet stran:	xvi + 82
Klíčová slova:	Betelgeuse; červení veleobři; tomografie; pulzace; konvekce; rázové vlny; metody: spektroskopie, fotometrie

Bibliographic Entry

Author:	Daniel Jadlovský Faculty of Science, Masaryk University Department of Theoretical Physics and Astrophysics
Title of Thesis:	Analysis of spectral variability of Betelgeuse
Degree Programme:	PřF N-FYZ Physics
Field of Study:	PřF ASTRO Astrophysics
Supervisor:	prof. Mgr. Jiří Krtička, Ph.D.
Academic Year:	2022/2023
Number of Pages:	xvi + 82
Keywords:	Betelgeuse; red supergiants; tomography; pulsations; convection; shock waves; techniques: spectroscopic, photometric

Abstrakt

Červení veleobři jsou klíčovou součástí chemického vývoje vesmíru. I přesto mnoho otázek ohledně jejich vývoje zůstává nezodpovězených. Jedním z nejjasnějších a nejstudovanějších objektů je Betelegeuse, veleobr se složitou proměnností, který měl v únoru 2020 historické minimum jasnosti. I přesto, že se jasnost později vrátila do původních hodnot, chování tohoto veleobra zůstává silně bezprecedentní. Naším úmyslem je použít fotometrická a spektroskopická pozorování tohoto veleobra pro zkoumání dlouhodobého vývoje jeho atmosféry, za účelem porozumění procesů, které způsobují různé typy proměnnosti červených veleobrů, ale také vysvětlení historického minima jasnosti.

Výsledky diplomové práce jsou rozděleny do dvou publikací. V prvním článku analyzujeme mnoho archivních spekter a fotometrických pozorování. Potvrzujeme, že proměnosti jasnosti a fotosférické rychlosti jsou svázány, zatímco radiální rychlosti určené z ultrafialové oblasti, které přisuzujeme rychlosti hvězdného větru blízko povrchu, vykazují proměnnost na delších časových škálách a mají nejvyšší absolutní hodnoty během historického minima. Ve druhém článku aplikujeme tomografickou metodu, která nám umožňuje zkoumat různé vrstvy hvězdné atmosféry. Pro tento účel používáme zhruba 2500 spekter z posledních 15 let, pozorovaných robotickým teleskopem STELLA na observatoři Izaña (Tenerife, Španělsko). Díky takovému velkému množství dat a tomografické metodě jsme byli schopni studovat vývoj různých vrstev atmosféry Betelgeuse v bezprecedentním detailu a odhalit šíření silných rázových vln během historického minima jasnosti. V důsledku této události byla atmosféra excitována do vyššího módu pulzací, přičemž, poněkud překvapivě, ne synchronně ve všech vrstvách atmosféry.

Abstract

Red supergiants are a key component in evolution of the Universe, yet many questions about their evolution are still not answered. One of the brightest and most intensively studied objects is Betelgeuse, a supergiant with complex variability, which underwent a historical minimum of brightness in February 2020, named the Great Dimming. Even though the brightness has returned to the values prior to the Dimming within months, it continues to exhibit highly unprecedented behavior. Our intention is to use photometric and spectroscropic data to analyse the long-term evolution of atmosphere of Betelgeuse, in order to unveil the physical processes that drive the different modes of variability in red supergiants and to be able to explain the Dimming.

The results of this diploma thesis are divided into two papers. In the first paper, we analyse various archival spectra and photometric data. We confirm that the variability of brightness and photospheric radial velocity is connected to each other, whereas the radial velocity determined from near ultraviolet region, which we attribute to the velocities at the base of outflowing stellar wind, shows longer periods of variability with a maximum of stellar wind velocity during the Dimming. In the second paper, we apply a tomographic method, which allows probing different layers in the stellar atmosphere. For that purpose, we use about 2500 spectra from the past 15 years, observed with the STELLA robotic telescope in Izaña observatory (Tenerife, Spain). Due to this large data sample and the tomographic method, we were able to analyse the variability of different layers in Betelgeuse's atmosphere in an unprecedented detail and unveil propagation of shock waves during the Dimming event. In result of this event, the mode of pulsations was excited to a higher overtone, but, quite extraordinarily, not synchronously in all layers.

MASARYKOVA UNIVERZITA
PŘÍRODOVĚDECKÁ FAKULTA
KOTLÁŘSKÁ 2, 611 37 BRNO
IČ: 00216224
DIČ: CZ00216224

ZADÁNÍ DIPLOMOVÉ PRÁCE

Akademický rok: 2022/2023

Ústav:	Ústav teoretické fyziky a astrofyziky
Student:	Bc. Daniel Jadlovský
Program:	Fyzika
Specializace:	Astrofyzika

Ředitel *ústavu* PřF MU Vám ve smyslu Studijního a zkušebního řádu MU určuje diplomovou práci s názvem:

Název práce:	Studium proměnnosti spektra Betelgeuze
Název práce anglicky:	Analysis of spectral variability of Betelgeuse
Jazyk závěrečné práce:	angličtina

Oficiální zadání:
Červený veleobr Betelgeuze vykazuje proměnnost v mnohých spektrálních oborech. Klíčem k pochopení této proměnnosti je studium změn radiálních rychlostí této hvězdy. Cílem práce je určení radiálních rychlostí jednotlivých částí atmosféry hvězdy, což umožní studium šíření vln a přinese lepší znalost příčin proměnnosti veleobra.
Literatura:

- Dupree, A. K., et al., 2020, ApJ, 899, 68
- Kravchenko, K., et al., 2021, A&A, 650, L17
- van Loon, J. Th.: EAS Publications Series, 2013, 60, 307

Vedoucí práce:	prof. Mgr. Jiří Krtička, Ph.D.
Konzultant:	doc. RNDr. Vladimír Štefl, CSc.
Datum zadání práce:	29. 10. 2021
V Brně dne:	6. 12. 2022

Zadání bylo schváleno prostřednictvím IS MU.

Bc. Daniel Jadlovský, 16. 12. 2021
prof. Mgr. Jiří Krtička, Ph.D., 7. 1. 2022
Mgr. Dušan Hemzal, Ph.D., 25. 1. 2022

Acknowledgments

First and foremost, I would like to express my gratitude to my supervisor prof. Jiří Krtička, Ph.D., for his continued unrelenting support and guidance. I would like to thank Dr. Thomas Granzer from Leibniz Institute for Astrophysics Postdam for making it possible to come for an internship, which became the key research component of this diploma thesis. Moreover, I would also like to thank other people in Postdam for their help, namely, Dr. Michael Weber a prof. Dr. Klaus Strassmeier. Last but not least, I am very grateful to Dr. Kateryna Kravchenko from Max Planck Institute for Extraterrestrial Physics for her significant and very active contribution.

Furthermore, I would like to thank other co-authors of both articles, as well as the referees. Finally yet importantly, finishing this thesis would not be possible without help from friends and other students in Postdam and Brno, and mainly without the support of my family.

Additionally, I would also like to thank Melissa Pisteljic from University of Zurich for proofreading the thesis.

Declaration

Hereby I declare that I have prepared my diploma thesis independently under the guidance of the supervisor with the use of cited works.

Brno, May 2023

. . . . . .

Daniel Jadlovský

Contents

Introduction **1**

1. Observational Properties of Red Supergiants **3**
1.1 Physical Properties 3
1.1.1 Identification and Hertzsprung-Russell Diagram 4
1.2 Mass Loss and Dust Production 6
1.2.1 Observations 7
1.2.2 Empirical $\dot{M} - L$ Relations 10
1.2.3 Current Day Theories 11
1.3 Variability 11
1.3.1 Fundamental Mode 13
1.3.2 Long Secondary Period 13

2. Model Atmospheres of Red Supergiants **15**
2.1 Fundamental Physical Concepts 15
2.1.1 Hydrodynamical Equations 15
2.1.2 Stellar Atmospheres 16
2.2 Radiatively Driven Stellar Winds 19
2.2.1 Isothermal Winds 19
2.2.2 Dust-driven Winds 20
2.2.3 Other Types of Stellar Wind 23
2.3 Convection 24
2.3.1 Schwarzschild and Ledoux Criterion 25
2.3.2 Mixing-Length Theory 25
2.3.3 Convection in Red Supergiants 26
2.4 Radial Pulsations 28
2.4.1 Non-adiabatic Oscillations 29
2.5 Simulations 30

3. The Tomographic Method **33**
3.1 Aims of the Method 33
3.1.1 Schwarzschild Scenario 33
3.2 Development 33
3.2.1 First Results 33

3.2.2 Validation 36
3.3 Application 37
3.3.1 Line-depth Contribution Function 37
3.3.2 Construction of Numerical Masks 38
3.3.3 Mask Cross-correlation 38

4. Summary of Results 41
4.1 Paper I: Analysis of photometric and spectroscopic variability of Betelgeuse 41
4.2 Paper II: The Great Dimming of Betelgeuse: the photosphere as revealed by tomography during the past 15 years 42

Conclusion and Future Insights 45

Appendix A 47

Appendix B 59

Bibliography 75

Introduction

Red supergiants lose a significant fraction of their mass during their evolution, while in their cores heavier elements than helium are produced. Additionally, red supergiants may explode as a core-collapse supernova, fusing elements even heavier than iron. In consequence, these stars significantly contribute to the chemical enrichment of interstellar medium and the Universe as a whole, whilst the expelled material may be used for formation of new generations of stars and planets. Furthermore, the heavier elements are essential building blocks of life as we know it.

Recent progress in modelling, simulations and observations of these objects provide us with new fascinating insights into the evolution of supergiants. Despite that, the physics behind the mass-loss process is still poorly understood, as well as the exact evolution towards a supernova explosion. Therefore, a further study of these objects is required, in order to properly connect the red supergiants with the results of their evolution.

For this purpose, in this work we select a magnificent red supergiant Betelgeuse, which is one of the brightest stars on the sky, as well as a star with the second largest angular diameter, surpassed only by the Sun itself. In the beginning of 2020, this remarkable supergiant suffered an unprecedented Great Dimming, when the brightness of Betelgeuse dropped the most significantly in the long history of observations. Even though later the supergiant returned to its previous values of brightness, its behaviour continues to be be unprecedented nonetheless and the Dimming itself is still not sufficiently explained. Therefore, in this work we study the Dimming event and what followed it, as well as overall variability of the star and its connection to mass loss.

In the first part of the theoretical part, we give an overview of observational properties of red supergiants, primarily based on compilation of various sources from scientific journals, as up to this date such overviews have been very sparse in the scientific community. In the second part, we describe the physical processes that are relevant in atmospheres and extended envelopes of red supergiants as well as correlate them with recent models and observations, while a special focus is devoted to processes that we deal with in our two articles, such as the mechanism of mass loss. In the third part, we describe the recently validated tomographic method. This method allows us to study different layers of stellar atmospheres.

The practical part of the thesis consists of two contributions, one published in a scientific journal, while the other one is currently in preparation. The first paper is the continuation of our previous research, i.e., the analysis of archival ultraviolet spectra, primarily from spectrographs onboard Hubble Space Telescope, as well as optical spectra from various ground based instruments. We improve upon previous results and connect the radial velocity variability with processes in atmospheres of Betelgeuse, namely the stellar wind.

The second contribution is based on the internship in Leibniz Institute for Astrophysics Postdam (AIP), which sparked a new collaboration, leading to the second paper. As part of this research we analyse an enormous dataset of Betelgeuse spectra, which was observed by means of the STELLA telescope. Combined with the tomographic method, we are able to unveil motions in the atmosphere of Betelgeuse in an astounding detail. This enables us to reveal many new details related to the variability of Betelgeuse, and in extension to other red supergiants. Moreover, it provides new insights related to the Great Dimming itself.

Chapter 1

Observational Properties of Red Supergiants

1.1 Physical Properties

Red supergiants (RSG) are variable evolved massive stars that burn helium in their cores. The progenitors are hot massive stars in a range of mass M from $\approx 8\,\mathrm{M}_\odot$ to $\approx 40\,\mathrm{M}_\odot$. During the main-sequence evolution, these stars are burning hydrogen in their cores, primarily via carbon-nitrogen-oxygen (CNO) cycle. The energy output is enough to sustain main sequence phase for about $10^6 - 10^7$ yr. Once the supply of hydrogen in the core is exhausted, the post-main-sequence evolution begins. The star continues to burn hydrogen in the shell surrounding the helium core, while the star evolves nearly horizontally across the Hertzsprung-Russell (HR) diagram for about $10^3 - 10^5$ yr as a yellow supergiant. Once the temperature T in the core is high enough to ignite helium burning, the star becomes a RSG star (Massey 2003; Levesque 2010, 2017; Kippenhahn et al. 2013). Figure 1.1 shows the evolution of single stars in the HR diagram.

There appears to exist an upper mass limit of $\approx 25\,\mathrm{M}_\odot$ for stars that end its evolution as RSGs, primarily due to the Eddington limit (see Section 2.3.3). The stars expand its radius R to $\approx 100 - 1000\,\mathrm{R}_\odot$, becoming some of the physically largest stars, and thus its effective temperature T_{eff} cools down to $\approx 3500 - 4000\,\mathrm{K}$, placing the stars amongst the spectral types K and M (Levesque 2017). Low surface gravity of RSGs makes it easier for material to escape from their surface through various mechanisms. Consequently, the mass-loss rates $\dot{M}$ are indeed very high, with the highest rates between 10^{-6} and $10^{-4}\,\mathrm{M}_\odot\,\mathrm{yr}^{-1}$. Red supergiants are the most luminous cool stars, with bolometric luminosities L between $2 \cdot 10^4$ and $6 \cdot 10^5\,\mathrm{L}_\odot$ (Mauron & Josselin 2011). Figure 1.2 shows positions of massive stars in the HR diagram with evolutionary tracks.

After the departure from the main sequence and especially during the RSG phase, massive stars lose a significant fraction of their mass, sometimes even up to half of their initial mass, being an essential asset to the enrichment of interstellar medium (ISM). A significant portion of this mass is lost during the RSG phase. Due to their low surface temperature, the material can condensate into dust particles relatively close to the star. In result of the mass loss, the RSG stars are often being veiled in shells of circumstellar medium (Levesque 2017).

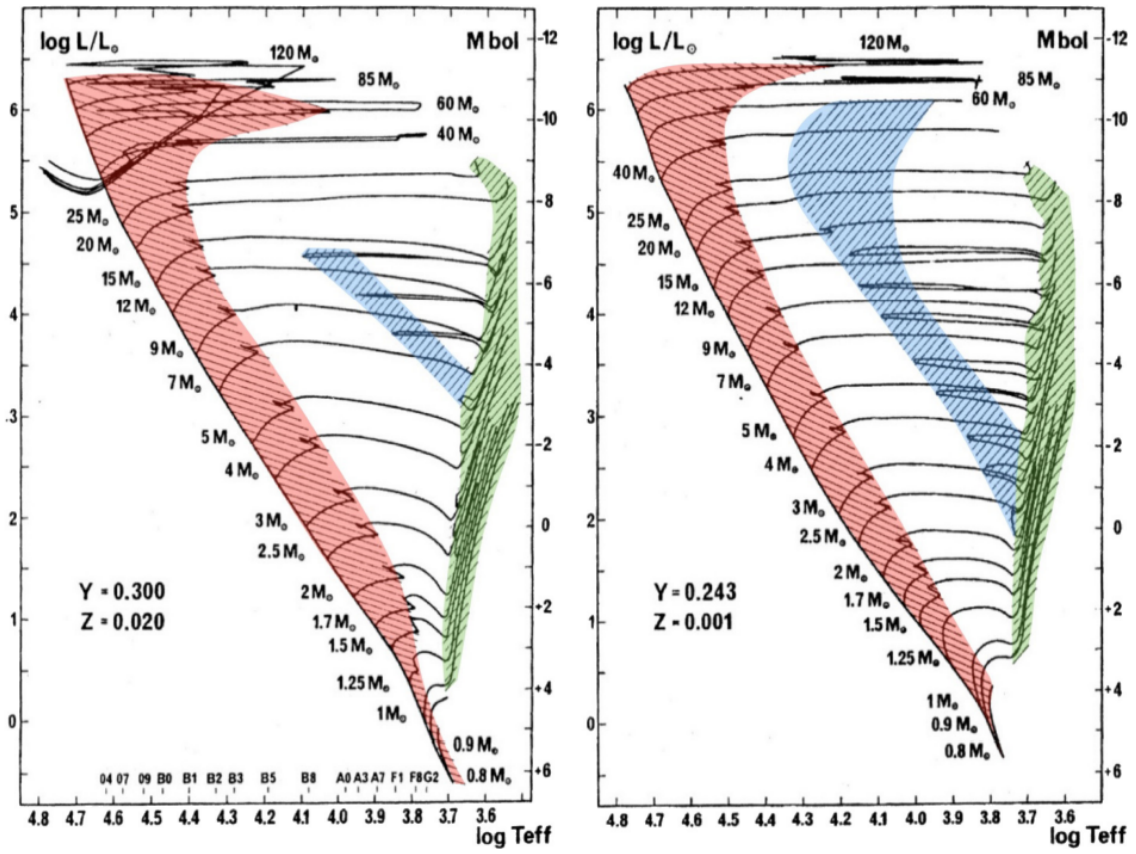

Figure 1.1: Evolutionary tracks of stars in the HR diagram above for metallicities $Z = 0.02$ (left panel) and $Z = 0.001$ (right panel). The colored regions indicate core H fusion (red), core He fusion (blue), and He or later core fusion phases (green). Adapted from Lamers & Levesque (2017) and Schaller et al. (1992).

From this point, the evolution of a RSG star seems to continue in two main ways. Low-mass RSG stars continue to burn heavier elements in their cores, until an iron core is formed. Then the star ends its RSG phase as core-collapse hydrogen-rich supernova Type II-P, leaving behind a newly formed neutron star or a black hole. On the other hand, high-mass RSG stars may lose enough mass to evolve back to yellow, and even blue supergiants, performing a blue loop (even more massive stars never cool enough to become a RSG star in the first place). Then they explode either as a blue supergiant or Wolf-Rayet star (Levesque 2010, 2017; Kippenhahn et al. 2013; Meynet et al. 2015). The exact evolution of a RSG star is determined primarily by initial mass and mass-loss rate, but also by rotation, metallicity and for example, whether such a star is part of a binary system.

1.1.1 Identification and Hertzsprung-Russell Diagram

Red supergiants are sometimes not easily distinguished from red giants, specifically the ones on the asymptotic giant branch (AGB), which includes Mira variables, as the most luminous AGB stars may occupy similar position in the HR diagram, despite the fact that from the evolutionary and internal physical structure point of view, these objects are

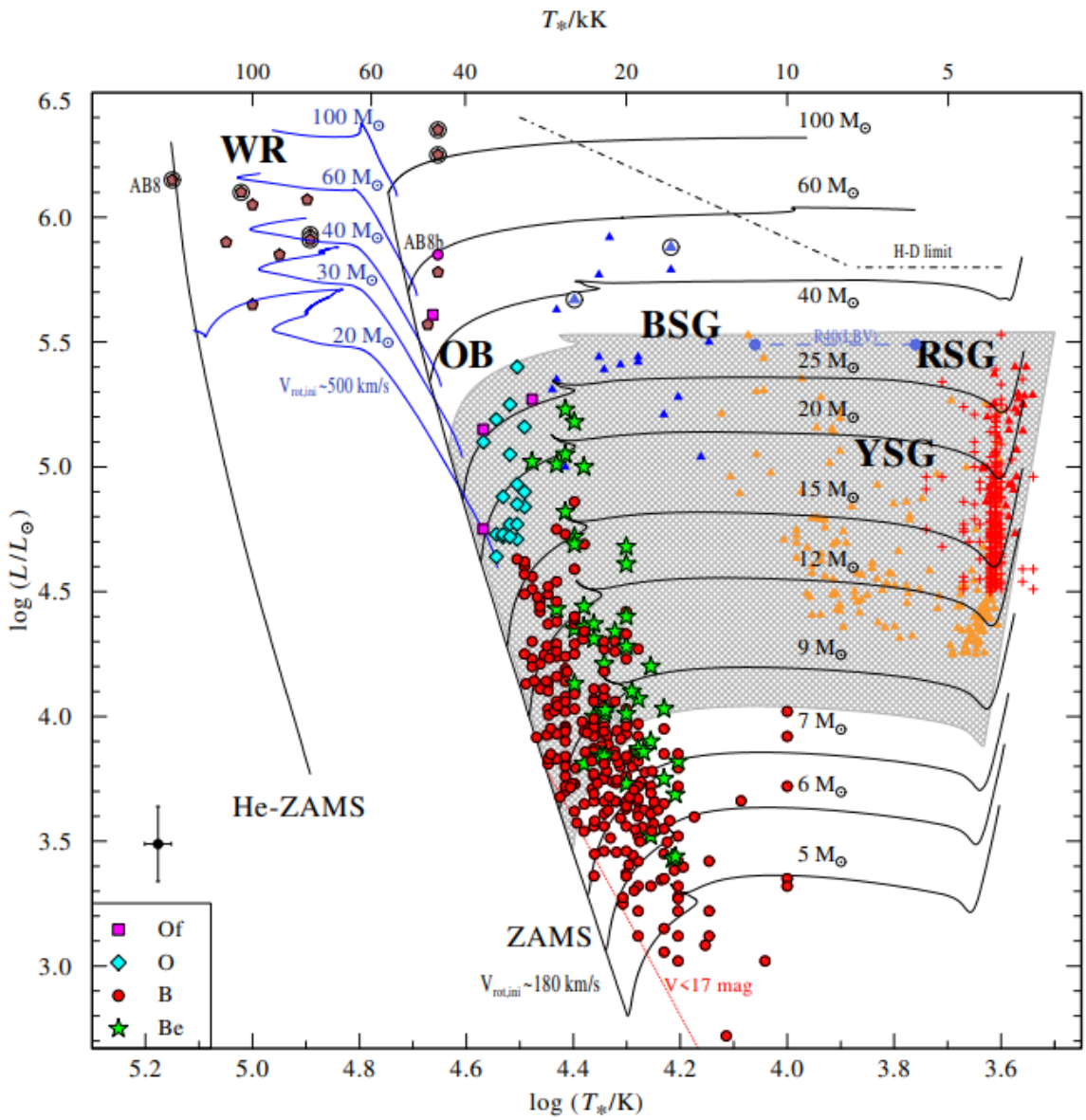

Figure 1.2: Hertzsprung-Russell diagram for massive stars in the Small Magellanic Cloud. It shows O and B main sequence stars, as well as stars evolved to the giant branch (and beyond), along with evolutionary tracks, taking into account stellar rotation. ZAMS is an abbreviation for zero age main sequence. Adopted from Ramachandran et al. (2019).

quite distinct (Massey & Olsen 2003; Levesque 2010). This may occur due to evolutionary proximity to the Hayashi track, which corresponds to a limit when a star can remain in hydrostatic equilibrium (Hayashi & Hoshi 1961).

To correctly place a star into the HR diagram, it is necessary to precisely determine effective temperature and bolometric luminosity. However, this has been an issue for quite some time, e.g., because the colors of these stars are strongly affected by gravity-dependent line blanketing (Massey 1998). Metallicity also significantly affects evolutionary tracks and the position of RSGs in the HR diagram (Elias et al. 1985). Some of the first results were not in agreement with each other, e.g., evolutionary tracks from Meynet et al. (1994) did

not match with observations from Humphreys & McElroy (1984) and later evolutionary tracks from Meynet & Maeder (2003) were also not able to produce as cool and luminous RSGs as observed.

Fortunately, MARCS stellar atmopshere models (Plez et al. 1992; Gustafsson et al. 2008) helped to resolve the issues, as it allowed Levesque et al. (2005) to improve upon the computation of reddened model fluxes and molecular transitions. They were able to use the models to determine effective temperature scale for RSGs, along with measurements of extinction and surface gravity, and in the end they were also able to determine bolometric luminosity. They also used an alternative method to determine bolometric luminosity, based on K magnitude, which is less sensitive to reddening and variability, as was shown by Josselin et al. (2000). Levesque et al. (2005) received results from both models in good agreement with each other, and were thus able to derive a new effective temperature scale, which brought the Galactic RSGs into a great agreement with the evolutionary models, as shown in Figure 1.3.

Based on their new scale, the RSGs are not as cool as previously thought, whilst for the most evolved M supergiants the differences amounted to 400 K. Massey et al. (2005) concludes that determinations of physical properties of RSGs depend on accurate corrections for reddening by dust and that many previous studies have indeed underestimated the correction for extinction in the optical region.

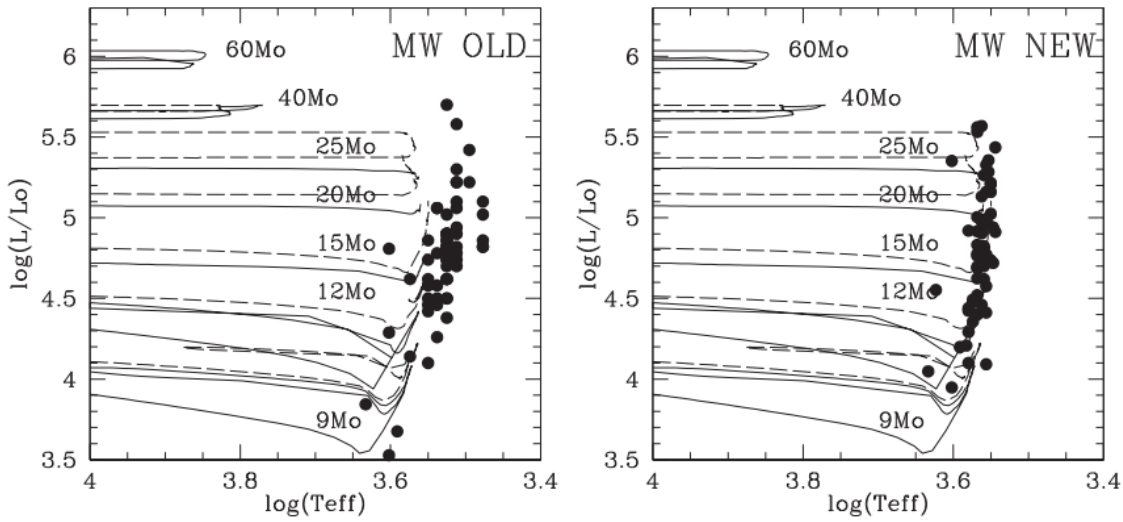

Figure 1.3: Improvements to determination of positions of Galactic RSGs in Hertzsprung-Russell diagram and better agreement with evolutionary tracks. *Left panel:* RSG positions by Humphreys (1978); Humphreys & McElroy (1984). *Right panel:* RSG positions by Levesque et al. (2005). Evolutionary tracks in both panels by Meynet & Maeder (2003). Adapted from Levesque (2010).

1.2 Mass Loss and Dust Production

One of the most significant features of RSGs are their high mass-loss rates, which lead to dust condensation, once the material reaches far enough from the star, i.e., the condensation

radius, and this may subsequently lead to the formation of circumstellar shells (Stothers & Chin 1996).

1.2.1 Observations

Detections of first signs of dust shells were accomplished for RSG stars NML Cyg and VY CMa by Johnson (1968) and Hyland et al. (1969), respectively. For NML Cyg, an extensive circumstellar cloud was proposed through infrared spectroscopy, based on high infrared excess and high luminosity. For the latter star, VY CMa, a circumstellar dust shell was proposed as well, based on spectroscopic and photometric data. Compared to other RSGs, the star was much more luminous and exhibited larger infrared excess, while it was also found that the extinction curve is different from the regular interstellar dust, suggesting larger sizes of dust grains. This was later supported by Snow et al. (1987) as well as through observations of supergiant binary system α Sco. They estimated the circumstellar grain sizes to be $> 0.05\,\mu$m and siliceous in composition. Stencel et al. (1988) and Stencel et al. (1989) analysed a large sample of galactic RGSs and concluded that the circumstellar dust shells around these objects are rather a rule than an exception, not restricted to just the most extreme objects. They also found these shells to be quite extended, up to several arcminutes, while at these distances the sizes of dust grains were $\approx 60\,\mu$m.

Meanwhile, Hagen (1978) and Hagen et al. (1983) analysed chromospheres and circumstellar shells around M giants and supergiants. From the spectroscopic analysis of line profiles of circumstellar gas and interferometric observations of the circumstellar dust they inferred many physical conditions of the dust, such as expansion velocities of the shells as $7-10\,\mathrm{km\,s^{-1}}$, and they also found that all studied stars have emission wings for Ca II H and K lines, whereas only objects with low dust-to-gas ratio had chromospheric emission in the cores of these lines. Most importantly, they suggest that radiative pressure on dust grains is not the principal mechanism of mass loss, as no direct correlation was found between the quantities of circumstellar gas and dust. Quantities of dust were not sufficient to explain the mass-loss rates, which they estimated from $2\cdot10^{-8}\,\mathrm{M_\odot\,yr^{-1}}$ to $6\cdot10^{-6}\,\mathrm{M_\odot\,yr^{-1}}$ for late supergiants. They also argued that shock waves may be linked to mass loss and dust formation.

Danchi et al. (1994) analysed a sample of cool giants and supergiants in mid-infrared interferometry, and due to high enough resolution they were able to determine inner radii of the shells. They found that for the red giants sample (AGB stars, including Mira variables) the inner radii are closer to stars, $\approx 3-5\,\mathrm{R_\odot}$, and for some of these objects it appeared that new dust formed closer to the surface during their luminosity minima. On the other hand, for the sample of RSGs, the inner radii appeared substantially larger with less dust close to the stars, and they also found larger variations in the distance of the inner radii shells from the surface. This indicated that for RSGs the substantial mass-loss episodes, which lead to dust production, are sporadic, typically being separated by a few decades.

Salasnich et al. (1999) presented new models for luminosity-dependent mass-loss rates of RSGs in Magellanic Clouds. They argued that previous results for mass-loss rates were severely underestimated (e.g., de Jager et al. 1988) and that true values were higher by a factor of 2−5. On the contrary, Josselin et al. (2000) analysed the galactic RSGs and found no correlation between luminosity and mass-loss rates, based on infrared photometry

and millimeter spectroscopy. Nonetheless, Levesque (2010) claims this is due to incorrect individual spectroscopic parallaxes that they adapted from Humphreys (1978). Massey et al. (2005) later revisited these results and was able to acquire luminosity-dependent mass-loss rates, when adopting better values for distances.

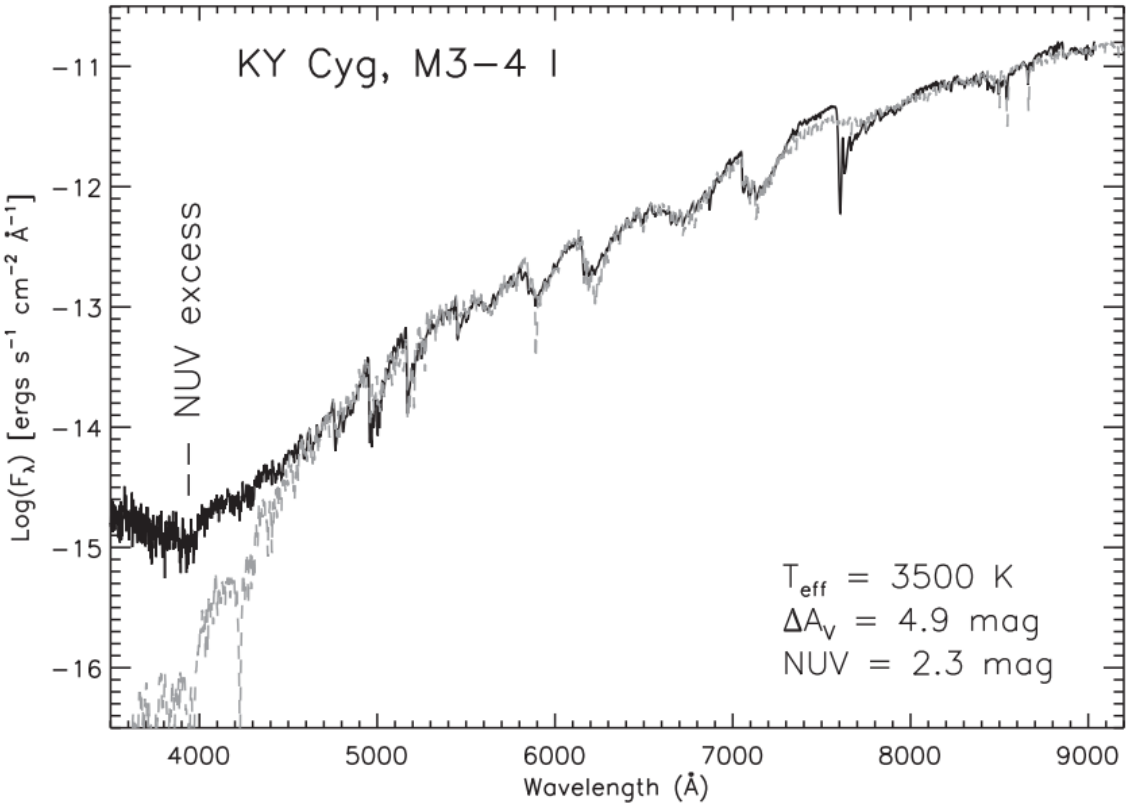

Figure 1.4: An example of NUV excess for a RSG star, based on Massey et al. (2005), compared to best-fit MARCS stellar atmosphere models (gray plot). Adapted from Levesque et al. (2005).

Levesque et al. (2005) also found that many of the Galactic RSGs have excess flux in near ultraviolet (NUV) region, as shown in Figure 1.4. This was explained by Massey et al. (2005), who studied Galactic RSGs in OB associations and clusters and ascertained that RSGs have much higher excess visual extinction when compared to OB stars. They argued that is due to circumstellar shells around the RSGs. Likewise, the stars with the highest extra visual extinction also had significant NUV excess, which is higher compared to the stellar models reddened by the standard reddening law (e.g., Cardelli et al. (1989)).

Levesque et al. (2006) also studied the RSGs in our Galaxy and both Magellanic Clouds, specifically the shift in average spectral type between these galaxies (Elias et al. 1985). They were able to show metallicity-dependent systematic differences in the physical properties of the stars, bringing the observations into agreement with evolutionary models once again, e.g., the scatter from evolutionary tracks in the Small Magellanic Cloud could be explained by a stronger effect of rotational mixing in low-metallicity stars (Maeder & Meynet 2001).

The circumstellar shells of dust can lead to significant complications when determining

physical properties of dust enshrouded supergiants. Levesque et al. (2009) discussed effects of a dust torus on bolometric luminosity for dust-enshrouded giants. They showed that the contribution from the torus must be taken into account when determining bolometric luminosity from a spectrum, as it may lead to overestimation of the luminosity of a star, and thus also its position HR diagram. In some of the most extreme cases, absorption lines in stellar spectra may be partially diluted or obscured due to photon scattering in the dusty envelopes (Massey et al. 2009). Some of the most famous examples of RSGs, for which the determined physical properties were affected, are also some of the largest and brightest stars, VY CMa in the Milky Way and WOH G64 in the Large Magellanic Cloud (Levesque 2010).

Extensive observation campaigns of Betelgeuse revealed that circumstellar envelopes around RSGs can have complex and irregular structures (Figure 1.5), while some of the inner structures may be possible to link to hot convective structures on the surface, or to the rotation of a star (Kervella et al. 2009), and are dominated by non-radial large-scale motions, whose overall behaviour changes dramatically within one year (Ohnaka et al. 2011). The outer atmosphere extends to about 1.4 stellar radii (Ohnaka et al. 2011), while envelopes can extend up to at least several tens of stellar radii (Kervella et al. 2011). The clumpiness and inhomogeneous distribution found in these observations support the theories about previous episodes of extended mass-loss rate events. Moreover, based on observations of VY CMa, Humphreys et al. (2021) revealed evidence of previous high mass-loss rate events for this star, spanning from 70 to 250 years ago. Kervella et al. (2018) suggested that strong convection cells emitting a focused molecular plumes may be contributing to the anisotropy of mass loss of RSGs. Based on the observations of Antares, Cannon et al. (2021) detected a dust clump very close to the surface, at a distance of only about 0.3 stellar radii, and find a minimum mass-loss rate from clumps of $1.5 \cdot 10^{-7}\,\mathrm{M}_{\odot}\,\mathrm{yr}^{-1}$.

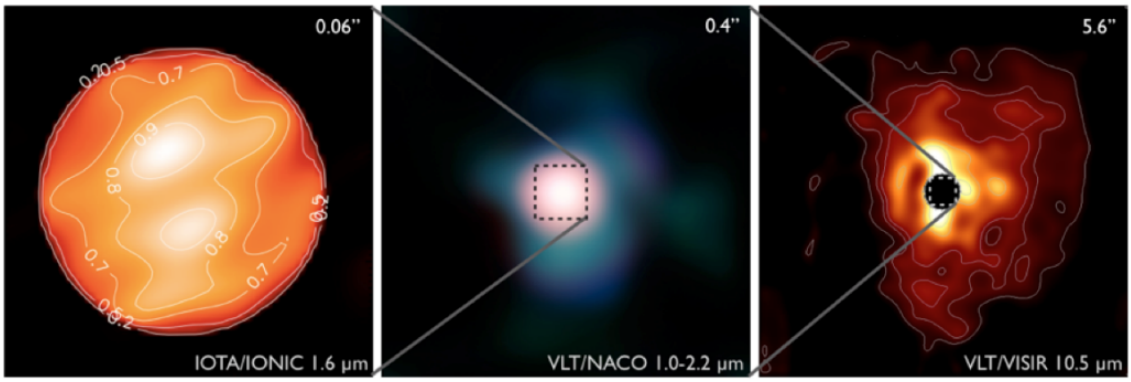

Figure 1.5: *Left panel:* Interferometric image of the photosphere of Betelgeuse obtained by Haubois et al. (2009). *Middle panel:* Emission from a compact molecular envelope obtained by Kervella et al. (2009). *Right panel:* Thermal emission of dust obtained by Kervella et al. (2011). Adapted from Nazé et al. (2015).

Based on observations of VY CMa, Scicluna et al. (2015) estimated the average size of grains at around 0.5 μm, which is about 50 times larger than a diffuse ISM, while Gail et al. (2020) was able to further explore the dust condensation sequence.

Recently, there were interferometric observations of several RSGs in the solar neigh-

bourhood dedicated to the analysis of surface structures and extended molecular envelopes, e.g., observations of several RSGs, including VY CMa and V602 Carinae, by Wittkowski et al. (2012, 2017), observations of AH Sco, UY Sct, and KW Sgr by Arroyo-Torres et al. (2013), and observations of V602 Car by Climent et al. (2020). These observations demonstrated that extended molecular atmospheres are a common feature of RSGs, even though the models failed to predict them, unlike for Mira-type stars. The envelopes consist mostly of H_2O (water) and CO (carbon monoxide, Wittkowski et al. 2021). Wittkowski et al. (2017) found that the strength of extended molecular layers increases with luminosity.

Chiavassa et al. (2022) were able to uniquely observe the photospheric extent and circumstellar environment VX Sgr across a very large spectral domain for the first time. They revealed a complex morphology of the extended atmosphere and found that the observed diameter depends on opacity through the atmosphere. They detected CO and OH (hydroxide) at the shortest wavelengths along with SiO (silicon monoxide) and CO dominating at longer wavelength, while H_2O is present in all wavelengths. A part of the observation is shown in Figure 1.6.

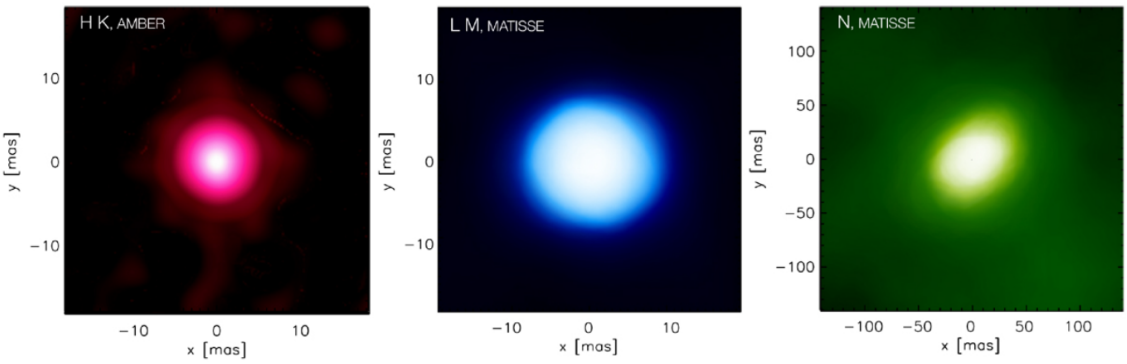

Figure 1.6: Interferometric images of extended atmosphere of VX Sgr at different bands. The images show the complex structure of molecular envelope. Adapted from Chiavassa et al. (2022).

1.2.2 Empirical $\dot{M} - L$ Relations

To determine mass-loss rates, several (primarily luminosity dependent) empirical relations have been used, such as by Reimers (1975), de Jager et al. (1988) and for example by van Loon et al. (2005). In a thorough review, Mauron & Josselin (2011) compared the available $\dot{M} - L$ relations and concluded that the de Jager prescription provides the best results for Galactic RSGs. The relation is given as

$$\log\left[\frac{\dot{M}}{1\,\mathrm{M}_\odot\,\mathrm{yr}^{-1}}\right] = -7.93 + 1.64\log\left[\frac{L}{1\,\mathrm{L}_\odot}\right] + 0.16\log\left[\frac{M}{1\,\mathrm{M}_\odot}\right] - 1.61\log\left[\frac{T_{\mathrm{eff}}}{1\,\mathrm{K}}\right] \quad (1.1)$$

in its second formulation by Nieuwenhuijzen & de Jager (1990).

Nonetheless, Mauron & Josselin (2011) also found some RSGs with mass-loss rates lower than the ones given by de Jager curve. A decade later, Humphreys et al. (2020) showed that for RSGs with luminosities $< 10^5\,\mathrm{L}_\odot$, the measured mass-loss rates are lower, while

for $> 10^5\,L_\odot$, there is a rapid transition to higher mass-loss rates, eventually overlaping the de Jager curve. This luminosity threshold appears approximately for RSGs with masses of $18-20\,M_\odot$, which interestingly also is the upper limit for becoming a Type II supernova.

1.2.3 Current Day Theories

Humphreys & Jones (2022) analysed new observations of VY CMa and Betelgeuse and discussed the leading mechanisms for mass loss in RSGs, namely the dust-driven wind, pulsations and convection. However, as they discussed, these mechanisms do not precisely reproduce observed mass-loss rates.

Radiative pressure on grains of dust does not help to resolve the scatter from observed mass-loss rates, unlike in AGB stars (van Loon et al. 2006; Höfner 2008), where simulations shows that pulsations are able to levitate the atmosphere and deposit material closer to the condensation radius. Freytag & Höfner (2023) were able to demonstrate that shock waves lead to mass loss and subsequent dust formation in these stars.

Nevertheless, the levitation by pulsations seems less efficient in the low-density atmosphere of RSGs. It however still seems to be within the realm of possibility that pulsations in combination with the activity of giant convective cells may be responsible for enhanced outflows of material. The typical timescale between the ejection of clumps of material is ≈ 5 years and coincides with the usual longer period of variability of RSGs, which is usually associated to pulsation and convective behaviours, or their interplay (Ohnaka 2014; Humphreys et al. 2021; Cannon et al. 2021). Furthermore, the recent mass loss event of Betelgeuse, the Great Dimming, was in synchronicity with the maximum of photospheric velocity during the ≈ 400 day cycle (Dupree et al. 2020; Granzer et al. 2021; Montargès et al. 2021). Humphreys & Jones (2022) proposed that the missing component of mass loss are episodes of high-mass-loss gaseous outflows, likely caused by large-scale surface activity and magnetic fields, that may contribute significantly to the observed mass-loss rates, and they show that that it can help explain the observed mass-loss rates for studied stars.

The formation of shock waves may provide another key component to understanding the mass loss of RSGs, as the unprecedented ejection of material during the Great Dimming of Betelgeuse was preceded by a strong shock in the atmosphere (this work, Kravchenko et al. 2021; Dupree et al. 2022). Furthermore, through spectropolarimetry imaging, López Ariste et al. (2022, 2023) reported rising plasma in convective cells, in some cases being driven by an unknown force acting on the plasma and counteracting the gravity force. The force is sufficient to maintain plasma rising to heights, where this velocity is comparable to the escape velocity. Thus, this new mechanism could significantly contribute to explanation of the mass loss from RSGs.

We will discuss the physics behind these major mechanisms in Chapter 2.

1.3 Variability

Red supergiants are some of the most luminous stars, therefore their variability have been observed for many decades and in some cases even for a few hundred years. For some of

the brightest RSGs, there exist written records from thousands of years ago (Neuhäuser et al. 2022).

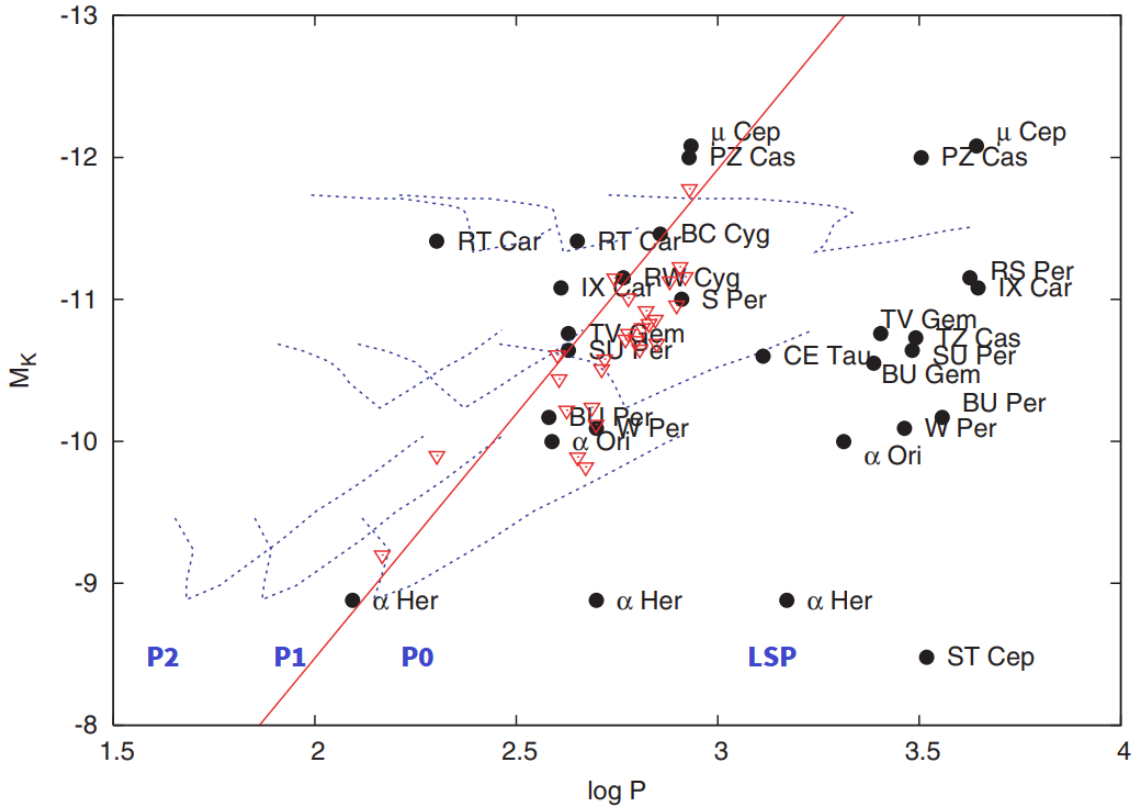

Figure 1.7: Period-absolute magnitude relation for Galactic (black dots) and Large Magellanic Cloud (red triangles) RSGs. The dotted lines are based on models from Guo & Li (2002) and represent (from right to left) fundamental, first overtone and second overtone modes for stars (from bottom to top) of $\approx 15\,M_\odot$, $\approx 20\,M_\odot$ and $\approx 30\,M_\odot$. The group of periods on the right side of the figure is called long secondary period (LSP). Red line is a linear fit of the Galactic sample. Guo & Li (2002) were not able to model the LSP mode. Adapted from Kiss et al. (2006).

Many RSGs show photometric and spectroscopic variability, which is usually characterized by two distinct semi-regular timescales: one of a few hundred days, and one of a few thousands days (Kiss et al. 2006; Chatys et al. 2019). Figure 1.7 shows the $P-L$ distribution for several RSGs in our Galaxy and Large Magellanic Cloud. Kiss et al. (2006) also noted that there are several RSGs with very large peak-to-peak light variations and a high level of noise in their period power spectrum, which could correspond to more dynamical environment in more evolved RSGs closer to central helium exhaustion. In some of these RSGs, the noise in the power spectrum becomes stronger and no periodicity can be detected at all. In the power spectra of all RSGs, the main component of the noise can be characterized by inverse power function of frequency. Kiss et al. (2006) argued that this noise is likely caused by huge convection cells, as predicted by Schwarzschild (1975), and is likely responsible for the observed fluctuations of variability. Chatys et al. (2019) noted that a complete analysis of variability is mainly challenged by the requirement of long term

photometric monitoring, as well as by incomplete theoretical basis.

1.3.1 Fundamental Mode

The periods of a few hundred days are identified with radial fundamental mode (FM) of pulsations, and possibly low-order overtones as well. In some cases, the RSGs seem to pulsate in the fundamental and first overtone mode simultaneously (Kiss et al. 2006). This type of pulsational instability is also predicted by models, e.g., by Guo & Li (2002). These shorter modes of pulsations may be stochastically driven by convective motions in the envelope (Schwarzschild 1975; Bedding 2003; Kiss et al. 2006; Chatys et al. 2019), or rather by an interplay of convection and pulsation. Assuming that the stochastic excitation or damping indeed occurs in the RSGs and considering the usual availability od the data, we would often measure an instantaneous period, comparable in length to the mode lifetime, rather than the mean period of star, which has the real physical meaning (Kiss et al. 2006).

Dolan et al. (2016) were unable to reproduce the oscillations in fundamental and first overtone modes with adiabatic models alone. Therefore, they suggested that non-adiabatic pulsations and convection could be responsible. Based on their models, large-scale granular convection could drive the pulsations. Joyce et al. (2020) demonstrated on Betelgeuse that the ≈ 400 day period is due to the pulsations in the fundamental p-mode (pressure driven) and suggest that the fundamental mode of radial pulsations is driven by the κ-mechanism. The oscillation is thus driven by radial pulsations in the hydrogen ionization zone, i.e., the collective expansion and contraction of the recombined hydrogen layer. They also further discussed the excitation of the oscillation mode to the first overtone. Possibly, it could be caused by non-linear mode excitation, when outer layers accumulate sufficient energy, which could lead to compression heating and affect convection flux in near surface regions.

1.3.2 Long Secondary Period

The origin of a few thousand days period is considerably less clear. It cannot be explained by radial pulsations, because the FM is the longest possible period for that kind of oscillations. The longer period of a few thousand days is called long secondary periods (LSP), based on presumed similarity of this type of variability to the one in AGB stars (Kiss et al. 2006; Chatys et al. 2019).

For this phenomenon in AGB stars, Wood (2000) proposed wide range of possible driving mechanisms: non-radial oscillations of gravity modes, semi-detached binaries, rotating stars with giant star spots, episodic dust ejection, magnetic activity or strange pulsation modes caused by convection-pulsation interaction. Wood et al. (2004) noted that all these models have problems and that the most likely explanation are large-amplitude, low-degree gravity modes oscillations confined to outer thick (thicker than models suggest) radiative layer above the convection zone, combined with large-scale surface activity. They also conclusively ruled out the radial pulsations. We can also rule out the rotational modulation, because the rotational period for Betelgeuse given by Kervella et al. (2018) is much longer than the length of LSP. Joyce et al. (2020) also confirmed that LSP is not driven by the same mechanism as the FM or its low-order overtones.

Stothers (2010) showed that LSP could be connected to the evolution of giant convection

cells, specifically their turnover timescales. Stothers (2010) further suggested that the convection cells likely overshoot above into a weakly radiative atmosphere (Josselin & Plez 2007; Gray 2008), causing observed chromospheric activity and dust production (Uitenbroek et al. 1998; Lobel & Dupree 2000). Thus, matter would be essentially pushed outward by the convection cells, but most of it would eventually fall back, as the cell would turn over (Stothers 2010). The new results from spectropolarimetry imaging of giant convective cells on the surface of Betelgeuse by López Ariste et al. (2018, 2022) could be used to support this.

Chapter 2

Model Atmospheres of Red Supergiants

2.1 Fundamental Physical Concepts

This Section 2.1 is adapted from Hubeny & Mihalas (2014).

Stars are in mechanical equilibrium for the majority of their lives. The equilibrium governs all properties of a star and any departure from it would quickly lead to a reaction that restores the equilibrium.

2.1.1 Hydrodynamical Equations

The most general quantity that describes a physical system is a distribution function, such as the Boltzmann (kinetic) distribution function, which fully describes the system. However, in such a function, there is more information than we need for practical use. Therefore, in order to describe a system, equations of moments of the distribution function are used. The results of these equations are commonly used and known as hydrodynamical equations.

The zeroth-order moment of the Boltzmann equation describes the conservation of mass and is thus known as equation of continuity, given as

$$\frac{\partial \rho}{\partial t} + \nabla \cdot (\rho \boldsymbol{v}) = 0. \tag{2.1}$$

The first moment of the Boltzmann equation describes the motion, and it is thus known as the momentum equation, given as

$$\rho \frac{\partial \boldsymbol{v}}{\partial t} + \rho \boldsymbol{v} \cdot \nabla \boldsymbol{v} = -\nabla p + \rho \boldsymbol{g}. \tag{2.2}$$

The third equation is the energy balance equation, given as

$$\frac{\partial}{\partial t}\left(\rho \varepsilon + \frac{\rho v^2}{2}\right) + \nabla \cdot \left[\rho \boldsymbol{v}\left(\varepsilon + \frac{v^2}{2}\right) + p\boldsymbol{v}\right] = \rho \boldsymbol{v} \boldsymbol{g} - \nabla \cdot (\boldsymbol{F}_{\text{rad}} + \boldsymbol{F}_{\text{cond}}). \tag{2.3}$$

In these equations, $\nabla = \left(\frac{\partial}{\partial x}, \frac{\partial}{\partial y}, \frac{\partial}{\partial z}\right)$, $\boldsymbol{v}$ is the macroscopic velocity (bold letter means vector), ρ is the density, p is the pressure, $\boldsymbol{g}$ is the gravity acceleration, ε is the internal energy, $\boldsymbol{F}_{\text{rad}}$ is the radiative flux, and $\boldsymbol{F}_{\text{cond}}$ is the conduction flux. In the equations except

the gravity, there could be other external forces $\boldsymbol{f}_{\text{ext}}$ on the right hand side, namely the radiative force $\boldsymbol{f}_{\text{rad}}$.

This system of partial differential equations is still quite general and difficult to solve analytically. Thus, for practical use, several additional approximations may be used, namely stationary ($\frac{\partial}{\partial t} = 0$) and static ($\boldsymbol{v} = 0$) scenarios, as well as simplified symmetries, namely planar ($\boldsymbol{v} = (0, 0, v_z)$) and spherical ($\boldsymbol{v} = (v_r, 0, 0)$).

Solutions for the Static Scenario

The most approximated case, the static scenario in 1D, results into some of the most fundamental equations.

From the momentum equation (Equation 2.2), we receive the hydrostatic equilibrium, given as

$$\frac{\mathrm{d}p}{\mathrm{d}z} = -\rho g, \tag{2.4}$$

which tell us that if there are no fast radial motions, the gradient of internal pressure is in balance with the gravity everywhere in the star.

From the energy equation (Equation 2.3), we receive the radiative equilibrium equation, given as

$$F_{\text{rad}} = \text{const} \equiv \sigma T_{\text{eff}}^4 = \frac{L}{(4\pi R)^2}, \tag{2.5}$$

where σ is Stefan-Boltzmann constant. The equation tell us that the energy in the atmosphere is transported only by radiation (if we neglect the conductive flux). This is elaborated further in Equation 2.14.

2.1.2 Stellar Atmospheres

Local Thermodynamic Equilibrium

For the description of stellar atmospheres we often use local thermodynamic equilibrium (LTE), even though it is not valid for a star as a whole. This approximation allows us to use thermodynamic equilibrium locally, which means we can assume that each excitation and ionization process is in balance with its inverse counterpart, while we can also assume Maxwellian velocity distribution of particles. It thus simplifies the problem substantially, as we can calculate the distributions that depend solely on thermodynamic variables, typically by temperature T and also by total particle number density N or electron number density n_{e}.

The Boltzmann excitation equation is given as

$$\frac{n_j}{n_i} = \frac{g_j}{g_i} \exp\left\{-\frac{E_j - E_i}{kT}\right\}, \tag{2.6}$$

where n is the population of an excited state (for energy levels i and j), g is statistical weight, E is energy of a level and k the Boltzmann constant. The equation allows us to compute populations of excited energy levels.

Saha ionization equation is given as

$$\frac{N_I}{N_{I+1}} = n_{\mathrm{e}} \frac{U_I}{U_{I+1}} C T^{-3/2} \exp\left\{ -\frac{E_I}{kT} \right\}, \tag{2.7}$$

where N is the total number density of a ionization stage, U is the partition function, E_I is the ionization potential of ion and C is a constant. The equation describes the total number densities of two ionization stages.

Radiative Transfer

Equations in Section 2.1.1 described the material properties. The following equations of radiative transfer may be viewed as kinetic equation for photons.

To get a complete description of the radiative field, the specific intensity I is used. It is defined as elementary energy

$$\mathrm{d}E = I(\boldsymbol{r}, \boldsymbol{n}, \nu, t)\, \mathrm{d}S \cos\theta \mathrm{d}\varpi \mathrm{d}\nu \mathrm{d}t, \tag{2.8}$$

transported by radiation across an elementary area dS and into angle dϖ. θ is the angle between $\boldsymbol{n}$ and a normal to dS. We also define moments of I, namely the mean intensity J (zeroth moment), H (first moment) and K (second moment). The energy flux of radiation is given as $\boldsymbol{F} = \oint \boldsymbol{n} I \mathrm{d}\varpi$.

In the thermodynamic equilibrium, the specific intensity is equal to Planck function, $I = B$, which is given as

$$B(\nu, T) = \frac{2h\nu^3}{c^2} \frac{1}{e^{\frac{h\nu}{kT}} - 1}, \tag{2.9}$$

where h is the Planck constant and c is the speed of light.

Finally, the change of specific intensity is described by the radiative transfer equation, given as

$$\left(\frac{1}{c} \frac{\partial}{\partial t} + \boldsymbol{n} \cdot \nabla \right) I(\boldsymbol{r}, \boldsymbol{n}, \nu, t) = \eta(\boldsymbol{r}, \boldsymbol{n}, \nu, t) - \chi(\boldsymbol{r}, \boldsymbol{n}, \nu, t) I(\boldsymbol{r}, \boldsymbol{n}, \nu, t), \tag{2.10}$$

where χ is the absorption (or opacity) coefficient and η is the emission coefficient. The coefficients describe the interaction of radiation and matter. The equation expresses the variations of specific intensity due to passing through a volume of material. The (true) total absorption coefficient is defined as $\chi = \varkappa + \sigma$, where $\varkappa$ is the contribution by thermal absorption and σ is the contribution by scattering due to collisions. Mass absorption coefficient defined as $\kappa = \chi/\rho$ is often used as well.

For the spherically symmetric static case $\boldsymbol{n} \cdot \nabla = \mu \frac{\partial}{\partial r} + \frac{1-\mu^2}{r} \frac{\partial}{\partial \mu}$, and thus the radiative transfer equation is given as

$$\mu \frac{\partial I(\nu, \mu, r)}{\partial r} + \frac{1-\mu^2}{r} \frac{\partial I(\nu, \mu, r)}{\partial \mu} = \eta(\nu, \mu, r) - \chi(\nu, \mu, r) I(\nu, \mu, r), \tag{2.11}$$

where $\mu = \cos\theta$.

For static planparalel atmosphere and $n_z = \cos\theta \equiv \mu$, we can write

$$\mu \frac{\mathrm{d}I_{\nu\mu}}{\mathrm{d}\tau_\nu} = I_{\nu\mu} - S_{\nu\mu}, \tag{2.12}$$

where $\mathrm{d}\tau_\nu \equiv -\chi_\nu \mathrm{d}z$ is the elementary optical depth and $S_\nu \equiv \frac{\eta_\nu}{\chi_\nu}$ the source function. As it is customary, the dependences are shown as a subscript.

An important elementary solution for Equation 2.12 is a semi-infinite atmosphere with a linear source function, given as

$$I_\nu(\tau = 0, \mu) = S_\nu(\tau = \mu) = a + b\mu, \tag{2.13}$$

where a source function is a linear function of optical depth. The equation is called Eddington-Barbier relation and in general, it provides a good estimate for the emergent flux.

Radiative Equilibrium

The equilibrium of radiation is given as

$$\nabla \cdot \boldsymbol{F}_{\mathrm{rad}} = \int_0^\infty \mathrm{d}\nu \oint (\eta_\nu - \chi_\nu I_\nu)\, \mathrm{d}\varpi = 0, \tag{2.14}$$

which expresses that the radiative flux is conserved.

Once we integrate over all angles, we can use the mean intensity J and thus write

$$\int_0^\infty \varkappa_\nu (J_\nu - S_\nu)\, \mathrm{d}\nu = 0, \tag{2.15}$$

where instead of the total absorption coefficient χ_ν, we can write the thermal absorption coefficient $\varkappa_\nu$, as we can assume that the scattering contributions σ_ν cancel out.

Statistical Equilibrium

To calculate the number densities of atoms and ions in individual levels in non-LTE, the statistical equilibrium equation is used, given as

$$n_i \sum_{j \neq i} \left(R_{ij} + C_{ij}\right) - \sum_{j \neq i} n_j \left(R_{ji} + C_{ji}\right) = 0, \tag{2.16}$$

where the first term of the equation represents the total number of transitions out of level i, while the second term represents the transitions into level i. R is defined as the radiative rate and C as the collisional rate, each for a transition between two levels.

These equations of statistical equilibrium would form a linearly dependent system, therefore it is necessary to add another equation, such as the abundance equation.

2.2 Radiatively Driven Stellar Winds

This Section 2.2 is adapted from Lamers & Cassinelli (1999), unless when stated otherwise.

Nearly all stars lose mass through stellar wind during their lives, affecting their evolution. To describe the properties of stellar wind, the hydrodynamical equations from Section 2.1.1 are used in a spherically symmetric stationary approximation.

By integrating the equation of continuity, we receive the equation of mass conservation, given as

$$\dot{M} = 4\pi r^2 \rho \boldsymbol{v}, \tag{2.17}$$

which expresses a mass flux from a star through a sphere of radius r.

The combination of equations of continuity (Equation 2.1) and momentum (Equation 2.2) results into momentum equation for stellar wind, given as

$$\left(1 - \frac{a^2}{v^2}\right) v \frac{\mathrm{d}v}{\mathrm{d}r} = \frac{2a^2}{r} - \frac{\mathrm{d}a^2}{\mathrm{d}r} - \frac{GM}{r^2} + f, \tag{2.18}$$

where a is the isothermal speed of sound, defined as $a = \sqrt{\frac{p_{\mathrm{gas}}}{\rho}}$, G is the gravitational constant, and f is an additional force, which could be for example f_{rad}.

To describe the energy of the wind, the Equation 2.3 is rewritten without the flux, while energy per unit mass $e(r)$ is used. It is given as

$$e(r) = \frac{v^2}{2} + \frac{GM}{r} + \frac{\gamma}{\gamma - 1} \frac{p_{\mathrm{gas}}}{\rho}, \tag{2.19}$$

which essentially is a sum of kinetic energy, gravitational energy and enthalpy, where γ is the heat capacity ratio (adiabatic exponent).

2.2.1 Isothermal Winds

For an idealized isothermal stellar wind, with no other forces acting on the gas than the gravity and gradient of the gas pressure, the momentum equation is given as

$$\left(1 - \frac{a^2}{v^2}\right) v \frac{\mathrm{d}v}{\mathrm{d}r} = \frac{2a^2}{r} - \frac{GM}{r^2}. \tag{2.20}$$

This simplified scenario has several solutions depending on the initial conditions, as shown in Figure 2.1, but there is only one critical solution, for which the velocity starts as subsonic near the stellar surface, and reaches supersonic values far from the star (the transonic solution).

For $v(r) = a$, which is the sonic point, the momentum equation has a singularity. This important distance is called a critical point, given as

$$r_{\mathrm{c}} = \frac{GM}{2a^2}. \tag{2.21}$$

The location of the critical point depends only on the conditions below the critical point, not beyond it, as the information cannot be transmitted back. The velocity in the critical point is given as

$$v(r_{\mathrm{c}}) = a = \frac{v_{\mathrm{esc}}(r_{\mathrm{c}})}{2}, \tag{2.22}$$

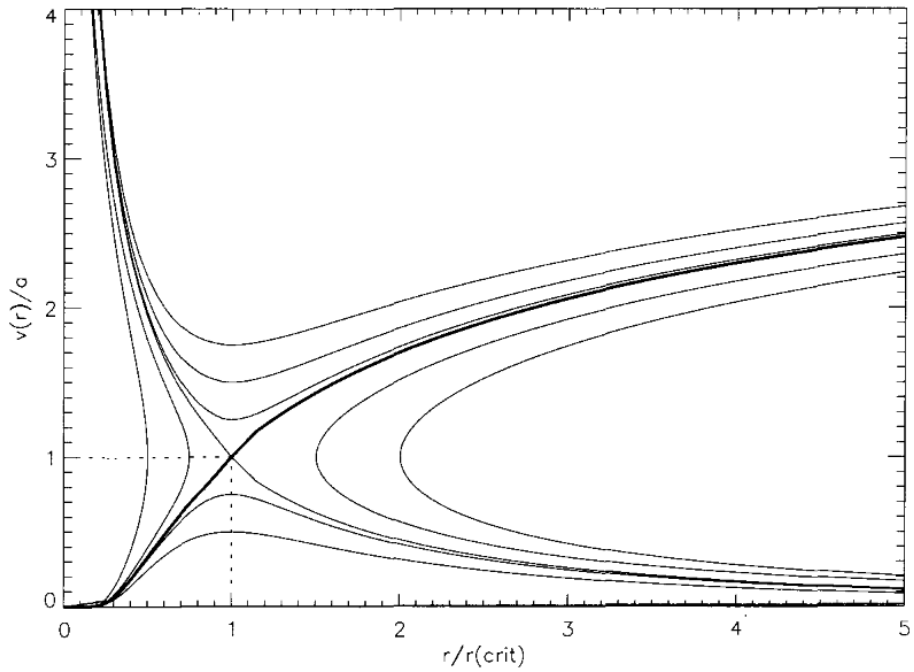

Figure 2.1: Solutions of the momentum equation for isothermal wind (Equation 2.20). The thick curve is the transonic solution. Adapted from Lamers & Cassinelli (1999).

where the escape velocity is given as $v_{\rm esc} = \sqrt{2GM/r_{\rm c}}$.

The existence of only one correct solution implies that the critical solution occurs only for one specific value of initial velocity v_0 at the lower boundary r_0 of the isothermal region (assuming fixed density). Below the sonic point, the properties of the wind are primarily determined by the hydrostatic equilibrium, while above the sonic point the properties are mainly due to forces that cause the velocity to increase.

The energy equation for isothermal wind is given as

$$e(r) = e(r_0) + \frac{v^2 - v_0^2}{2} + \frac{GM}{r_0}\left(1 - \frac{r_0}{r}\right). \tag{2.23}$$

This shows that the energy is not constant, but it starts as negative and increases to positive values at larges distances. Thus, there must be an additional energy input, which would be transferred into kinetic energy of the wind. It may be possible to use isothermal description for winds, in which the temperature changes are primarily due to radiative processes.

In cases when the forces driving the wind depend on $\frac{{\rm d}v}{{\rm d}r}$, the sonic and critical points are no longer in the same location.

2.2.2 Dust-driven Winds

Due to low effective temperatures of cool luminous giant and supergiant stars, the material in outer atmospheres may condensate into dust grains. The grains have much larger opacity than gas, therefore the grains are able to absorb photons over a large range of wavelengths, partially blocking the radiation from the star. Thus, this leads to radiative pressure on dust grains, which is referred to as dust-driven stellar wind, but sometimes also as continuum

driven wind or wind driven by continuous opacity. The absorbed stellar photons transfer its energy and momentum to the dust grains, causing approximately outward net acceleration of the grains. The accelerated grains collide with surrounding gas (and other grains), producing a drag force f_{drag} on the gas. Thus, in result, the dust and gas particles are coupled and move outward from the star, leading to very large mass-loss rates.

For the radiation field to be able to drive the mass loss, it must exceed the gravity. The ratio of accelerations due to these two forces is described by the Eddington parameter. In a general form, the ratio is given as

$$\Gamma = \frac{g_{\mathrm{rad}}}{g_{\mathrm{grav}}} = \frac{\kappa L}{4\pi r^2 c} \cdot \frac{r^2}{GM} = \frac{\kappa L}{4\pi c GM}. \tag{2.24}$$

For the radiative forces on the dust, we write Γ_{d} and instead of opacity κ we use the radiative pressure mean opacity κ_{rp}.

In subsonic region, the gravity is stronger than the radiative force. However, once the dust grains form, Γ_{d} very quickly grows and thus the grains are quickly accelerated to the sound speed. Therefore, we can assume that the condensation radius r_{c} and the sonic radius r_{s} are approximately the same ($r_{\mathrm{c}} \cong r_{\mathrm{s}}$).

Momentum of a Continuum Driven Wind

The momentum of stellar photons is $\frac{h\nu}{c}$, therefore the total momentum of the radiation from the star is $\frac{L}{c}$. We estimate the efficiency of the coupling of gas and dust by the ratio of the final momentum to the radiative momentum, given as

$$\eta_{\mathrm{mom}} = \frac{\dot{M} v_\infty}{L/c}, \tag{2.25}$$

where v_∞ is the terminal velocity of the wind. Assuming a single scattering limit ($\eta_{\mathrm{mom}} \approx 1$), i.e. each photon interacted just once, we can estimate maximum mass-loss rates.

For a dust-driven wind, the momentum equation is given as

$$v\frac{\mathrm{d}v}{\mathrm{d}r} + \frac{1}{\rho}\frac{\mathrm{d}p}{\mathrm{d}r} + \frac{GM}{r^2} = g_{\mathrm{rad}} = \frac{GM}{r^2}\Gamma_{\mathrm{d}}. \tag{2.26}$$

We integrate the momentum equation over elementary mass dm of the outflowing gas, starting at the photospheric radius R and going to infinity, through the sonic and condensation radii. Assuming that velocity at the photosphere is negligible compared to the terminal wind velocity v_∞, that hydrostatic equilibrium holds sufficiently well in the subsonic region, and that beyond the sonic point the gradient of pressure is negligible compared to the gradient of radiative pressure, we arrive at

$$\dot{M} v_\infty = \frac{L}{c}\frac{\Gamma_{\mathrm{d}} - 1}{\Gamma_{\mathrm{d}}}\tau_{\mathrm{W}}, \tag{2.27}$$

where $\tau_{\mathrm{W}} = \int_{r_{\mathrm{s}}}^{\infty} \kappa_{\mathrm{rp}} \rho \mathrm{d}r$ is the optical depth of the wind. This equation shows that the maximum mass-loss rates are not constrained by the single scattering limit only, but also by Γ_{d} and τ_{W}, and can thus be even higher. The equation also shows that the final momentum of the wind in supersonic region ($\Gamma_{\mathrm{d}} \gg 1$) is determined by the optical depth of the wind.

Terminal Velocity

There is a separate momentum equation for grains and gas, coupled by the drag force $f_{\rm drag}$. The force depends on drift speed $w = v_{\rm dust} - v_{\rm gas}$. By integrating the momentum equation for gas in supersonic region, we can estimate the terminal velocity as

$$v_\infty = \sqrt{\frac{2GM}{r_{\rm c}}(\Gamma_{\rm d} - 1)}, \tag{2.28}$$

which is a form of β-type velocity law. The terminal velocities for the dust-driven wind are on the order of tens of $\mathrm{km\,s^{-1}}$.

Properties of Dust Grains

The grain heats up due to the absorption of photons and collisions, while it cools down due to thermal emission. Assuming that the radiative processes are dominant, we can determine the temperature of the grain from radiative equilibrium (Equation 2.14), using the absorptive grain opacity $\varkappa_{\rm d}$.

Condensation radius $r_{\rm c}$ is different for each molecule, and is a steep function of stellar $T_{\rm eff}$. For a typical AGB star with $T_{\rm eff}$ in range of 2000 to 3000 K, the condensation radius of silicate grains increases from about 1.15 to 3 stellar radii, respectively.

The average radius of grains in dust shells around RSGs is estimated to be about 0.5 µm (Scicluna et al. 2015). Gilman (1969) proposed there are two main types of grains, based on the ratio of carbon to oxygen. Dust of oxygen-rich stars primarily consist of silicate grains, while dust of carbon-rich stars (evolved AGB stars) primarily consists of amorphous carbon. Speck et al. (2000) suggested that dust in RSGs follows different condensation sequence than in AGB, likely due to lower carbon to oxygen ratios and UV radiation, i.e., they suggest it progresses from Al_2O_3 (alumina) and Ca-Al-rich silicates to magnesium silicates. Verhoelst et al. (2009) also detected additional dust species in dust shells of RSGs, most likely amorphous carbon. The newer multi-wavelength observations (Wittkowski et al. 2021; Chiavassa et al. 2022) showed that CO and OH are the most prominent ones at shorter wavelengths (larger apparent diameter) and SiO and CO dominate at longer wavelength (smaller apparent diameter), while H_2O contributes across the spectral range. Gail et al. (2020) suggested that alumina, metallic iron, or other large transparent grains such as Ca-Al-rich silicates may be formed below 2 stellar radii, which may serve as seeds for formation of Mg-Fe-rich silicate at larger radii.

Limits on the Mass-loss Rates

The efficiency of the dust-driven wind also depends on mass-loss rate of a star. In case when mass-loss rate is not sufficient, the density at near condensation radius is not significant enough for the dust-driven wind to occur. That is due to higher drift of the grains relative to the gas, which leads to lower ratio of the dust to the gas.

The upper limit is the reddening effect, which may occur for cool stars with the extreme mass-loss rates, such as OH/IR sources (extremely bright infrared sources with OH maser emission). The dust shell becomes optically thick and we receive no or very little direct stellar radiation, as it is absorbed at the inner radius of the shell, where also the condensation

radius lies. The radiation is re-radiated at longer wavelengths, while the grain opacities decrease with increasing wavelength. Thus, in result, the outward acceleration by radiation decreases.

Combining this with other limitations mentioned before (temperature and luminosity), the dust-driven mechanism of stellar wind is possible only for a narrow band of very cool giant and supergiant stars in the HR diagram. However, this mechanism produces some of the largest mass-loss rates observed.

The Role of Pulsations

As it was made clear in this section, the mass-loss rate due to the dust-driven wind depends on density, i.e., it requires that some material is already present near the condensation radius. Therefore, there must be an additional mechanism that provides a sufficient density, otherwise no significant dust-driven wind could be generated. Stellar pulsations may extend the atmosphere and thus levitate material near the condensation radius. While for AGB stars, namely Mira-type and OH/IR stars, this mechanism explains sufficiently well the observed mass-loss rates, as the mass-loss rates are correlated with the pulsation periods, in the case of RSGs the situation is more complicated.

The mechanism of pulsations are further explored in Section 2.4.

2.2.3 Other Types of Stellar Wind

Line-driven Winds

Line-driven stellar wind, a dominant type of the wind for hot massive stars (the progenitors of RSGs), may also occur in RSGs, but it makes only a slight contribution (Bennett 2010; Levesque 2017). Doppler shifting of spectral lines is an important factor for line-driven winds. However, the terminal velocities of material in cool evolved stars amounts to a shift $\lambda v_\infty/c$ of only a few Å, unlike for hot stars, where the shifts are much larger. Therefore, radiative pressure on spectral lines is unable to drive the mass loss on its own.

Nonetheless, Josselin & Plez (2007) proposed that radiative pressure on molecular lines could initiate the mass loss in RSGs (in combination with high convective motions). Later, Arroyo-Torres et al. (2015) was able to correlate observations with this theory.

Alfvén Wave-driven Winds

Perturbations in magnetic field lines may be induced at the base of the stellar wind, generating Alfvén waves that propagate outwards. These waves dissipate into the outer atmopshere, transferring its energy and momentum. This mechanism naturally requires a presence of magnetic fields.

Moderate magnetic fields of a few G were indeed detected in RSGs (e.g., Tessore et al. 2017). However, the Alfvén waves require ionized material, while the circumstellar envelopes around very cool stars consist of mostly neutral gas. Therefore, Alfvén waves are not expected to contribute significantly to the mass-loss rates of RSGs, although the exact degree of its contribution remains unclear (Levesque 2017).

Sound Wave-driven Winds

The convective zones in photospheres of stars may generate acoustic waves that propagate outwards, producing wave pressure on material in outer atmosphere. The gradient of this pressure could drive the wind in stars with low surface gravity, such as the supergiants.

This mechanism is confirmed to heat the chromospheres of RSGs, but does not appear to contribute significantly to the stellar wind (Bennett 2010). The heating of chromosphere due to convection is shown in Figure 2.2.

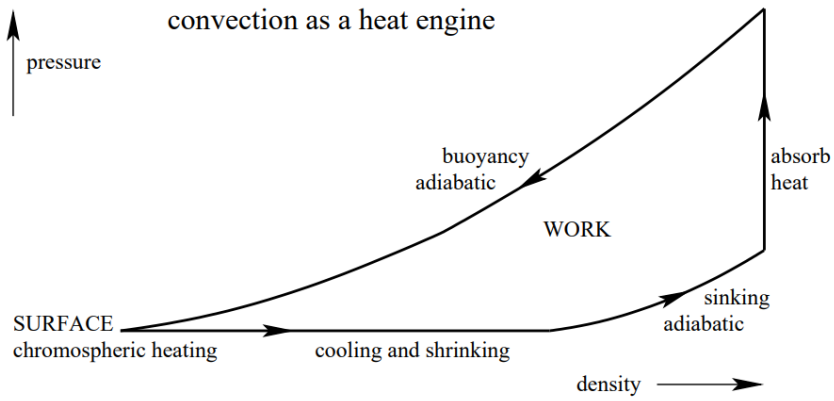

Figure 2.2: Convection acting as a heat engine, powering the chromosphere. Adapted from van Loon (2013).

Supra-Eddington Mass Loss

The Eddington limit (from Equation 2.24 for $\Gamma = 1$) is given as

$$L_{\mathrm{Edd}} = \frac{4\pi c G M}{\kappa}. \tag{2.29}$$

If this limit for luminosity is reached, it means that the atmosphere is no longer bound and thus high-mass loss rates may occur. The limit may be decreased in outer layers and thus causes instabilities, such as due to ionization of hydrogen layer beneath the surface. This limit is also crucial for the upper mass limit of RSGs (Levesque 2017), see Section 2.3.3.

2.3 Convection

This Section 2.3 is adapted from Maeder (2009) and Kippenhahn et al. (2013), unless when stated otherwise.

Convection is the basic form of energy transport in stars, along with radiative transfer. It is a turbulent motion of material heated from below.

2.3.1 Schwarzschild and Ledoux Criterion

For an idealised moving cell of material, we can neglect horizontal variations of the mean molecular weight μ, assuming that the cell keeps its composition. We also neglect variations of pressure, assuming the cell is at an hydrostatic equilibrium with its surroundings, which is valid only if the velocities are subsonic. We also define pressure scale height as

$$H_p \equiv -\frac{\mathrm{d}r}{\mathrm{d}p}p, \tag{2.30}$$

which describes the length characteristic of the radial variation of pressure. Then, we can finally write the stability condition as

$$\frac{\mathrm{d}\ln T_{\mathrm{ext}}}{\mathrm{d}\ln p} < \frac{\mathrm{d}\ln T_{\mathrm{int}}}{\mathrm{d}\ln p} + \frac{\varphi}{\delta}\frac{\mathrm{d}\ln \mu_{\mathrm{ext}}}{\mathrm{d}\ln p}, \tag{2.31}$$

where $\varphi = \frac{\partial \ln \rho}{\partial \ln \mu}$ and $\delta = -\frac{\partial \ln \mu}{\partial \ln T}$. The subscript **int** corresponds to properties within the cell, and the subscript **ext** to the background material. This can be rewritten using gradients as

$$\nabla_{\mathrm{ext}} < \nabla_{\mathrm{int}} + \frac{\varphi}{\delta}\nabla_{\mu}, \tag{2.32}$$

which is the Ledoux criterion for convective stability. If we assume the background is also chemically homogeneous, such as in regions, where nuclear burning does not produce heavier elements, then we can write

$$\nabla_{\mathrm{ext}} < \nabla_{\mathrm{int}}, \tag{2.33}$$

which is the Schwarzschild criterion. Furthermore, if we assume a layer, where all energy is transported by radiation and that the cell moves adiabatically, i.e., it does not exchange any heat with the surroundings medium, then we can rewrite the criterion as

$$\nabla_{\mathrm{rad}} < \nabla_{\mathrm{ad}}, \tag{2.34}$$

while Figure 2.3 shows the course of these terms in a massive star. In both of these criteria, if the inequality is fulfilled, a layer of material is stable and thus no convection occurs. But if the left-hand side is larger, than the layer becomes dynamically unstable. That may happen due to increase of flux or opacity.

In conclusion, we can write all the versions of the criteria together as

$$\nabla_{\mathrm{rad}} > \nabla_{\mathrm{ext}} > \nabla_{\mathrm{int}} > \nabla_{\mathrm{ad}}, \tag{2.35}$$

which expresses the relation between gradients in a convective zone.

2.3.2 Mixing-Length Theory

As shown in both criteria, Equations 2.32 and 2.33, the convection is a non-local process, i.e., it depends on properties of the surrounding medium. To simplify the computation of stellar models, the mixing-length theory (Böhm-Vitense 1958) is applied. It assumes that we can use an average cell, which allows us to determine properties of convection based

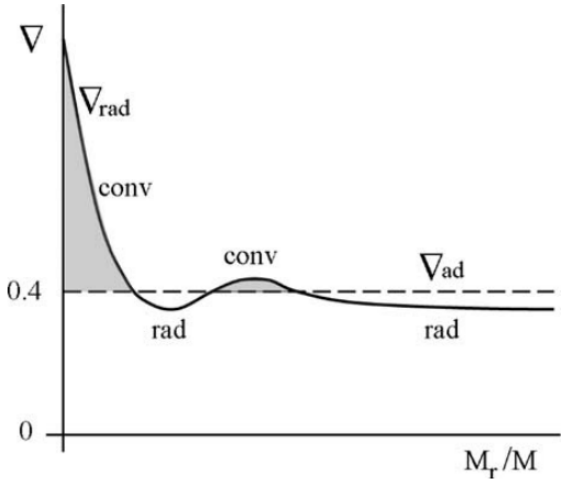

Figure 2.3: Schematic representation of the course of the terms in the Schwarzschild criterion as a function of mass in a massive star. In RSGs, the radiative zones would be much smaller, if present at all (Levesque 2017). Adapted from Maeder (2009).

on local properties. The length, over which the cell is able to sustain itself, is called mixing length l. Usually, it is defined using the pressure scale height as

$$l\alpha = H_p, \tag{2.36}$$

where α is a coefficient, usually given as ≈ 1, as we do not expect that the cell would be able to keep its identity over several scale heights. Current estimates lead to a value of $\alpha \approx 1.6$.

2.3.3 Convection in Red Supergiants

In RSGs, the large radiative pressure coupled with high opacity in cool envelopes favours convection. The cores and shell fusion regions of RSGs are also convective. Coupled with the convective envelopes, this makes the RSGs nearly fully convective (Levesque 2017), as shown in Figure 2.4.

Due to the high opacity and radiative force, the envelope may reach the Eddington limit (Equation 2.29), i.e, $\Gamma \to 1$, or even become supra-Eddington. This generates a density inversion in the convective envelope, i.e, the density grows in the convective envelope, causing an inward force due to gas pressure. The density inversion phenomenon introduces computational difficulties for evolutionary models. In new models, Agrawal et al. (2022) further investigated this phenomenon and they were able to compute the evolution up to next evolutionary stages.

It is often necessary to use non-adiabatic treatment of the convection, such as in layers, where the ionization of hydrogen and helium are incomplete. Furthermore, the approximation of subsonic motions used in Equation 2.31 is no longer valid due to high convective velocities. The ratio of (convective) velocity to sound speed a is given by Mach number $\mathbb{M}$, which is typically very low in most of stars. However, in the convective envelopes of RSGs, it reaches a number of about five or more, producing shocks (Chiavassa

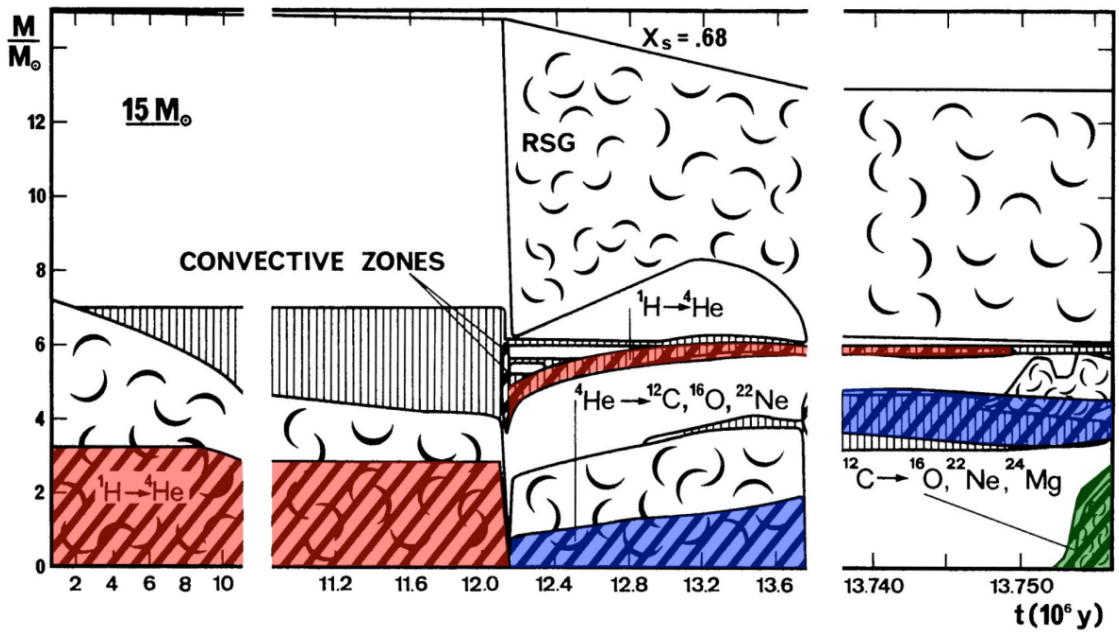

Figure 2.4: Kippenhahn diagram, i.e., interior evolution of a star, for a $15\,\mathrm{M}_\odot$ star. RSG phase is in the middle of the diagram. Thick hatched regions indicate efficient nuclear fusion, curly regions indicate convective zones and the vertically hatched regions indicate layers, where chemical composition was changed by previous convection. Adapted from Lamers & Levesque (2017) and Maeder & Meynet (1987).

& Freytag 2015; López Ariste et al. 2018), and thus complicating the standard treatment of mixing-length theory. Thus, the acoustic flux becomes important in the convective envelopes of RSGs and we need to account for turbulent pressure. Turbulent acceleration is given as

$$\boldsymbol{g}_{\mathrm{turb}} = -\frac{\alpha}{\vartheta\rho}\frac{\mathrm{d}F_{\mathrm{turb}}}{\mathrm{d}a}\frac{\boldsymbol{r}}{r}, \tag{2.37}$$

where F_{turb} is the mechanical flux due to turbulent motions, ϑ is a numerical factor in the order of unity, and $\alpha \approx 0.3$. Near the stellar surface, the acceleration is directed outwards. There exists a limit of total zero gravity at the surface, i.e., $\boldsymbol{g}_{\mathrm{tot}} = \boldsymbol{g}_{\mathrm{grav}} + \boldsymbol{g}_{\mathrm{rad}} + \boldsymbol{g}_{\mathrm{turb}} = 0$, which gives

$$\frac{GM}{r^2}(1-\Gamma) + \frac{\alpha}{\vartheta}\frac{\mathrm{d}F_{\mathrm{turb}}}{\mathrm{d}a} = 0. \tag{2.38}$$

The last term becomes negative and opposes gravity, as the turbulent flux decreases outwards. This stability limit is known as de Jager limit (de Jager 1984). It means that photosphere may dissipate due to the flux of turbulence and radiative pressure. Meanwhile, the Eddington limit is due to the radiative force only and larger pressure causes the dissipation to become relevant deeper in the photosphere. The de Jager limit likely explains, why there are no RSGs with luminosity $\log\left[\frac{L}{\mathrm{L}_\odot}\right] > 5.5$, as the mass-loss rates are significantly enhanced.

Furthermore, for some models the de Jager and Eddington limit also mostly explain, why massive stars with $M \geq 25\,\mathrm{M}_\odot$ are not able to cool enough to become (or remain)

a RSG star. Their envelopes become unstable, allowing for severe mass loss to occur. Eventually, these stars begin to evolve to the left in the HR diagram again (Ulmer & Fitzpatrick 1998; Lamers & Levesque 2017; Levesque 2017). The lack of super luminous cool stars is known as the Humphreys-Davidson limit (Humphreys & Davidson 1979).

Ekström et al. (2012), Meynet et al. (2015) and Levesque (2017) suggested that the supra-Eddington mass-loss could be the missing piece to better constraining the mass-loss process in RSGs. Meynet et al. (2015) noted that even small changes to mass-loss rates can have a dramatic effect on evolutionary tracks, therefore it is necessary to better constrain the mass-loss process. Ekström et al. (2020) reviewed the state of modelling of massive stars and points out that neither convection or mass loss arise naturally in the commonly used 1D models, therefore they are included only by various prescriptions.

Giant Convective Cells

Schwarzschild (1975) predicted that the surface of RSGs is covered by a small number of giant convective cells, which was in agreement with the mixing-length theory by Böhm-Vitense (1958). These predictions were supported by both simulations (e.g., Freytag et al. 2002) and observations (e.g., Josselin & Plez 2007; López Ariste et al. 2018). Chiavassa et al. (2009) showed that pressure scale height should be treated more precisely and modified it as

$$H_p = -\frac{kT_{\mathrm{eff}}}{g\mu m_{\mathrm{H}}}\left(1+\beta\gamma\left(\frac{v_{\mathrm{turb}}}{a}\right)^2\right), \tag{2.39}$$

where m_{H} is the mass of hydrogen, γ is the adiabatic exponent for a perfect gas and β is related to anisotropy of the velocity field. This considerably increases the pressure scale height and gives a good match with observations of Betelgeuse (Chiavassa et al. 2010).

2.4 Radial Pulsations

This Section 2.4 is adapted from Maeder (2009) and Kippenhahn et al. (2013), unless when stated otherwise.

Oscillations are frequent in the nature. In stars, generally, they are induced, when a layer increases its temperature, while the opacity also increases. The high opacity makes it difficult for the layer to lose its excess energy in another way than by expanding. As the layer expands, its temperature and opacity decrease and eventually, the layer can lose its excess energy. The gravity force pulls the layer back, causing it to contract and thus heat up again. The cycle repeats, as the star attempts to restore equilibrium. The inverse behaviour of opacity (usually it decreases with growing temperature) is typically present in layers with partial hydrogen or helium ionization.

Such conditions are present mainly in stars that departed the main sequence, and thus they become variable. The oscillations are highly periodic in many types of variable stars, such as in the Cepheids. Meanwhile, in RSGs the situation is more complex, mainly due to the interplay of pulsations with the large-scale convection.

2.4.1 Non-adiabatic Oscillations

The layer may exchange its heat with other layers, therefore it is necessary to consider non-adiabatic effects, as these effects may drive or damp the pulsations.

To examine the stability of pulsations, we can use the stability conditions, given as

$$-(\kappa_T \nabla_{\mathrm{ad}} + \kappa_P) - \frac{4}{3\gamma_1} + 4\nabla_{\mathrm{ad}} \geq 0, \tag{2.40}$$

where κ_T and κ_P are logarithmic derivatives of opacity by temperature and pressure, respectively, and where the change of density during compression is given by the first adiabatic exponent for a general equation of state $\gamma_1 = \left(\frac{\mathrm{d}\ln P}{\mathrm{d}\ln \rho}\right)_{\mathrm{ad}}$. We will now examine the terms present in the equation. Figure 2.5 shows the stability condition for a Cepheid star.

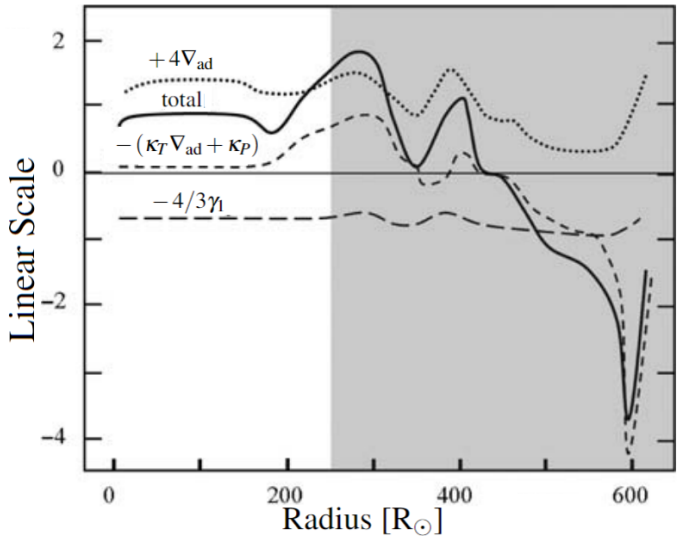

Figure 2.5: Stability condition (Equation 2.40) and its three terms for a Cepheid star. The grey area is an optically thick envelope. In the white area, the optical depth is $\tau > \frac{2}{3}$. Adapted from Maeder (2009).

The κ Mechanism

The first term in Equation 2.40 influences stability of pulsations most significantly. Opacity is higher during the contraction, which drives the pulsation, while during the expansion, the opacity drops and energy is released. Therefore, this term is positive and has a stabilising effect in outer layers, while it is negative and has a destabilising effect in inner layers.

The γ Mechanism

In the partial ionization zone, ∇_{ad} decreases and it may cause the first term in Equation 2.40 to be negative, while the third term becomes negligible. Thus, this may lead to instability.

Radiative Heating

The second term in Equation 2.40 is always destabilizing, as the density increases during compression. Therefore, more energy is retained.

Radiative Damping

The third term in Equation 2.40 is always stabilizing. It expresses the change of temperature during compression, therefore how much heat can be lost by the radiative damping.

The value of ∇_{ad} also plays a significant role in limiting the amplitude of pulsations. If pulsations become too large, i.e., a layer is fully recombined during an expansion and fully ionized during contraction, this would lead to large ∇_{ad}, which would have a stabilizing effect.

Furthermore, the amplitude of pulsations is also limited by the amount of damped heat. To describe non-adiabatic effects, the damping timescale τ_{d} is used, which is the time it would take for a layer to radiate all its heat away. The ratio of period of pulsations to τ_{d} determines the importance of non-adiabatic heat damping during a pulsation cycle.

The ε Mechanism

Changes to the rate ε of the nuclear energy production may also drive instabilities. However, in most stars this mechanism cannot overcome damping, as this type of instability is driven only in regions close to stellar cores or burning shells.

2.5 Simulations

The phenomena mentioned in this chapter make it very challenging to simulate atmospheres of RSGs, especially because of the large-scale convective motions. For hydrodynamical modeling of convection, it is necessary to include the whole star in a simulation. For that reason, the proper simulations of RSGs were not computationally possible for a substantial time.

Freytag et al. (2002) succeeded in doing first 3D radiative hydrodynamics simulations of atmospheres of RSGs, using the newly developed COB5BOLD code with a star-in-a-box approach. They were able to confirm the presence of a small number of giant convective cells on the surface, as per prediction by Schwarzschild (1975). They were also able to reproduce brightness variations and formation of shocks.

These results were followed upon by Chiavassa et al. (2009, 2011), who developed a new 3D pure-LTE radiative transfer code Optimd3D. They confirm the results from Freytag et al. (2002) and further simulate the evolution of the atmosphere. The simulations showed that the giant convective cells have strong downdrafts that can penetrate very deep inside the star, as far as to the convective stellar core. Chiavassa et al. (2010) compared the simulations to interferometric observations of Betelgeuse and found an excellent agreement. Furthermore, Chiavassa & Freytag (2015) showed that the acoustic waves produced by supersonic convective motions propagate outwards into the atmosphere, where they are compressed and amplified, producing shocks. Kravchenko et al. (2019) found that the

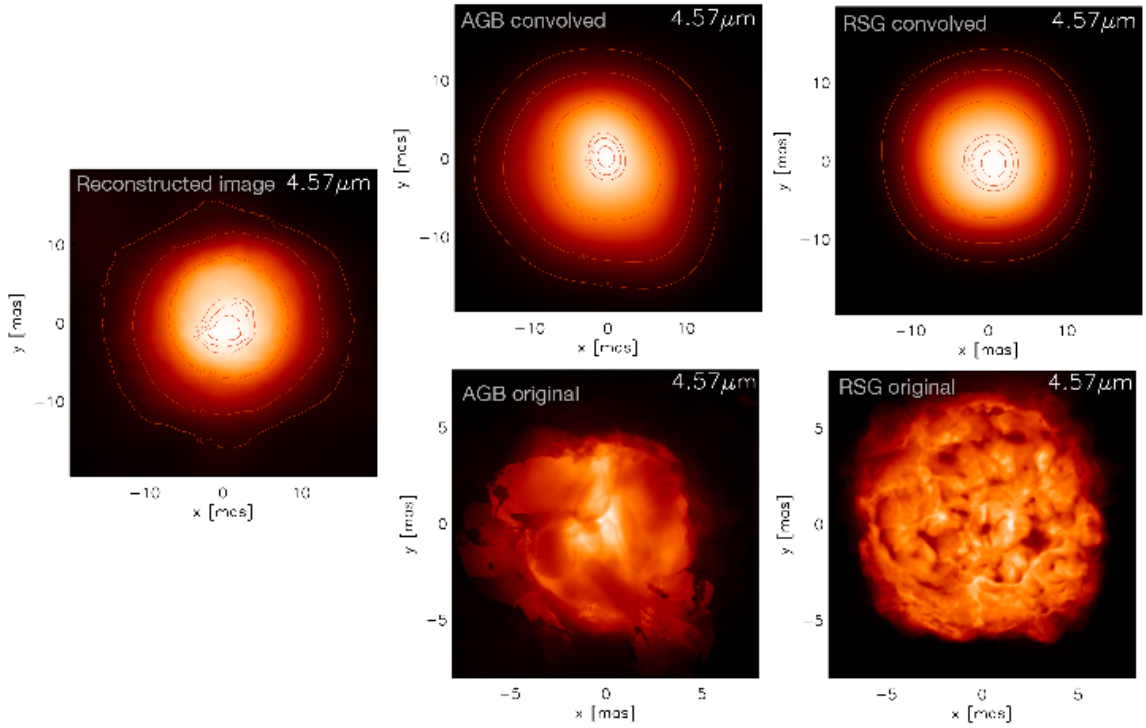

Figure 2.6: Comparison between an interferometric observation of VX Sgr (left picture) and COB5BOLD simulations of an AGB and a RSG star (bottom right panels). The simulations were convolved with the interferometric beam (upper right panels), in order to be able to compare it to the observations. Adapted from Chiavassa et al. (2022).

sound-crossing timescale in outer layers is of the same order as the length of the cycles of cooling and heating of material, i.e., the hysteresis loops. An example of 3D radiative hydrodynamics COB5BOLD simulations is shown in Figure 2.6.

Nonetheless, 1D and 3D convection and pulsation models of RSGs fail to predict the extended molecular envelopes, which were proven by observations (Section 1.2.1). Therefore, this suggests that neither pulsations nor convection alone drive the mass-loss process (Arroyo-Torres et al. 2015; Wittkowski et al. 2021).

The situation is better in regards to reproducing the observed spectra, especially in the optical and infrared region (Levesque 2017). Despite many approximations taken, such as spherical symmetry, LTE and mixing-length theory, the models are able to produce a reasonable agreement with the observed spectra, namely MARCS (Plez et al. 1992; Gustafsson et al. 2008) and PHOENIX (Lançon et al. 2007), which allows us to determine physical properties of RSGs. Lobel & Dupree (2000) developed non-LTE spherically symmetric models of Betelgeuse's photosphere and inner chromosphere. This was followed upon by Lobel (2010), who succeeded in correctly modelling the emission features in the UV.

Recently, Davies & Plez (2021) were able to add the influence of a constant stellar wind model into the MARCS atmospheres (Figure 2.7), which opened a new window to studying the mass-loss rates of RSGs. They managed to reproduce for the first time many of the observed features, such as the extended molecular envelopes, the increased molecular

TiO absorption at fixed effective temperature, which considerably shifts the spectral type of a star, and the mid-IR excess from molecular bands, which is caused by high mass-loss rates.

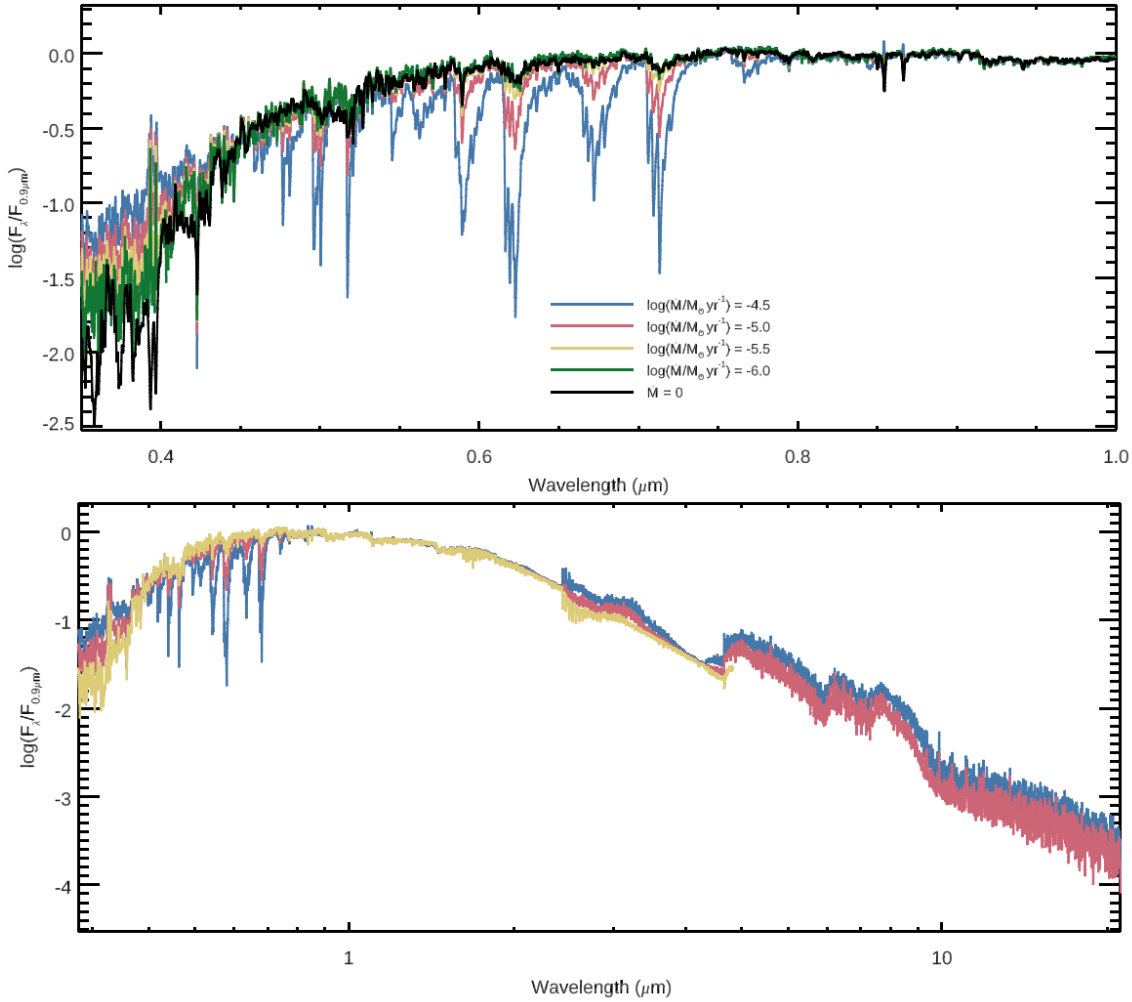

Figure 2.7: Model spectra for various values of mass-loss rates, for a star with $T_{\rm eff} = 3800\,$K, $\log g = 0$ and solar metallicity. *Upper panel:* zoomed optical region. *Lower panel:* optical and infrared region with selected mass-loss rates. The same color coding applies. Adapted from Davies & Plez (2021).

This was followed upon by González-Torà et al. (2023), who were able to improve upon the previous models, by semi-empirically adding a stellar wind to the model atmospheres. They correctly reproduced the spectroscopic and interferometric properties of RSGs.

Chapter 3

The Tomographic Method

3.1 Aims of the Method

The tomographic method that studies different slices of stellar atmospheres was first introduced by Alvarez et al. (2000, 2001a). It allows us to probe different layers of stellar atmospheres and thus to reconstruct depth-dependent velocity fields, by grouping lines based on their formation optical depth (Alvarez et al. 2001b). These groups are called masks. Therefore, we can use this method to study different processes in atmospheres.

One of the main aims of this method was to study the dynamics of the atmospheres of long-period variables. Specifically, they aimed to test the Schwarzschild scenario (Schwarzschild et al. 1948; Schwarzschild 1952), which could explain, why lines (or cross-correlation functions) of some Mira-type stars appear double peaked during their maxima of brightness.

3.1.1 Schwarzschild Scenario

The Schwarzschild scenario describes upward propagation of a shock wave through a photosphere (Figure 3.1). The cycle begins, when the material in photosphere is in-falling and therefore all the spectral lines are red shifted. Meanwhile, a new shock wave forms below the region, where the lines form. Once the shock front reaches the photosphere, material in the innermost layers begins to rise, therefore the innermost layers are characterized by a blue shifted component of spectral lines. As the shock front ascends, the intensity of the blue component increases, while the red component diminishes. Once the shock front passed through the photosphere, all the matter is rising and only the blue shifted component remains (Schwarzschild et al. 1948; Schwarzschild 1952; Alvarez et al. 2000; Kravchenko et al. 2019).

3.2 Development

3.2.1 First Results

Alvarez & Plez (1998) successfully applied the tomographic method to Mira variable star RT Cyg and recovered Schwarzschild scenario, i.e., the cross-correlation functions

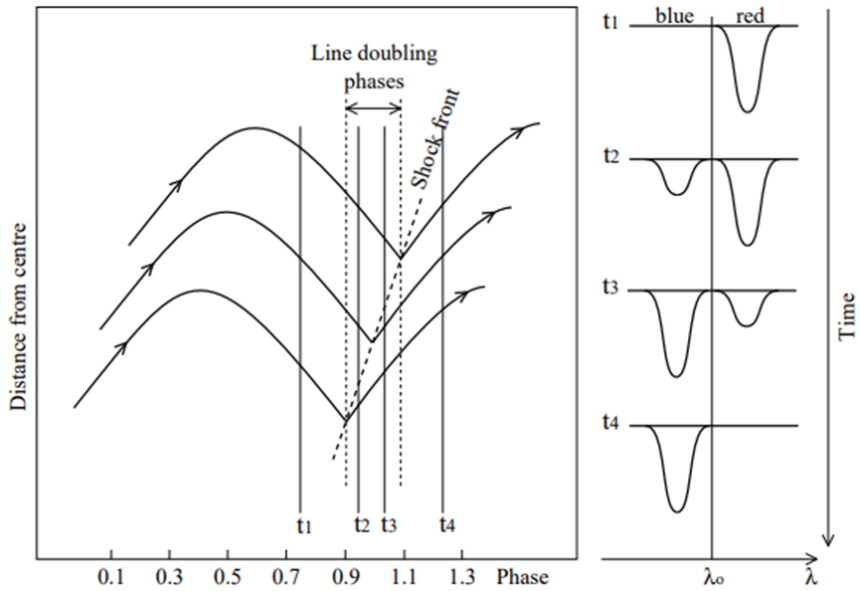

Figure 3.1: Schwarzschild scenario. Vertical axes on the left panel show the distance from a centre of a star and the time increases to the right. The right panel shows the intensity of blue and red shifted components of a spectral line and the time increases downwards. The figure shows that a secondary blue-shifted peak appears during the time t_2, representing the rising material within an atmosphere. It eventually becomes the dominant feature. Adapted from Alvarez et al. (2000).

(CCF) showed propagation of shock waves through the atmosphere (Figure 3.2). They also analysed the temporal evolution of Balmer emission lines in relation to absorption-line velocities in an attempt to find the origin of the complex profile of Hα emission line. For the construction of masks, they used MARCS (1D LTE) model atmospheres with Turbospectrum (1D LTE) radiative transfer code (Plez et al. 1992) .

Nonetheless, many other long period variable (LPV) stars showed no line-doubling, as it was demonstrated for example on Mira-type star X Oph in Alvarez et al. (2000). A subsequent study by Alvarez et al. (2001b), which examined a much larger sample of long-period variables, suggested that compact LPVs are more prone to exhibit line-doubling phenomena than large sized LPVs. In the latter case, the CCFs become asymmetric rather than showing clear line-doubling.

However, the method still had some significant limitations. Namely, there was no correlation of the masks with geometric depth, which made it difficult to make quantitative predictions, e.g., velocity of the shock front. Furthermore, Alvarez et al. (2000) used Eddington-Barbier approximation (Equation 2.13) in their computations, which assumed that lines form in layers, where $\tau = \frac{2}{3}$, and thus also the line depression.

Josselin & Plez (2007) applied the tomographic method to several RSGs. They revealed strong line asymmetries, probably of convective origin, while the line-doubling appear less prominent in RSGs than in Mira-type stars. The convective motions they found are supersonic, variable on a timescale of a few hundred days. They proposed that the turbulent pressure produced by the convective motions may play a role in the mass-loss process of RSGs, in combination with radiative pressure on molecular lines.

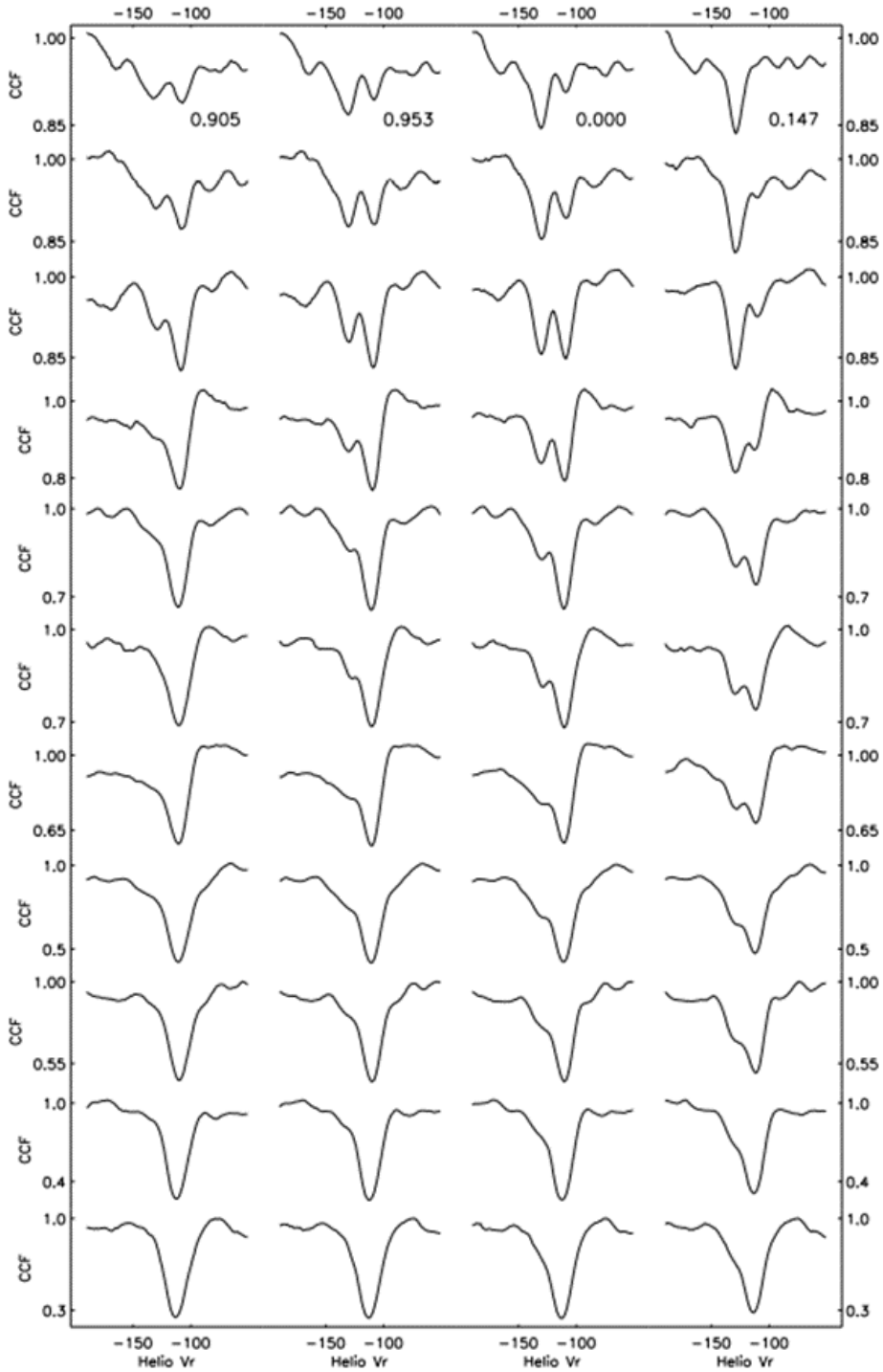

Figure 3.2: Cross-correlation functions of Mira-type star RT Cyg show a successful application of the tomographic method. Time increases to the right, and the distance from the centre of a star increases downwards. A shock wave propagates from the innermost layer to layers above it. By the time it reaches the upper layers, the innermost CCFs no longer show any significant secondary component. Adapted from Alvarez et al. (2000).

3.2.2 Validation

The tomographic method was fully validated almost two decades later by Kravchenko et al. (2018). They added the line-depth contribution function (Equation 3.1) to correctly assess the formation depth of spectral lines, using MARCS (1D LTE) model atmospheres (Gustafsson et al. 2008), CODEX (1D LTE) model atmospheres (Ireland et al. 2008, 2011) and Turbospectrum (1D LTE) radiative transfer code (Plez 2012; Lion et al. 2013). They successfully reproduced results by Alvarez et al. (2001a) for Mira variable V Tau. Due to convection in real stars, the line formation may be spread over different optical depths than in 1D models, therefore they also tested the method in 3D radiative-hydrodynamics (RHD) simulation, using CO5BOLD dynamical atmospheres (Freytag et al. 2017), which correctly reproduces the effects of non-radial waves and convection (Chiavassa et al. 2011), and Optim3D (pure-LTE) radiative transfer code (Chiavassa et al. 2009), which takes Doppler shifts due to convective motions into consideration. Kravchenko et al. (2018) were able to confirm that the tomographic method is indeed able to correctly recover the velocity distribution in 3D as well.

Kravchenko et al. (2019) showed the application of the tomographic method to high-resolution spectroscopic observations of a RSG star μ Cep. They related observed photometric variability with the photometric and temperature variability. The hysteresis loops are characterized by a timescale of a few hundred days and are similar to the ones observed in Betelgeuse and they found that physical processes related to convection are likely responsible for the variations. They further found that the timescales are similar to sound-crossing timescales, therefore it suggests that acoustic waves originate from disturbances in convective flow and propagate upwards to surface layers, where they modulate the convective energy flux. Figure 3.3 displays velocity maps for snapshots along the hysteresis loops for a 3D RHD model of a star of similar parameters as μ Cep.

As the final part of the tomography of cool giant and supergiant star atmospheres series, Kravchenko et al. (2020) used spectro-interferometric observations of Mira-type AGB star S Ori to derive a relation between the optical and geometric scale, using CODEX (1D LTE) model atmospheres (Ireland et al. 2008, 2011), COB5BOLD 3D dynamical model atmospheres (Freytag et al. 2017) and Optim3D (pure-LTE) radiative transfer code (Chiavassa et al. 2009). This was accomplished by extracting interferometric visibilities at wavelengths contributing to the tomographic masks. The visibilities were fitted with an uniform disk model to estimate the relative spatial extensions at different optical depths. These results were compared to 1D and 3D models, which gave a similar relation between optical and geometrical depths, thus further validating the tomographic method. The results also revealed a complex multi-layered structure of the atmosphere of S Ori, unlike predicted by some previous theories for AGB stars. The derived relation shall allow us to measure shock wave propagation velocity in real stars for the first time and thus improve our models and give us means to better understand the mass-loss mechanism in cool giants and supergiants.

Additionally, Kravchenko et al. (2021) further applied the tomographic method to Betelgeuse. They revealed two shock waves, which preceded the Great Dimming event.

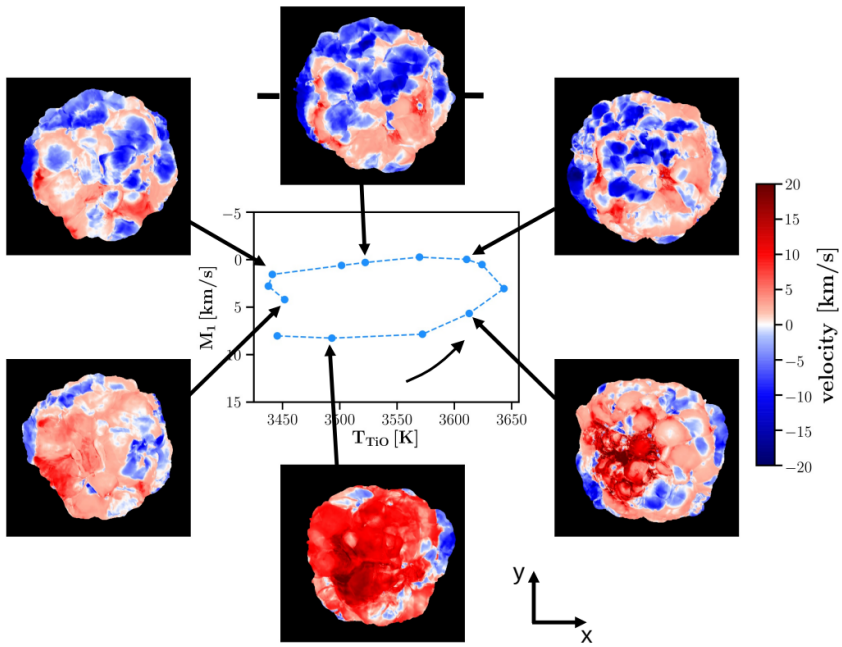

Figure 3.3: 3D radiative-hydrodynamics simulation of a star with parameters similar to μ Cep shows line-of-sight velocity maps (for the observer located in front of the figure) for snapshots along the hysteresis loop of mask C4. Red color corresponds to in-falling material and blue color to rising material. Adapted from Kravchenko et al. (2019).

3.3 Application

3.3.1 Line-depth Contribution Function

As it was mentioned before, Alvarez et al. (2000) used the Eddington-Barbier approximation to determine the optical depth of lines formation. However, Magain (1986) demonstrated that this approximation is correct for strong lines only. To correctly determine the valid depth of line formation, Kravchenko et al. (2018) used the contribution function to the absolute line depression (CFLD)

$$\mathrm{CFLD}_{\mathrm{disk}}(\log\tau_0,\lambda) = 2\pi(\ln 10)\frac{\tau_0}{\kappa_{\mathrm{c},0}}\int_0^1 \kappa_{\mathrm{line}_\lambda}(I_{\mathrm{c}_\lambda} - S_{\mathrm{line}_\lambda})\mathrm{e}^{-\tau_\lambda/\mu}\,\mathrm{d}\mu \tag{3.1}$$

(Magain 1986; Albrow & Cottrell 1996), which is a solution of radiative transfer (Equation 2.12) for line depression, where $\tau_0 = \int \kappa_{\mathrm{c},0}\rho\mathrm{d}x$ is the optical depth of the continuum at a reference optical depth λ_0, $\kappa_{\mathrm{c},0}$ the continuum absorption coefficient at reference wavelength λ_0, I_{c} the continuum intensity, I_{line} the line intensity, κ_{line} the line absorption coefficient, S_{line} the line source function and $\tau_\lambda = \int \kappa_\lambda\rho\mathrm{d}x$ the optical depth along a ray. The equation is given in a $\log\tau_0$ scale.

All the necessary quantities for the computation were acquired from synthetic spectra based on the radiative-transfer codes listed in the previous section. τ_0 serves as a proxy for a geometrical depth x. The optical depth τ_λ is related to its reference counterpart τ_0 as

$$\frac{\mathrm{d}\tau_\lambda}{\mathrm{d}\tau_0} = \frac{\kappa_\lambda}{\kappa_{\mathrm{c},0}} \tag{3.2}$$

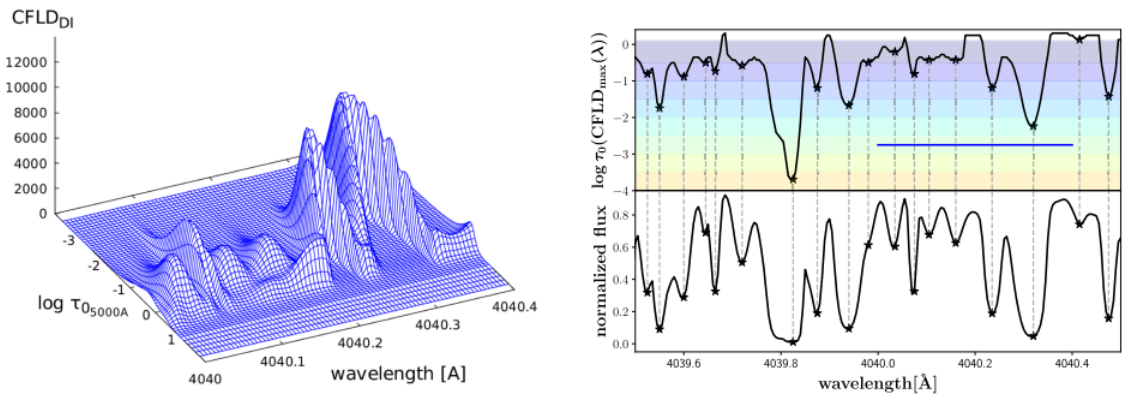

Figure 3.4: *Left panel:* CFLD for a 1D model of a red supergiant. *Right panel:* the upper panel shows a depth function corresponding to the Equation 3.1 in $\lambda - \log\tau_0$ plane, while the lower panel shows a corresponding synthetic spectrum. The bottom right panel demonstrates that cores of spectral lines form in outer layers, while the wings form in deeper layers. Adapted from Kravchenko et al. (2018).

Figure 3.4 shows the computed CFLD function for a disk. The set of reference optical depths τ_0 corresponding to the maximum of the function for each wavelength λ defines a crest line, which Kravchenko et al. (2018) calls a depth function $D(\lambda)$, given in a $\log\tau_0$ scale. The depth function calculates the optical depth of lines formation, for lines contributing at wavelength λ.

3.3.2 Construction of Numerical Masks

Kravchenko et al. (2018) computed the reference optical depth scale τ_0 using continuum opacities at 5000 Å (used in this work as well). Then the atmosphere can be split into layers based on the selected ranges of optical depths (see Figure 3.5), for which the spectral masks are constructed. The lines in each mask are represented by a Dirac-like distribution.

3.3.3 Mask Cross-correlation

The acquired masks are then cross-correlated with series of spectra (observed or synthetic).

The cross-correlation technique has a long history in astrophysics, some of the first uses are for example from Simkin (1974) and Tonry & Davis (1979). It is one of the most popular procedures in astrophysics for deriving Doppler velocity shifts, superior to simply comparing central wavelengths (Allende Prieto 2007). It is defined as

$$\mathrm{CCF}(\Delta x) = s(\Delta x) \otimes t(\Delta x) = \frac{1}{N\sigma_s\sigma_t}\sum_{x=1}^{N} s(x)t(x-\Delta x), \tag{3.3}$$

where s is a stellar spectrum, t is a template (synthetic) spectrum, σ is the root mean square and N is the number of bins based on sampling. If s is the same as (or closest to)

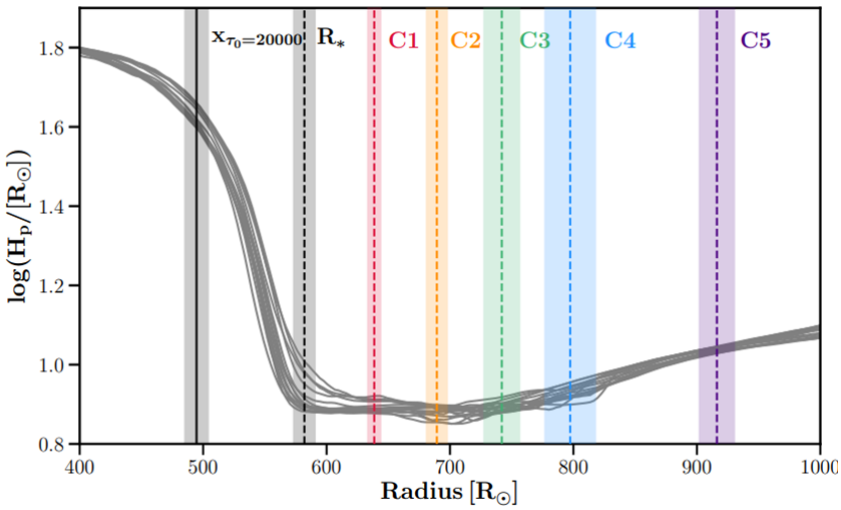

Figure 3.5: Pressure scale height profiles (gray plots) as a function of shell radius for set of 3D simulations snapshots. The vertical coloured lines show physical locations of tomographic masks. The location of R_* corresponds to Rosseland optical depth ($\tau_{\mathrm{Ross}} = \frac{2}{3}$). Adapted from Kravchenko et al. (2019).

t but shifted by a number of d units, the CCF will have a peak at $x = d$. Therefore, this technique is based on averaging profiles of spectral lines in the spectrum, by comparing a synthetic spectrum with observed spectrum, resulting into cross-correlation function, where the location of the peak of corresponds to the Doppler velocity shift.

Combined with the tomographic masks, the resulting CCFs provide us with the ”average” shape of spectral lines forming at a given range of optical depths, and therefore we can also uncover a corresponding velocity field.

Chapter 4

Summary of Results

The first part of the results was published in a scientific journal, while the second part is going to be submitted. The papers are available in Appendix A (Jadlovský et al. 2023) and Appendix B.

4.1 Paper I: Analysis of photometric and spectroscopic variability of Betelgeuse

In the first paper, which was the continuation of the results from the bachelor's thesis (Jadlovský 2021), we analysed the variability of Betelgeuse using available high-quality archival spectral and photometric data. Our main intention was to analyse variability of radial velocity and brightness in different spectral regions.

As part of the spectral analysis in the optical region, we used about 15 spectra from different instruments to determine radial velocity based on selected lines, while we also adapted results of radial velocity measurements from Granzer et al. (2021). For the ultraviolet region, the analysis was more complicated, as spectra from spectrographs onboard Hubble Space Telescope (HST) are taken at different positions at the surface of Betelgeuse, in different ultraviolet regions and with different sizes of apertures, while the archive also included several faulty spectra. In the end, we were able to determine radial velocity of the Betelgeuse's surface using about 20 observations (about 70 subexposures from different parts of the surface in total), based on 2 groups of selected lines in near ultraviolet region. When available, we used high-level processed HST spectra from ASTRAL archive (Ayres 2014). For the brightness analysis part, we used photometric filters spanning from ultraviolet to near infrared region.

We found that variability of radial velocity and light curve are connected and periods that we determined based on photospheric velocity and photometric data correlate well with each other as well as with the values from literature. Meanwhile, the velocity at the base of outflowing stellar wind also showed variability, with a maximum during the Great Dimming, but due to limited time coverage it was not possible to conclusively determine its period. Although, based on the data it is clear that the timescale of this variability is longer than that of the fundamental mode of pulsations and it is likely driven by processes in outer atmosphere of Betelgeuse. Similarly, based on the displacement of radial velocity across

the Betelgeuse's surface in near ultraviolet region, it was not possible to unveil rotational effects.

In regards to the Great Dimming of Betelgeuse, the photometric data showed that the brightness in near infrared region underwent only a very small decrease during the Dimming, relative to the decrease of optical brightness, which suggests that the drop in brightness could have been caused by an extinction in optical region, or possibly due to a decrease of effective temperature. The maximum of stellar wind velocity supports that the Dimming was preceded by an outflow of material. After the Dimming, the mean period appeared to be shorter, as was also shown by other studies (e.g., Dupree et al. 2022).

4.2 Paper II: The Great Dimming of Betelgeuse: the photosphere as revealed by tomography during the past 15 years

Work on the second paper was initiated as part of the internship in the Leibniz Institute for Astrophysics Postdam (AIP) in summer 2022. The main inspiration for this project was the application of the tomographic method (see Section 3) to Betelgeuse by Kravchenko et al. (2021), which even with the small dataset was able to reveal a lot of information about Betelgeuse's atmosphere and the Great Dimming. Coupled with 15 years of nearly continuous high-resolution spectroscopic time-series of Betelgeuse (Granzer et al. 2022), obtained using AIP's STELLA échelle spectrograph (SES, Strassmeier et al. 2004), the tomographic method could reveal long-term variability of Betelgeuse's photosphere in an unprecedented detail. Therefore, the application of the tomographic method to AIP's spectral dataset is the main subject of the second paper.

We combined the line lists from Kravchenko et al. (2019) with a spectral template for Betelgeuse (see Figure 4.1 for the distribution of lines in a spectrum). The acquired masks were cross-correlated with STELLA-SES time-series of Betelgeuse, which consists of about 2500 spectra in optical region (as of January 2023). After the application of order-by-order cross-correlation procedure and subsequent cleaning, we received about 1500 good CCFs for each mask. Therefore, we were able to analyse a variability of 5 layers of Betelgeuse's photosphere. Apart from this, we included photometric data in order to be able to correlate the photospheric motions with brightness variability. We also determined relative temperatures changes based on line-depth ratio of V I and Fe I, as introduced by Gray (2008).

The high-precision velocity results provided a unique insight into the long-term evolution of the photosphere and its connection to brightness variability. We found phase shifts between the variability of photospheric layers, the photometric variability, and relative temperature changes, as well as crossing timescales of shocks in the photosphere. We constructed hysteresis loops, i.e., evolution of temperature and velocity, which illustrates the cycles of cooling and heating of material in atmosphere. The results suggest that the material is not able to complete the loops during timescales that correspond to oscillations of higher overtones, but only during the fundamental mode of pulsations. This, along with the length of cycles, have implications for convective and sound-crossing timescales in the photosphere. We also found that pulsations of higher overtones are being excited (and

damped) in the atmosphere of Betelgeuse more commonly than previously thought, which may be related to increased data sampling compared to other studies.

Our results also showed a unique behaviour of the photosphere during and after the Dimming. After the previously reported shock wave that preceded the Dimming (Kravchenko et al. 2021) and a subsequent outflow of material (Dupree et al. 2022; Granzer et al. 2022), the inner layers begun to in-fall faster than outer layers, causing the inner layers to expand. By the time of minimum brightness due to the Great Dimming in February 2020, the velocity reached its minimum and a second shock wave emerged, which was even more powerful than the first one, as shown by the data. During the next 2 years that followed the Dimming, the inner and outer photospheric layers were in dissonance, i.e., the inner layers were excited to a higher overtone of pulsations, while the outer layers appeared to continue their previous movement. By the beginning of 2022, the behaviour of photospheric layers appeared to be synchronized again, although all the layers now pulsated with the first overtone.

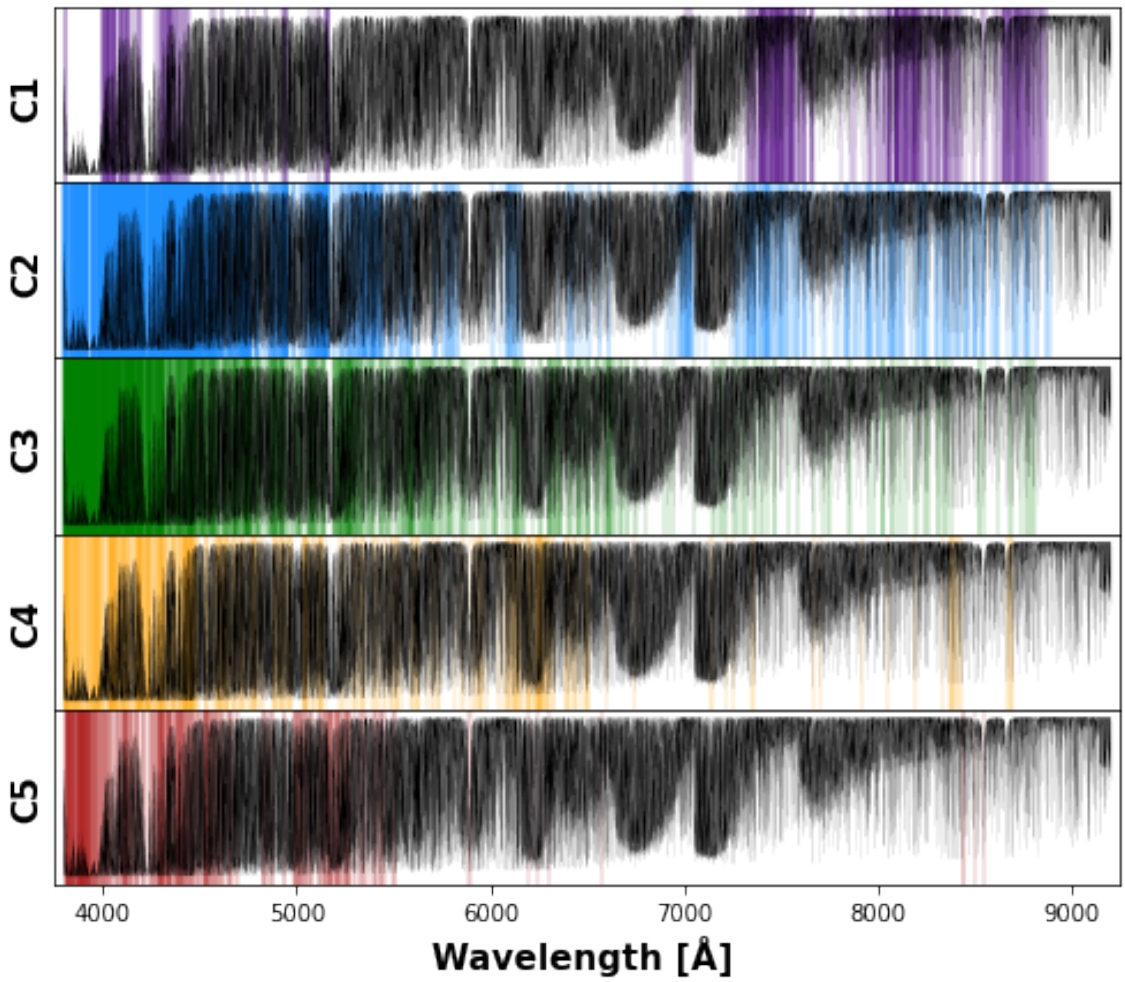

Figure 4.1: Line distribution of tomographic masks (vertical lines of various colors) used in Paper II (Appendix B) across a normalized template spectrum (black line) for cross-correlation with STELLA-SES, calculated with MARCS model atmospheres (Gustafsson et al. 2008) for $T_{\rm eff} = 3500\,{\rm K}$, $\log g = 0$ and $v_{\rm microturb} = 2\,{\rm km\,s^{-1}}$.

Conclusions and Future Insights

Despite the progress in modelling and simulations of red supergiants during the last two decades, the mass-loss process in these stars remains not well constrained and a large majority of models failed to predict the observed extended molecular envelopes, as well as several other phenomena related to mass loss and stellar wind.

While the dust-driven stellar wind in combination with pulsations is able to support the observed mass-loss rates for red giants on the asymptotic giant branch, this process does not appear to be sufficient for more massive red supergiants. The additional processes that drive the mass loss may include interplay of pulsations and convection, activity of giant convective cells, supra-Eddington instabilities or formation of strong shock waves. Another proposed process is radiative pressure on molecular lines, similar to line-driven wind of hot stars, the progenitors of red supergiants.

We investigated the variability of red supergiant Betelgeuse across a wide spectral range, using a multitude of instruments. High-resolution spectral analysis revealed the long-term dynamics in different layers of photosphere and chromosphere and yielded new insights related to pulsations of atmosphere, the line asymmetries caused by passing of shock waves or by giant convective cells, and the velocity at the base of outflowing stellar wind. These processes may contribute to the mass loss and some indeed appear correlated with the mass-loss event that caused the Great Dimming, most importantly the formation of a strong shock at the base of photosphere and a subsequent outflow of photosphere followed by a maximum of stellar wind velocity.

The two most dominant modes of variability are the fundamental mode of radial pulsations and long secondary period. The observed timescales and amplitudes of these two modes of variability vary, while low-order overtones of radial pulsations are occasionally being excited and damped. In the transition times, when the mode of variability changes, the inner and outer layers of the photosphere behave differently, until the change reaches the upper layers. Nonetheless, following the Great Dimming and the second powerful shock wave that we detected, the first overtone of radial pulsations appear dominant for a longer time than usually. Meanwhile, it is not certain whether the fundamental period is damped permanently or whether it eventually regains its dominance.

In future, we intend to expand our research to other red giants and supergiants, with a focus on the mass-loss process, using spectroscopy, spectro-interferometry and interferometric imaging. The observations will be compared to 1D models and state-of-the-art 3D radiative-hydrodynamics simulations. Simultaneously, new observations of Betelgeuse will be taken by STELLA-SES, maintained by the Leibniz Institute for Astrophysics Postdam, therefore we will be able to further closely monitor the unprecedented aftermath of the Great Dimming.

Appendix A

New Astronomy 99 (2023) 101962

Contents lists available at ScienceDirect

New Astronomy

journal homepage: www.elsevier.com/locate/newast

Analysis of photometric and spectroscopic variability of red supergiant Betelgeuse

Daniel Jadlovský *, Jiří Krtička, Ernst Paunzen, Vladimír Štefl

Department of Theoretical Physics and Astrophysics, Faculty of Science, Masaryk University, Kotlářská 2, Brno, 611 37, Czech Republic

ARTICLE INFO

Keywords:
Betelgeuse
Red supergiants
Radial velocity
Photometry
Spectroscopy
Stellar pulsations

ABSTRACT

Betelgeuse is a pulsating red supergiant whose brightness is semi periodically variable and in February 2020 reached a historical minimum, the Great Dimming. The aims of this study are to characterize Betelgeuse's variability based on available archival data and to study possible causes of light variability. Many spectra, from ultraviolet and optical regions, were evaluated for spectral analysis. The spectra were used primarily to determine radial velocities from different layers of atmosphere and their long-term evolution. Additionally, photometric data were analysed in different filters as well, to construct light curves and to determine periods of the variability. Spectroscopic and photometric variability are compared to each other and given into a context with the Great Dimming.

The two most dominant photometric periods are $P_1 = 2190 \pm 270$ d and $P_2 = 417 \pm 17$ d, while the dominant optical (photospheric) radial velocity periods are $P_{1,v_r} = 2510 \pm 440$d and $P_{2,v_r} = 415 \pm 11$d. During the same time, the radial velocity determined from ultraviolet spectra also shows variability and is distinctively different from the variability of photospheric velocity, undergoing longer periods of variability. We attribute these velocities to the velocities at the base of outflowing wind. We also report a maximum of stellar wind velocity during the Great Dimming, accompanied by the previously reported minimum of brightness and the maximum of photospheric radial velocity. After the Dimming, Betelgeuse's mode of variability has fundamentally changed and is now instead following a shorter period of ~ 200 d.

1. Introduction

Betelgeuse is a semi-regular variable star and is the brightest star in the near-infrared part of spectrum [E1], typically ranking as one of the 10 brightest stars overall. It is classified as a red supergiant of M1–M2 spectral type (Keenan and McNeil, 1989). However, despite many highest quality observations and research, several of the fundamental characteristics of Betelgeuse remain significantly uncertain.

The uncertainty lies primarily in the determination of the distance of Betelgeuse, and other physical properties tied to it. A reliable estimate of distance determined by Harper et al. (2008a) 887 ± 203 $R_\odot$ is based on multi-wavelength observations. The analysis by Joyce et al. (2020) that combines evolutionary, asteroseismic, and hydrodynamical simulations, gives a current mass of 16.5–19.0 $M_\odot$ and initial mass of 18–21 $M_\odot$.

Betelgeuse has average photospheric radial velocity $v_{\rm rad} = 21.9\,{\rm km\,s^{-1}}$ (Famaey et al., 2005). There have been issues with tracing Betelgeuse back to its birthplace, especially due to the uncertainty of the distance to the star (van Loon, 2012). Rotational velocity of Betelgeuse is higher than most other red supergiants typically have (van Loon, 2012). The projected rotational velocity that was determined from HST ultraviolet data of Betelgeuse (Uitenbroek et al., 1998) is given as $v_{\rm rot}\sin(i) \sim 5\,{\rm km\,s^{-1}}$, while a more recent study by Kervella et al. (2018) gives $v_{\rm rot}\sin(i) = 5.47 \pm 0.25\,{\rm km\,s^{-1}}$.

Betelgeuse's brightness changes on at least two different timescales (Joyce et al., 2020) that were observed since 1837 by sir John Herschel (Lloyd, 2020). Based on some of the most precise determinations of the periodicity by Kiss et al. (2006) and Chatys et al. (2019), the shorter period is $P_{\rm short} \sim 388 \pm 30$ days, and the longer period is $P_{\rm long} \sim 5.6 \pm 1.1$ years (~ 2050 days). Both vary in the exact length, and also the amplitude of photometric variability shows significant variability. While there is no clear consensus, it is mostly assumed that the shorter period is driven by atmospheric pulsations in either the fundamental or low-overtone modes, and also by oscillations due to invocation of convective cells (Kiss et al., 2006). Joyce et al. (2020) concluded that the mode of atmospheric pulsations is the fundamental mode. The longer period is most often attributed to either flow timescales of giant convection cells (Stothers, 2010) or to magnetic

* Corresponding author.
E-mail address: jadlovsky@mail.muni.cz (D. Jadlovský).

https://doi.org/10.1016/j.newast.2022.101962
Received 19 November 2021; Received in revised form 19 October 2022; Accepted 25 October 2022
Available online 28 October 2022

Table 1
List of spectra used for the radial velocity analysis. The dates are given in Modified Julian Date (MJD), which can be obtained by subtracting 2400000.5 days from the Julian date (JD).

Reference	Wavelength region [Å]	MJD [d]	Number of used spectra	Source
HST GHRS (Brandt et al., 1995)	UV (1980-3300)	48889	20	[E6]
HST STIS (Dupree et al., 2020; Ayres, 2014)	UV (2270-3120)	50821-59476	68	[E8,E7]
HARPS (Mayor et al., 2003)	OPT (3780-6910)	58891	1	[E2]
UVES (Dekker et al., 2000)	OPT (3280-5000)	52530; 56570	2	[E2]
X-shooter (Vernet et al., 2011)	OPT (2990-10190)	55166	1	[E2]
SOPHIE (Perruchot et al., 2008)	OPT (4000-6800)	54074	1	[E3]
ELODIE (Baranne et al., 1996)	OPT (4000-6800)	51204-53404	8	[E4]
FLASH HEROS (Kaufer, 1998)	OPT (3390-8630)	49868-50455	4	[E5]

activity, rotation of starspots, episodic dust formation, or a nearby companion followed by a dust cloud (Wood, 2000; Wood et al., 2004).

In October 2019 Betelgeuse begun to decrease its brightness once again. However this time, the dimming continued much further than ever before, and it reached the historical minimum by the middle of February (Guinan et al., 2020). The unprecedented event was nicknamed as The Great Dimming. The Dimming was first noticed by Guinan et al. (2019), who suggested that this dimming is due to confluence of the longer and shorter period. Betelgeuse had continued to dim until middle February, reaching a minimum of $V \sim 1.6$ mag. After that it appeared to increase its brightness again Guinan et al. (2020). Gehrz et al. (2020) observed that the Betelgeuse's brightness in infrared was largely unaffected by the Great Dimming, whereas mostly the optical wavelengths were affected. Considering that Betelgeuse is the brightest in the infrared, it suggests that the overall brightness of Betelgeuse remained mostly intact. Therefore it seems unlikely that this episode would be due to major changes within a star, but more likely due to a local surface event.

However, considering that such a dimming had never been observed before, other theories have been proposed besides the conjunction of the two periods. Levesque and Massey (2020) argued the dimming episode could not have been caused by a decrease in Betelgeuse's effective temperature, according to model atmospheres. Based on their best fit, the effective temperature dropped only from 3650 K to 3600 K, which would cause a decrease of visual magnitude $V \sim 0.17$ mag. That would definitely not be sufficient to explain the $V \sim 1.1$ mag drop in brightness. Therefore, they suggest that the decrease in V could be due to mass loss and subsequent large grain dust production that would cause an absorption, mostly in optical part of spectrum. However, Dharmawardena et al. (2020) found out the Betelgeuse has also dimmed in sub-millimetre wavelengths by about 20% during the Great Dimming. They argue the Dimming must have been due to changes in the photosphere, as sub-millimetre wavelengths are primarily dominated by Betelgeuse's photosphere. Based on their models, they were able to present other possible causes that would explain the scope of the dimming. Either decrease in Betelgeuse's effective temperature to 3450 K, or a significant surface activity through starspots.

Dupree et al. (2020) managed to find a connecting link between most of the previous data. Based on the UV observations acquired by HST, they identified a hot structure that had formed in Betelgeuse's southern hemisphere during the beginning of the Dimming. Due to a combination of two major effects, the expansion of photosphere as part of the pulsation period and convective outflows, the apparent mass loss event resulted from an unprecedented powerful outflow. As the material cooled down, the dust opacity could increase quickly enough, which would explain the dimming of Betelgeuse's southern hemisphere.

The irregularities in Betelgeuse's variability continued, as after its initial rapid rise in brightness that restored Betelgeuse's usual values of brightness, it reached several new minima of brightness, all in shorter time intervals than the previously dominant ~ 400 days period (AAVSO, Dupree et al., 2022). A detailed investigation by Montargés et al. (2021) also supports the mass loss event scenario, although it does not fully rule out the possibility of a decrease in surface temperature. Nonetheless, Harper et al. (2008b) showed that the Dimming could be explained by a decrease of temperature by about ~ 200 K, while no additional dust was required.

However, the epoch of Great Dimming and its connection to previous light variability is still not well understood. To better understand the epoch of Great Dimming and the variability of the star in general, we provide here a detailed analysis of photometric and spectroscopic variability covering the last 30 years, i.e., 1990–2021.

2. Spectral analysis

We analysed numerous high-quality calibrated ultraviolet and optical spectra from many publicly available sources using Starlink SPLAT-VO (Škoda et al., 2014). All the spectra and their sources are listed in Table 1. The ultraviolet spectra were acquired by STIS and GHRS spectrographs onboard Hubble Space Telescope (hereafter HST). The optical spectra were acquired by several different spectrographs (see Table 1). In total, about 120 spectral lines were used to determine the radial velocities.

The optical spectra usually include a wide range of wavelengths, therefore it was possible to use one set of spectral lines in SPLAT-VO to identify the lines in all the spectra. On the other hand, the ultraviolet spectra were often captured in relatively narrow wavelength windows, therefore it was often not possible to use the same list of spectral lines. Moreover, STIS data are not publicly available in a simple linear format, i.e., a dependency of flux on wavelength. Therefore, in order to analyse the spectra in SPLAT-VO, the orders had to be merged. Nonetheless, the spectra that are part of ASTRAL library (Ayres, 2014) are already converted and publicly available.

HST spectra were captured at different positions relatively to the centre of Betelgeuse (Dupree et al., 2020), usually scanning from one edge of Betelgeuse to the other edge through its centre. The aperture sizes (given in Table 4) are smaller than the diameter of Betelgeuse, therefore the position (and size) of the aperture used in each subexposure must be taken into account, as it will affect the results. This does not apply to the optical spectra that we used, because their apertures are larger than the diameter of the star.

Most STIS datasets include 7 subexposures (010-070), some up to 9. In the newer datasets the subexposure 040 corresponds to the centre of the star, but in the older datasets other subexposure (or more than one) correspond to the centre (the names of datasets and subexposures are also given in Table 4). Nonetheless, for the determination of radial velocities we checked the positions of apertures in each dataset to confirm that we used the ones corresponding to the centre of the star. For the analysis of rotational velocity (only for the newer data), we also used subexposures from the ultraviolet surface, usually the edges (010 and 070). The results from these subexposures are given in Table 5.

Numerous spectra from HST were omitted based on quality comment of the data, such as due to issues with acquisition of a guide star (the omitted spectra are listed in Table 4).

Table 2
List of photometric data used for the light curve analysis.

Reference	Wavelength region [Å]	MJD [d]	Source
AAVSO [E9]	3000-19370	48500-59800	[E9]
BRITE (Pigulski et al., 2018)	3900-4600 & 5500-7000	56500-59250	[E10]
SMEI (Jackson et al., 2004)	4500-11000	52500-55800	[E11]

Table 3
Spectral lines used for the radial velocity analysis. The line lists were created based on Carpenter et al. (2018), Brandt et al. (1995) and [E13]. The exact wavelengths of all the lines were taken from NIST [E14] and are given in Å. Ultraviolet wavelengths are given in vacuum, while the optical ones are given in air.

Chromosphere and stellar wind				Ultraviolet photospheric region		Optical region			
Line	Wavelength	Line	Wavelength	Line	Wavelength	Line	Wavelength	Line	Wavelength
Fe II	2280.81	Fe II	2600.30	Fe II	2905.22	Ca II	3933.66	Ti II	4501.27
Fe II	2328.27	Mn II	2606.61	Fe I	2913.01	Ca II	3968.47	Ti I	4512.73
Fe II	2332.15	Fe II	2608.05	Fe I	2929.86	Ti I	4024.57	Ti I	4522.80
Fe II	2333.66	Fe II	2612.04	Fe I	2937.76	Mn I	4030.76	Fe I	4920.50
Fe II	2355.77	Fe II	2614.72	Fe I	2974.10	Mn I	4033.07	Ba II	4934.08
Fe II	2369.48	Fe II	2618.58	Fe I	2982.31	Mn I	4034.49	Fe I	5079.74
Fe II	2371.39	Fe II	2621.37	Fe I	2995.30	Fe I	4045.81	Mg I	5167.32
Fe II	2374.58	Fe II	2622.63	Fe I	3008.16	Fe I	4063.59	Mg I	5183.60
Fe II	2376.12	Fe II	2626.62	Fe I	3009.01	Fe I	4071.74	Fe I	5371.49
Fe II	2380.20	Fe II	2629.25	Fe I	3014.37	Sr II	4077.71	Fe I	5405.77
Fe II	2385.27	Fe II	2715.36	Fe I	3018.51	Fe I	4132.06	Fe I	5429.70
Fe II	2385.86	Fe II	2725.93	Fe I	3024.91	Fe I	4134.42	Ni I	5476.91
Fe II	2392.41	Fe II	2728.52	Fe I	3026.72	Fe I	4143.87	Na I	5889.95
Fe II	2400.10	Fe II	2731.75	Fe I	3048.49	Fe I	4181.75	Na I	5895.92
Fe II	2403.49	Fe II	2733.47	Ni I	3051.71	Fe I	4187.04	Fe I	6400.32
Fe II	2450.62	Fe II	2737.97	Fe I	3059.98	V I	4190.73	Ti I	6413.10
Fe II	2451.99	Fe II	2740.53	Ti II	3067.11	V I	4191.52	Fe I	6421.35
Fe II	2485.10	Fe II	2744.19			Fe I	4199.10	Fe I	6430.85
Fe II	2494.18	Fe II	2747.44			Ca I	4226.73	Ca I	6455.60
Fe II	2506.15	Fe II	2747.91			V I	4234.00	Ca I	6462.57
Fe II	2563.46	Fe II	2756.76			Cr I	4254.35	Fe I	6469.12
Fe II	2564.37	Fe II	2760.37			V I	4259.31	Ca I	6471.66
Fe II	2567.83	Fe II	2762.86			Fe I	4271.76		
Fe II	2578.85	Fe II	2769.95			Cr I	4274.81		
Fe II	2583.49	Mg II	2796.48			Cr I	4289.73		
Fe II	2586.80	Mg II	2803.67			Fe I	4383.55		
Fe II	2592.50	Mg I	2853.15			Fe I	4466.55		
Mn II	2594.67	Fe II	2881.81			Fe I	4482.17		
Fe II	2599.32					Fe I	4489.74		

STELLA data

Because the (optical) spectra available to us contain large time gaps, we also adapted high-quality determinations of radial velocities by STELLA robotic spectrograph (Granzer et al., 2021) to improve the results, as they aggregated considerably more data. This dataset consists of unprecedentedly enormous amount of the radical velocity determinations in optical region, about 2000 spectra across 14 years (covering MJD = 54754−59716). The instrument and data reduction are described in Strassmeier et al. (2004), Weber et al. (2012). STELLA data are used in Chapter 4.

2.1. Radial velocity

Spectral lines used for the radial velocity analysis were selected primarily based on Carpenter et al. (2018), Brandt et al. (1995) and [E13]. For determination of radial velocity, we used only such lines that could be easily identified even in spectra of lower quality. The spectral lines that we used are given in Table 3. To determine radial velocity, we primarily used selected absorption lines and centrally reversed emission lines (in UV). Afterwards, the lines were fitted with SPLAT-VO, using Voigt profile.

As the ultraviolet spectra consist of various types of spectral lines, we divided ultraviolet spectral lines into two groups (Brandt et al., 1995; Carpenter et al., 2018) that were analysed separately. The first group is composed of lines that are supposed to originate in the warm chromosphere or at the base of outflowing wind as given in paper by Carpenter et al. (2018). The lines in this list span from far ultraviolet to 2881 Å. As the majority of ultraviolet spectra in our sample start at about 2300 Å, we did not use all the lines. Some weaker lines were also not used. Almost all the lines in this list correspond to single ionized metals and a large portion of them also have emission wings (centrally reversed emission). To determine radial velocity, we analysed the central absorption feature, therefore these results correspond to velocity of stellar wind (Wood et al., 2004, 2016), and thus we will refer to them as such. Analysis of other absorption features in this region gave similar results of radial velocity, but in further analysis we used only the lines from Carpenter et al. (2018).

The second group of lines in the ultraviolet spectra are from a wavelength region above 2900 Å, where the photospheric absorption starts to dominate the spectrum and photospheric continuum becomes prominent (although some chromospheric features remain significant) (Brandt et al., 1995; Carpenter et al., 2018). Spectral lines in this group consist primarily of absorption by neutral metals. The radial velocity determined from this group should correspond to outer atmosphere (Brandt et al., 1995). We shall refer to this group of lines as ultraviolet photospheric region.

To test the validity of this approach, we also divided the lines into groups based on their excitation potential (in the UV and optical region) and fitted them separately, but the differences between determined radial velocities did not exceed the margin of error. For the stellar wind lines we also compared the absorption cores velocities to velocities of the emission wings centroids, but it gave similar results. Lastly, we determined radial velocity from pure emission features (without central reversals). These determined velocities were higher than the ones from stellar wind lines, usually centred at rest with respect to the photosphere, which is in agreement with Carpenter et al. (1995).

Table 4
Determined radial velocity v_r from all the spectra, used in the upper panel of Fig. 1. All the UV radial velocities in the table were determined from the central subexposures. Omitted UV spectra — OEDQ04, OEDQ03 (subexposures 10-40), OEDQ02, OE1I02, ODXG01 (subexposure 10), ODXG04, ODXG03, ODXG05, OBKK71, O6LX03, O6LX02, as well as ZOYL01 (GHRS) and OBKK74 due to much larger apertures ($0.2 \times 0.2''$).

Ultraviolet spectra					
Source	MJD [d]	Dataset/Subexposure	$v_{r,wind}$ [km s^{-1}]	$v_{r,photo}$ [km s^{-1}]	Aperture [″]
HST ASTRAL	50821.45	O4DE03050	17.88 ± 0.48	20.92 ± 0.69	0.1 × 0.03
HST ASTRAL	50904.67	O4DE05050	20.36 ± 0.47	20.69 ± 0.73	0.1 × 0.03
HST ASTRAL	51077.18	O4DE07050	21.06 ± 0.49	19.90 ± 0.75	0.1 × 0.03
HST ASTRAL	51265.31	O4DE09050	18.73 ± 0.39	21.94 ± 0.69	0.1 × 0.03
HST ASTRAL	52562.57	O6LX01020	19.27 ± 0.45	20.05 ± 0.94	0.2 × 0.06
HST ASTRAL[a]	55600.34	OBKK72010/72020	21.85 ± 0.47		0.2 × 0.09
HST ASTRAL[a]	55615.85	OBKK73010/74020	21.84 ± 0.44		0.2 × 0.09
HST ASTRAL	55652.38	OBKK76020	21.45 ± 0.52		0.2 × 0.09
HST STIS	58508.31	ODXG01040	19.33 ± 0.44	21.64 ± 0.99	0.1 × 0.03
HST STIS	58547.57	ODXG02040	18.68 ± 0.39	20.01 ± 0.78	0.1 × 0.03
HST STIS	58744.33	ODXG07040	17.67 ± 0.40	19.10 ± 1.10	0.1 × 0.03
HST STIS	58762.81	ODXG08040	16.85 ± 0.38	18.96 ± 1.24	0.1 × 0.03
HST STIS	58815.64	OE1I01040	18.21 ± 0.44	20.20 ± 1.12	0.1 × 0.03
HST STIS	58882.38	OE1I52040	15.75 ± 0.37	16.67 ± 0.83	0.1 × 0.03
HST STIS	58904.82	OE1I03040	15.82 ± 0.34	17.74 ± 0.72	0.1 × 0.03
HST STIS	58941.04	OE1I04040	14.50 ± 0.37	19.38 ± 0.75	0.1 × 0.03
HST STIS	59092.77	OEDQ01040	16.03 ± 0.36	19.91 ± 0.65	0.1 × 0.03
HST STIS	59177.04	OEDQ52040	16.46 ± 0.35	20.98 ± 0.84	0.1 × 0.03
HST STIS	59475.69	OEDQ54040	19.13 ± 0.49	24.35 ± 1.18	0.1 × 0.03

Optical spectra			
Source	MJD [d]	$v_{r,OPT}$ [km s^{-1}]	Aperture [″]
F/H	49868.96	19.58 ± 0.87	2.7
F/H	50455.68	18.37 ± 0.50	2.7
ELODIE	51204.90	22.50 ± 0.49	2
UVES	52530.42	21.54 ± 0.52	0.5
ELODIE	52873.14	22.82 ± 0.45	2
ELODIE	52899.16	22.56 ± 0.46	2
ELODIE	52953.09	20.42 ± 0.50	2
ELODIE	53048.90	19.33 ± 0.47	2
ELODIE	53121.81	20.56 ± 0.42	2
ELODIE	53244.16	22.75 ± 0.43	2
ELODIE	53404.90	18.84 ± 0.42	2
SOPHIE	54074.01	22.17 ± 0.49	3
X-shooter	55116.34	25.97 ± 0.67	0.5
UVES	56570.38	20.18 ± 0.42	0.4
HARPS	58891.07	19.83 ± 0.51	1

[a]In these datasets the wavelength regions were split into 2378-2650 and 2621-2887, therefore results from these two regions were merged (when available). In the case of OBKK73010/74020 there was a 2 day gap between the observations. However considering the length of periods, this should not affect the results. The date of the latter observation is 55617.96.

Table 5
Determined UV photospheric radial velocities across the disk of the Betelgeuse, used in the bottom panel of Fig. 1. MJD of datasets correspond to the previous table. Position angle of the axis of rotation as determined by Kervella et al. (2018) is 48° (all angles are given in ° E of N). Position angles of the aperture given for each dataset. Subexposures correspond to different positions the ultraviolet surface of Betelgeuse, as discussed in Chapter 2. Some datasets also have 080 subexposures at distance of 100 mas from the centre.

Ultraviolet photospheric region								
Dataset	Position angle [°]	$v_{r,photo}$ [km s^{-1}]						
		Subexposure						
		010	020	030	050	060	070	080
ODXG01	35.1		18.63 ± 1.10	18.74 ± 1.05	19.21 ± 1.00	18.90 ± 0.99	20.06 ± 0.96	
ODXG02	40.5	22.13 ± 0.78					18.78 ± 1.01	
ODXG06[a]	52.5	19.40 ± 0.59						
ODXG07	−136.6	19.14 ± 0.95					19.13 ± 1.05	
ODXG08	−131.5	17.32 ± 0.86					17.94 ± 1.11	
OE1I01	−102.4	18.50 ± 0.93	18.23 ± 1.09	17.88 ± 1.05	17.64 ± 1.08	17.57 ± 1.36	18.61 ± 1.10	17.56 ± 1.27
OE1I52	35.2	16.45 ± 0.87					18.16 ± 0.81	
OE1I03	38.0	17.35 ± 0.72					18.68 ± 0.91	
OE1I04	50.5	18.57 ± 0.92					17.89 ± 0.66	
OEDQ01	−141.4	19.56 ± 0.87	18.13 ± 0.95	17.75 ± 0.91	18.61 ± 1.02	18.34 ± 1.11	19.07 ± 0.77	18.17 ± 1.02
OEDQ52	−106.9	19.60 ± 0.84					20.13 ± 0.85	
OEDQ03[a]	32.2						21.97 ± 0.82	

[a]Unused in bottom panel of Fig. 1 due to a missing subexposure from the centre of the star.

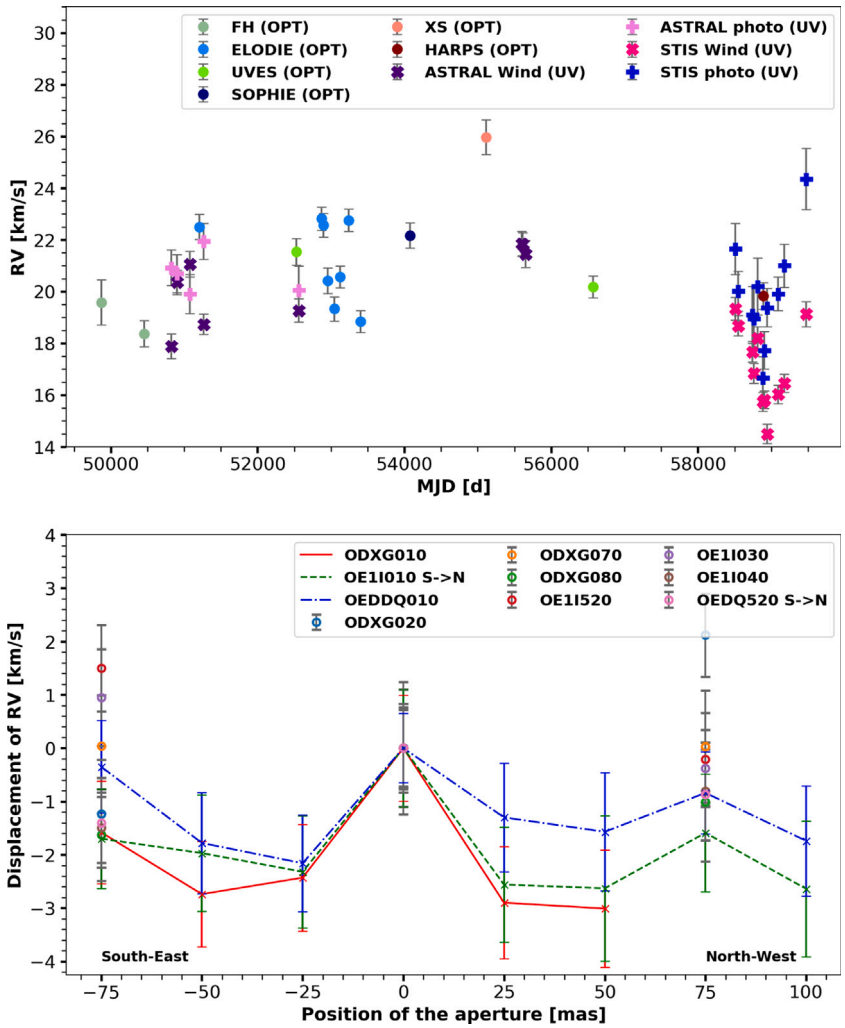

Fig. 1. *Upper panel:* Dependence of radial velocity v_r on MJD, using results from all the spectra that were analysed in this paper (Table 4). *Bottom panel:* Radial velocity from the ultraviolet photospheric region measured across the disk of Betelgeuse from the datasets **ODXG**, **OE1I** and **OEDQ**, as given in Table 5. The position is relative to the disk centre and position angles of scans were not the same each time. Position angles of the datasets labelled as S->N were orientated about $\sim 30°$ from the position angle of the axis of rotation, therefore the observed rotational effects should be minimal. The zero value on y coordinate corresponds to the central subexposure (Table 4).

However, we were able to analyse only a few of such emission lines therefore we will not use them in the following analysis.

The determined radial velocities are listed in Table 4 and are plotted together in Fig. 1. The HST STIS datasets **ODXG**, **OE1I** and **OEDQ** are the ones near the Great Dimming. We also used them to analyse rotational velocity by using the subexposures across the surface of the star. The individual radial velocities for each of the subexposures are listed in Table 5. In ASTRAL **O4DE** dataset, i.e., the one between MJD 50821-51265, we only used subexposures 050 as they correspond to the centre of the star. On the other hand, subexposures in the ASTRAL dataset **OBKK** use different wavelength regions rather than positions on the surface, as well as slightly larger apertures. Most of the spectra within this dataset that we used are within the wavelength region under 2900 Å, but do not cover the photospheric region.

In further analysis, some UV spectra were omitted due to significantly larger apertures compared to other UV spectra, such as spectra from GHRS and OBKK74010, as the different aperture size might affect the resulting radial velocity (and it indeed appears to be the case). **O6LX** and **OBKK** datasets also have larger apertures, but less than the omitted spectra, and it appears the determined radial velocities from this dataset are of similar values as most of other datasets that we used, although they appear slightly larger.

The data plotted in Fig. 1 have some considerable gaps, but fortunately they seem to cover the full range of possible radial velocities v_r values, i.e., the minima and maxima. At several places, the results also display a variability at smaller time scales, such as the ones from ELODIE, and especially the ones from STIS.

The radial curve shows a major systematic difference between the velocities determined from the optical and ultraviolet spectra. While the optical radial velocities v_r have a range between about 19–28 $\mathrm{km\,s^{-1}}$, the velocities of stellar wind have a range of only 14–22 $\mathrm{km\,s^{-1}}$. The variability itself appears to be happening on a different time scale as well. For example a closer examination of the well covered ultraviolet peak (in both ultraviolet line lists) of ASTRAL **O4DE** dataset (the values with MJD between 50821-51266) shows a relatively slow variability near the local radial velocity maximum, covering roughly 370 days, while the profile of the peak suggests that the period is much longer. On the other hand, on a similar timescale radial velocities from ELODIE appears to undergo one full period of variability. Similarly, examining the **ODXG**, **OE1I** and **OEDQ** ultraviolet radial velocities near the Great Dimming, covering about 820 days, yields a slow fall into a minimum, culminating by the time of the Great Dimming, and a subsequent slow rise. Therefore, the data suggest that radial velocity in ultraviolet is undergoing a variability on a much longer time scale than radial velocity in the optical part of the spectrum, and on top of that the amplitude is not the same. The ultraviolet photospheric radial velocity is more similar to the optical radial velocity, at least in terms of amplitude. Considering the

event that is covered by **O4DE** dataset, when the radial velocities from the two ultraviolet regions intertwined, it shows that both groups of ultraviolet lines that we selected are indeed fundamentally different and have different periods of variability.

In optical region, the changes of the radial velocity we observe are largely due to the pulsations of Betelgeuse. Henceforth, the variability is due to some layers of Betelgeuse's atmosphere changing its relative velocity towards us. As the majority of contributions to the spectra are from the photosphere, it would be more relevant to use term photospheric velocity to describe the velocity variability.

2.2. Rotational velocity

As discussed previously, the STIS spectra are taken from different parts of Betelgeuse surface including the centre and edges. Thus, it could be possible to unveil rotational effects by comparing the spectra from different parts of Betelgeuse surface as one side of Betelgeuse should be moving towards us, while the other side away from us. Table 5 lists ultraviolet photospheric radial velocities determined from different parts of the stellar surface, which are plotted in the bottom panel of Fig. 1.

While the resulting plots (bottom panel of Fig. 1) show a systematic trend, it does not reveal the projected rotational velocity $v_{\rm rot}\sin(i)$, as both edges of Betelgeuse seem to be moving towards us mostly at a similar velocity. According to Kervella et al. (2018), the value of projected rotational velocity is $v_{\rm rot}\sin(i) = 5.47 \pm 0.25\,{\rm km\,s^{-1}}$, therefore the effects should have been theoretically observable. But based on the data, it is questionable whether rotational effects are observable in this region of UV. That notion is reinforced by the fact that ultraviolet diameter of Betelgeuse is much larger than the optical diameter (Dupree et al., 2020), therefore distances of most subexposures are further from the centre than the diameter of photosphere.

3. Photometry

For photometric analysis, the data from AAVSO, BRITE and SMEI were used (Table 2).

3.1. Light curve

Combining the data gives us almost a continuous brightness variability of Betelgeuse for the last two decades, with SMEI covering the first decade, and AAVSO supplementing sufficiently enough the rest. The combined plot can be seen in Fig. 2.

As can be seen in Fig. 2, the observations in filters using longer wavelengths (I, J, H) are considerably less affected by the variability of the star (Gehrz et al., 2020). As the star is the brightest in near-infrared region, this means that the variability we observe (most often in optical region) does not affect the overall brightness of the star in such a dramatic way. That can be seen in even greater extent during the Great Dimming as well, which suggests several possible causes of the Dimming. For the determination of period, SMEI is the best source, as it has a continuous high-quality coverage of almost two periods. The V filter from AAVSO is also very promising, but it has large time gaps. The time gaps are caused by the position of the star, as during summer period in the northern hemisphere it is difficult to observe Betelgeuse by ground-based observations.

SMEI data

The Solar Mass Ejection Imager (SMEI, Eyles et al., 2003) was launched into an Earth-terminator, Sun-synchronous, 840 km polar orbit as a secondary payload on board the Coriolis spacecraft in January 2003 and was terminated in September 2011. Its main purpose was to monitor and predict space weather in the inner solar system. SMEI comprised three wide-field cameras, which were aligned such that the total field of view is a 180 deg and about 3 deg wide arc, yielding a near-complete image of the sky after about every 101.5 min orbit.

A detailed description of the data analysis pipeline used to extract light curves from the raw data is provided by Hick et al. (2007). Because of the presence of strong instrumental trends, a basic cleaning algorithm as described in Paunzen et al. (2021) was applied.

4. Period analysis

The following periods were determined using CLEANest method in the PERANSO program (Paunzen and Vanmunster, 2016). It features several methods to deal specifically with irregularly spaced data and multi-period signals (it was also used to clean the BRITE and SMEI data by removing outliers). As we can see in Figs. 3 and 4, the variability has fundamentally changed during the Dimming, therefore in the following analysis the period is determined separately before and after the Great Dimming.

4.1. Photometric variability

Photometric period analysis was performed using the SMEI and AAVSO V data in PERANSO, after outliers were removed (for SMEI). The dominant periods (before the Dimming) are $P_1 = 2190 \pm 270$ d and $P_2 = 417 \pm 17$ d, $P_3 = 365 \pm 75$ d and $P_4 = 185 \pm 4$ d. The third strongest period P_3 shares the peak with P_2. These results correspond well to the values given by Kiss et al. (2006) and Chatys et al. (2019), except P_4, which might correspond to observational gaps in summer. The longer period is often given with a similarly large uncertainty, such as in the literature cited above. After the Dimming, the dominant mean period is 230 ± 29 d.

4.2. Radial velocity variability

As was discussed in Section 2.1, radial velocity from different parts of Betelgeuse's spectrum, i.e., ultraviolet and optical, should be examined separately.

The dominant periods of optical region (before the Dimming) are $P_{1,v_{\rm r}} = 2510 \pm 440$ d, $P_{2,v_{\rm r}} = 415 \pm 11$ d, $P_{3,v_{\rm r}} = 185 \pm 4$ d and $P_{4,v_{\rm r}} = 370 \pm 9$ d. To improve the results, we also used the data from STELLA robotic spectrograph (Granzer et al., 2021).[1] The second and fourth results correspond well to the shorter period given by Kiss et al. (2006) and Chatys et al. (2019), as well as to photometric periods P_2 and P_3 determined here (they share the same peak as well). The period $P_{1,v_{\rm r}}$ shows a clear connection to the longer period. After the Dimming the dominant mean period is 200 ± 18 d, which is perhaps connected to the period $P_{3,v_{\rm r}}$ that was present before the Dimming and is the same (within margin of error) as the post Dimming period determined from the photometry.

The dominant periods determined from the velocity of stellar wind are: 1432 ± 76 d, 2410 ± 470 d, and 757 ± 16 d. The second period suggests a connection to the longer period. The other two peaks are relatively strong and suggest different new periods. Nonetheless, there are no significant peaks similar to the shorter period, therefore there does not seem to be a connection of a chromosphere or stellar wind to the shorter period.

For the ultraviolet photospheric region the determined periods are: 560 ± 12 d, 1190 ± 50 d, and 653 ± 17 d. The first period is to a degree close to the periods determined from optical radial velocities $P_{2,v_{\rm r}}$ and $P_{4,v_{\rm r}}$, which suggests that in this wavelength region the photosphere does indeed become prominent. The other periods are somewhat similar to the shorter periods of stellar wind velocities, although there are numerous narrow peaks.

[1] Even without using the additional data from STELLA it was possible to detect the shorter period by Kiss et al. (2006) and Chatys et al. (2019).

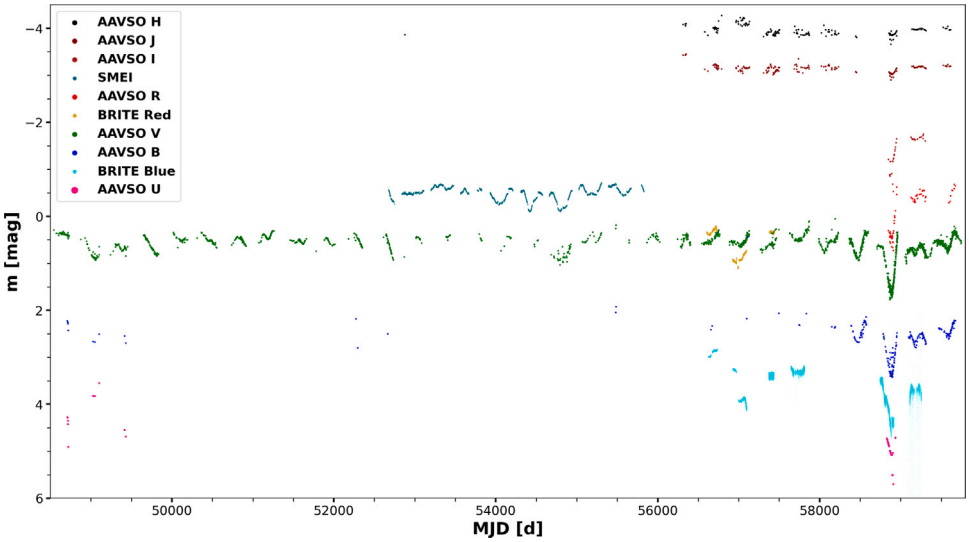

Fig. 2. Light curve comprising of all the photometric data adopted here, from H (upper curve) to U (bottom curve), i.e., in the same order as in the legend. The data cover the last three decades and end shortly after the Great Dimming. The data from V filter range even farther into history, but they were not plotted to improve scaling.

Therefore, it appears that the variations of ultraviolet radial velocities are not caused by the pulsations, or at the very least not by the same processes that drive the variability of radial velocity in the optical region. Instead, the radial velocity determined from the ultraviolet photospheric region is likely a subject to other processes in outer parts of the Betelgeuse's atmosphere, possibly loosely connected to the processes that lead to the longer period, while the main group of the ultraviolet lines represent the stellar wind (as discussed previously). Furthermore, Kervella et al. (2018) showed that the angular velocity changes as a function of radius, so the results are likely affected by that as well.

4.3. Connection of radial velocity and light variations

The radial velocity and major photometric data were plotted together in Figs. 3 and 4, so that the curves can be directly compared. Out of the optical radial velocities analysed here, only 3 were taken during the same period as STELLA. Considering that different methods were used, our results correspond reasonably well to the adapted values adopted from literature, although the velocity determined from X-shooter seems to be too high. The variability of amplitudes of both curves is clearly correlated, i.e., when the amplitude of magnitude is smaller, the amplitude of radial velocity is usually also smaller and it is apparent that both curves follow similar periods of variability.

Furthermore, the maxima of optical radial velocity seem to be usually delayed by roughly one month after the brightness minima. As we can see in Fig. 4, during the Great Dimming the velocity of stellar wind reached a maximum. The ultraviolet radial velocity from the photospheric region is indeed more similar to the optical radial velocity, sometimes it appears to follow the optical light curve very closely, such as during the beginning of the Great Dimming. Nevertheless, during other parts of the Great Dimming it is clearly not following the optical radial curve anymore.

5. Discussion and conclusions

In this research we aimed to study Betelgeuse's variability in pursuit of explaining its causes, and possibly to bring some context to the unprecedented Great Dimming. To accomplish that, we accessed many available public archival data, coming from various high-quality instruments. The results show that variability of optical and ultraviolet radial velocities are distinctively different from each other, as well as the brightness variability in various filters. These results and their comparison allow us to study the variability in a greater extent.

The optical radial velocity variability corresponds very well to both periods given by Kiss et al. (2006) and Chatys et al. (2019). The changes of radial velocity are likely caused by the pulsations of the photosphere, thus we interpret the radial velocity from optical region as a photospheric velocity of Betelgeuse. The longer mode of variability is also prominent in the optical radial velocity, therefore it appears that convection strongly influences the radial velocity as well, as the longer period is often attributed to convection cells (Stothers, 2010).

In the ultraviolet spectra we analysed two groups of spectral lines separately, stellar wind lines and lines from a region where the influence of the photosphere rises (Carpenter et al., 2018). Despite the fact that most of the spectra studied here were obtained in the ultraviolet region, the data was usually restricted to relatively short periods of time, thus proving it difficult to correctly determine the overall period.

The systematic difference between the values of optical radial velocity and the stellar wind lines is primarily caused by the expansion of stellar wind. As the stellar wind accelerates material towards us, the radial velocity determined in upper parts of atmosphere is therefore lower, relative to Betelgeuse's rest velocity. Our results for the velocity of stellar wind are similar to the ones reported by Carpenter et al. (1995, 2018), who report velocity outflows of several $\mathrm{km\,s^{-1}}$, increasing with optical depth of a given line. However, in their studies they analysed shorter periods of time. As we analysed larger sample of data, we show that the velocity of stellar wind is highly variable as well, at some times it is close to the star's rest velocity. The variability of stellar wind is likely affected by a multitude of processes in outer parts of atmosphere. It likely corresponds to various episodic gaseous outflows (Humphreys and Jones, 2022), local (up/down)flows and global nonradial chromospheric oscillations that might partially be in phase with photospheric pulsations (Lobel and Dupree, 2001). Nonetheless, the time scale of the variability is different than for the photospheric radial velocity. We analysed periodicity of stellar wind and found that periods 1432 ± 76 d and 2410 ± 470 d are the most prominent, while the second one is similar to the longer period derived by Kiss et al. (2006) and Chatys et al. (2019).

The ultraviolet photospheric region did not yield a reasonably accurate period, although the periods and amplitudes are considerably closer to the periods of photospheric radial velocity. To a certain degree, the radial velocity appears to be affected by the overall magnitude variability and pulsation cycle. The possible explanations for the processes that drive the variability of these groups of lines are less

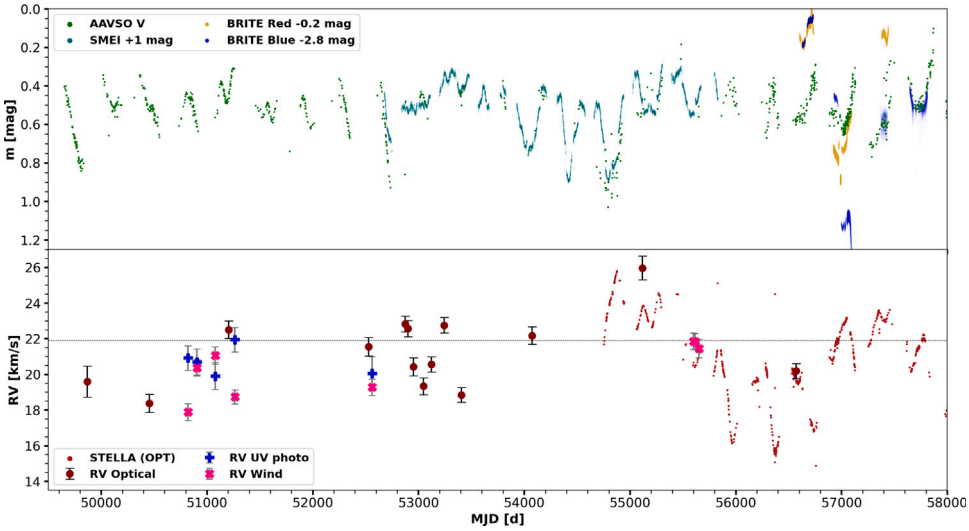

Fig. 3. Joint plot of radial velocities and photometric data covering the last 30 years, except the Great Dimming. The plot of photometric data (*upper panel*) contains only data in selected filters due to scaling issues. The plot of radial velocities (*lower panel*) includes the data from Granzer et al. (2021). RV Optical refers to the optical spectra that were analysed in this paper. The broken dashed line corresponds to Betelgeuse's rest velocity 21.9 km s^{-1} (Famaey et al., 2005). The plot is continued in Fig. 4.

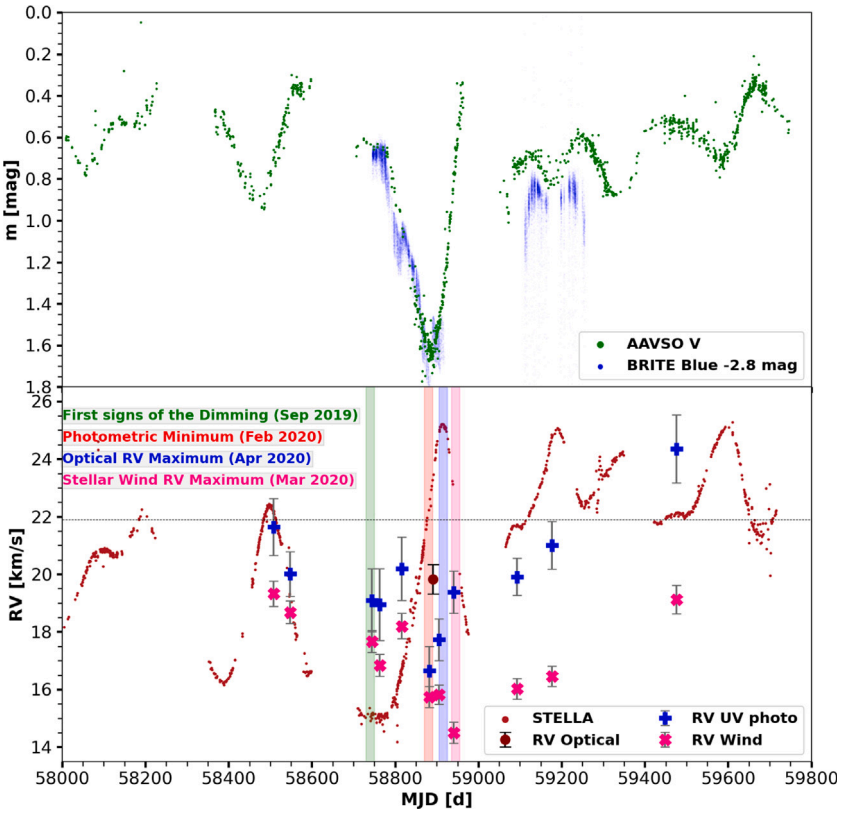

Fig. 4. Detailed plot of magnitude variations (*upper plot*) and radial velocity (*lower plot*) during the period of the Great Dimming and after the Dimming. Plotted using additional data by Granzer et al. (2021) and marking the significant points in time.

obvious. Partially, it can be affected by the same multitude processes as discussed in the previous paragraph. Possibly, it could also correspond to velocity of stellar wind, but closer to the photosphere, where the speed of stellar wind is lower. Besides that, this region is undoubtedly affected by the photosphere significantly, as at some occasions its radial velocity is following the optical radial curve and is of similar values. However, the results of velocity based on the ultraviolet spectra are not as abundant and precise as the measurements from STELLA, therefore the interpretation of these results remains rather ambiguous.

As part of studying the ultraviolet spectra, we also attempted to measure projected rotational velocity $v_{\rm rot}\sin(i)$ of Betelgeuse, by studying additional spectra from the disk of the star, and comparing them to central spectra. We used the results from the ultraviolet photospheric region, where the photosphere is already prominent. But this analysis

did not provide reasonable results. Apart from other reasons already discussed, the reason that the method did not succeed might be largely due to the fact that the parts of Betelgeuse's atmosphere where ultraviolet spectral lines that we used are formed simply do not fully reflect the rotation of photosphere. However, Kervella et al. (2018) suggests a period of rotation 31 ± 8 years and a rotational coupling of Betelgeuse and its chromosphere, therefore if a more elaborate method would have been used, it would have likely been possible to determine $v_{\rm rot}\sin(i)$. Rather than measuring rotational effects, our results of radial velocity across the Betelgeuse's disk probably corresponds to the local upflows and downflows with amplitudes up to $\sim 2\,{\rm km\,s^{-1}}$ reported by Lobel and Dupree (2001). This suggests why the results of ultraviolet radial velocity in this study did not provide expected results of $v_{\rm rot}\sin(i)$.

As part of photometric analysis, it was possible to reliably determine the periods $P_1 = 2190 \pm 270$ d and $P_2 = 417 \pm 17$ d, which is in high accordance with the most dominant periods determined by optical photospheric velocities. These photometric periods are also in accordance with the values by Kiss et al. (2006) and Chatys et al. (2019). The photometric data do not support that the Great Dimming is due to a simple convergence of the shorter and longer period, as the amplitudes of the two main periods could not cause such a decrease in brightness even when combined. Fortunately, the AAVSO photometric data from various filters (Fig. 2) give a major information about what could have possibly caused the Dimming. Based on the filters from near-infrared region, where Betelgeuse is the brightest, the Dimming is on a much smaller magnitude scale (filter I) than in optical filters, or barely noticeable at all (filters J and H) (Gehrz et al., 2020). Therefore, this possibly means that Betelgeuse was actually not physically affected by the Great Dimming, i.e., that the star did not change its luminosity, but that there was an extinction, mostly in optical region. That could have been due to dust particles in a proximity of the star, therefore Betelgeuse must have experienced a significant loss of mass prior to the Dimming. The reason could also be that Betelgeuse's effective temperature $T_{\rm eff}$ decreased. That would cause the peak of Betelgeuse's brightness to move to longer wavelengths, henceforth the Dimming would be of a smaller scale in the infrared. So Betelgeuse could have decreased either its entire surface's effective temperature, or only some parts of the surface did. Betelgeuse is known to have large convective cells and starspots (Kervella et al., 2018), so possibly the overall surface temperature could have temporarily decreased due to an unprecedented activity of this kind.

Most importantly, the spectral analysis reveals the global minimum of ultraviolet radial velocity (in both UV groups) during the Great Dimming, therefore the velocity of stellar wind had its maximum in March 2020. Either way, this supports that during the Great Dimming there was a massive outflow of material, most likely connected to the mass loss event in southern hemisphere of Betelgeuse that was reported by Dupree et al. (2020), Kravchenko et al. (2021), Montargés et al. (2021) and regarded to be responsible for the Great Dimming. It was followed by the minimum of brightness in February 2020 (Guinan et al., 2020) and later by a maximum of optical radial velocity in April 2020, as reported by Granzer et al. (2021). Furthermore, in Fig. 4 we can also see that after the Great Dimming Betelgeuse did not return to its original mode of variability, but it is now instead following a much shorter period of ~ 200 d. These findings give us new insights regarding the Great Dimming, the connection between Betelgeuse's photosphere and chromosphere and the nature of stellar wind in red supergiants that should be examined further.

CRediT authorship contribution statement

Daniel Jadlovský: Conceptualization, Methodology, Data curation, Software, Formal analysis, Investigation, Writing. **Jiří Krtička:** Supervision, Conceptualization, Methodology, Validation, Investigation, Resources. **Ernst Paunzen:** Data curation, Software. **Vladimír Štefl:** Investigation, Resources.

Declaration of competing interest

The authors declare the following financial interests/personal relationships which may be considered as potential competing interests: Daniel Jadlovský reports writing assistance was provided by Masaryk University Faculty of Science.

Data availability

Links to public data were shared in the article, except for SMEI and STELLA, which are not publicly available.

Acknowledgements

Based on data collected by the BRITE Constellation satellite mission, designed, built, launched, operated and supported by the Austrian Research Promotion Agency (FFG), the University of Vienna, Austria, the Technical University of Graz, Austria, the University of Innsbruck, Austria, the Canadian Space Agency (CSA), the University of Toronto Institute for Aerospace Studies (UTIAS), Canada, the Foundation for Polish Science and Technology (FNiTP MNiSW), Poland, and National Science Centre (NCN), Poland. Based (partly) on data obtained with the STELLA robotic telescopes in Tenerife, an AIP facility jointly operated by AIP and IAC. The authors are grateful for the permission to use yet unpublished radial velocity data from STELLA (Granzer et al., 2021).

The authors would also like to express their gratitude to Dr. T. Ayres for his guidance with accessing the ASTRAL archive.

Other electronic sources

[E1] https://old.ipac.caltech.edu/2mass/releases/allsky/doc/
[E2] http://archive.eso.org/scienceportal/home
[E3] http://atlas.obs-hp.fr/sophie/
[E4] http://atlas.obs-hp.fr/elodie/
[E5] http://dc.zah.uni-heidelberg.de/flashheros/q/web
[E6] https://archive.stsci.edu/hst/atlasalfori/
[E7] https://archive.stsci.edu/prepds/astral/#catalog
[E8] https://archive.stsci.edu/hst/search.php
[E9] https://www.aavso.org
[E10] http://brite-wiki.astro.uni.wroc.pl/bwiki/doku.php?id=start
[E11] http://smei.ucsd.edu/
[E12] https://astro.physics.muni.cz/download/documents/bc/bpjadlovsky.pdf
[E13] http://spectra.freeshell.org/whyspectroweb.html
[E14] https://physics.nist.gov/PhysRefData/ASD/lines_form.html

References

Ayres, T.R., 2014. HST/STIS advanced spectral library (ASTRAL). In: International Workshop on Stellar Spectral Libraries ASI Conference Series, Vol. 11.
Baranne, A., Queloz, D., Mayor, M., et al., 1996. ELODIE: A spectrograph for accurate radial velocity measurements. Astron. Astrophys. Supplement 119.
Brandt, J.C., Heap, S.R., Beaver, E.A., et al., 1995. An Atlas of Alpha Orionis Obtained with the Goddard High Resolution Spectrograph on the Hubble Space Telescope. Astron. J. 109.
Carpenter, K.G., Nielsen, K.E., Kober, G.V., et al., 2018. The Advanced Spectral Library (ASTRAL): Reference Spectra for Evolved M Stars. Astrophys. J. 869 (2).
Carpenter, K.G., Robinson, R.D., Judge, P.G., 1995. GHRS observations of cool, low-gravity stars. II. Flow and turbulent velocities in the outer atmosphere of gamma crucis (M3.4 III). Astrophys. J. 444.
Chatys, F.W., Bedding, T.R., Murphy, S.J., et al., 2019. The period–luminosity relation of red supergiants with Gaia DR2. Mon. Not. R. Astron. Soc. 487 (4).
Dekker, H., D'Odorico, S., Kaufer, A., et al., 2000. Design, construction, and performance of UVES, the echelle spectrograph for the UT2 Kueyen Telescope at the ESO Paranal Observatory. In: Proc. SPIE, Optical and IR Telescope Instrumentation and Detectors, Vol. 4008.
Dharmawardena, T.E., Mairs, S., Scicluna, P., et al., 2020. Betelgeuse fainter in the submillimeter too: An analysis of JCMT and APEX monitoring during the recent optical minimum. Astrophys. J. Lett. 897 (1), id.L9.

Dupree, A.K., Strassmeier, K.G., Calderwood, T., et al., 2022. The Great Dimming of Betelgeuse: A Surface Mass Ejection and Its Consequences. Astrophys. J. 936 (1), id.18.
Dupree, A.K., Strassmeier, K.G., Matthews, L.D., et al., 2020. Spatially Resolved Ultraviolet Spectroscopy of the Great Dimming of Betelgeuse. Astrophys. J. 899 (1), id.68.
Eyles, C.J., Simnett, G.M., Cooke, M.P., et al., 2003. The Solar Mass Ejection Imager (Smei). Sol. Phys. 217 (2).
Famaey, B., Jorissen, A., Luri, X., et al., 2005. Local kinematics of K and M giants from CORAVEL/Hipparcos/Tycho-2 data. Astron. Astrophys. 430.
Gehrz, R.D., Marchetti, J., McMillan, S., et al., 2020. Betelgeuse remains steadfast in the infrared. Astronomer's Telegram (13518).
Granzer, T., Weber, M., Strassmeier, K.G., et al., 2021. The curious case of betelgeuse. CS20.5, https://zenodo.org/record/4561732#.YtfUxvlBy3A.
Guinan, E.F., Wasatonic, R.J., Calderwood, T.J., 2019. Updates on the fainting of betelgeuse. Astronomer's Telegram (13365).
Guinan, E.F., Wasatonic, R.J., Calderwood, T.J., 2020. The fall and rise in brightness of betelgeuse. Astronomer's Telegram (13512).
Harper, G.M., Brown, A., Guinan, E.F., 2008a. A new VLA-hipparcos distance to betelgeuse and its implications. Astron. J. 135 (4).
Harper, G.M., Guinan, E.F., Wasatonic, R., et al., 2008b. The Photospheric Temperatures of Betelgeuse during the Great Dimming of 2019/2020: No New Dust Required. Astrophys. J. 905 (1), id.34.
Hick, P., Buffington, A., Jackson, B.V., 2007. A procedure for fitting point sources in SMEI white-light full-sky maps, solar physics and space weather instrumentation II. Proc. SPIE 6689.
Humphreys, R.M., Jones, T.J., 2022. Episodic gaseous outflows and mass loss from red supergiants. Astron. J. 163 (3).
Jackson, B.V., Buffington, A., Hick, P.P., et al., 2004. The Solar Mass-Ejection Imager (SMEI) Mission. Sol. Phys. 225 (1).
Joyce, M., Leung, S., Molnár, L., et al., 2020. Standing on the shoulders of giants: New mass and distance estimates for betelgeuse through combined evolutionary, asteroseismic, and hydrodynamic simulations with MESA. Astrophys. J. 902 (1).
Kaufer, A., 1998. Variable circumstellar structure of luminous hot stars: the impact of spectroscopic long-term campaigns. In: Reviews in Modern Astronomy 11: Stars and Galaxies. Vol. 11.
Keenan, P.C., McNeil, R.C., 1989. The perkins catalog of revised MK types for the cooler stars. Astrophys. J. Supplement 71.
Kervella, P., Decin, L., Richards, A.M.S., et al., 2018. The close circumstellar environment of Betelgeuse, V. Rotation velocity and molecular envelope properties from ALMA. Astron. Astrophys. 609.
Kiss, L.L., Szabó, G.M., Bedding, T.R., 2006. Variability in red supergiant stars: pulsations, long secondary periods and convection noise. Mon. Not. R. Astron. Soc. 372 (4).
Kravchenko, K., Jorissen, A., Van Eck, S., et al., 2021. Atmosphere of Betelgeuse before and during the great dimming event revealed by tomography. Astron. Astrophys. manuscript no. 39801corr.
Levesque, E.M., Massey, P., 2020. Betelgeuse just is not that cool: Effective temperature alone cannot explain the recent dimming of betelgeuse. Astrophys. J. Lett. 891 (2), id.L37.
Lloyd, C., 2020. Betelgeuse – a century and more of variation. eprint arXiv:2006.15403.
Lobel, A., Dupree, A.K., 2001. Spatially resolved STIS spectroscopy of α orionis: Evidence for nonradial chromospheric oscillation from detailed modeling. Astrophys. J. 558 (2).
Mayor, M., Pepe, F., Queloz, D., et al., 2003. Setting New Standards with HARPS. The Messenger (114).
Montargés, M., Cannon, E., Lagadec, E., de Koter, A., 2021. A dusty veil shading betelgeuse during its great dimming. Nature 594 (7863).
Paunzen, E., Supíková, J., Bernhard, K., Hümmerich, S., Prišegen, M., 2021. Magnetic chemically peculiar stars investigated by the Solar Mass Ejection Imager. Mon. Not. R. Astron. Soc. 504 (3).
Paunzen, E., Vanmunster, T., 2016. Peranso - light curve and period analysis software. Astron. Nachr. 337 (3).
Perruchot, S., Kohler, D., Bouchy, F., et al., 2008. The SOPHIE spectrograph: design and technical key-points for high throughput and high stability, Ground-based and Airborne Instrumentation for Astronomy II.. Proc. SPIE 7014.
Pigulski, A., et al., 2018. BRITE Cookbook 2.0. Polish Astron. Soc. 8.
Škoda, P., Draper, P.W., Neves, M.C., et al., 2014. Spectroscopic analysis in the virtual observatory environment with SPLAT-VO. Astron. Comput. 7.
Stothers, R.B., 2010. Giant convection cell turnover as an explanation of the long secondary periods in semiregular red variable stars. Astrophys. J. 725 (1).
Strassmeier, K.G., Granzer, T., Weber, M., et al., 2004. The STELLA robotic observatory. Astron. Nachr. 325 (6), 527–532.
Uitenbroek, H., Dupree, A.K., Gilliland, R.L., 1998. Spatially resolved hubble space telescope spectra of the chromosphere of alpha orionis. Astron. J. 116 (5).
van Loon, J. Th., 2012. Betelgeuse and the red supergiants. In: EAS Publications Series. Vol. 60.
Vernet, J., Dekker, H., D'Odorico, S., Kaper, L., et al., 2011. X-shooter, the new wide band intermediate resolution spectrograph at the ESO Very Large Telescope. Astron. Astrophys. 536.
Weber, M., Granzer, T., Strassmeier, K.G., 2012. The STELLA robotic observatory on tenerife, software and cyberinfrastructure for astronomy II. Proc. SPIE 8451, 84510K.
Wood, P.R., 2000. Variable red giants in the LMC: Pulsating stars and binaries? Publ. Astron. Soc. Aust. 17 (1).
Wood, B.E., Müller, H.R., Harper, G.M., 2016. Hubble space telescope constraints on the winds and astrospheres of red giant stars. Astrophys. J. 829 (2).
Wood, P.R., Olivier, E.A., Kawaler, S.D., 2004. Long secondary periods in pulsating asymptotic giant branch stars: An investigation of their origin. Astrophys. J. 604 (2).

Appendix B

Astronomy & Astrophysics manuscript no. output
May 16, 2023

The Great Dimming of Betelgeuse: the photosphere as revealed by tomography during the past 15 years

Daniel Jadlovský[1,2], Thomas Granzer[2], Michael Weber[2], Kateryna Kravchenko[3], Jiří Krtička[1], Andrea K. Dupree[4], Andrea Chiavassa[5], Klaus G. Strassmeier[2], and Katja Poppenhäger[2]

[1] Department of Theoretical Physics and Astrophysics, Faculty of Science, Masaryk University, Kotlářská 2, Brno, 611 37, Czech Republic
e-mail: jadlovsky@mail.muni.cz
[2] Leibniz-Institut für Astrophysik Potsdam (AIP), An der Sternwarte 16, D-14482 Postdam, Germany
[3] Max Planck Institute for Extraterrestrial Physics, Giessenbachstrasse 1, D-85748, Garching, Germany
[4] Center for Astrophysics | Harvard & Smithsonian, 60 Garden Street, MS-15, Cambridge, MA, 02138, USA
[5] Université Côte d'Azur, Observatoire de la Côte d'Azur, CNRS, Lagrange, CS 34229, 06304 Nice Cedex 4, France

in preparation

ABSTRACT

Context. Betelgeuse, a red supergiant star of semi-regular variability, underwent a historical minimum of brightness in February 2020, the Great Dimming. Even though the brightness has returned to the values prior to the Great Dimming by now, it continues to exhibit highly unusual behavior.
Aims. Understanding the long-term atmospheric motions of Betelgeuse and its variability could be a clue to the nature of the Great Dimming and the mass-loss process in red supergiants. Our goal is to study long-term dynamics of the photosphere, including during the Great Dimming.
Methods. We applied a tomographic method, which allows probing different layers in the stellar atmosphere, to reconstruct depth-dependent velocity fields. The method is based on constructing spectral masks by grouping spectral lines from specific optical depths. These masks are cross-correlated with the observed spectra to recover the velocity field inside each atmospheric layer.
Results. We obtained about 2500 spectra during the past 15 years, observed with the STELLA robotic telescope in Tenerife. We were able to analyse the variability of five different layers of Betelgeuse's photosphere. We found phase shift between the layers, as well as between the variability of velocity and photometry. The time variations of the widths of the cross-correlation function reveal propagation of two shock waves during the Great Dimming. For about 2 years after the Dimming, the time scale of variability was different in inner and outer photospheric layers. By 2022, all the layers seemingly started to follow a similar behavior as before the Dimming, but pulsating with the first overtone.
Conclusions. Combination of the extensive high-resolution spectroscopic dataset with the tomographic method revealed the variable velocity fields in the photosphere of Betelgeuse, for the first time in such a detail. We were also able to find new insights related to the Great Dimming event.

Key words. Betelgeuse – The Great Dimming – red supergiants – tomography – shock waves – techniques: spectroscopic, photometric

1. Introduction

Betelgeuse (α Orionis) is a nearby red supergiant (RSG) star. Its semi-regular variability is characterized by two main timescales common to many RSGs, a shorter period of roughly 400 days, attributed to the radial pulsations of the atmosphere in the fundamental mode (FM) (Kiss et al. 2006; Chatys et al. 2019; Joyce et al. 2020; Jadlovský et al. 2023) and a longer period of about 2100 days (5.6 years), of less certain origin. The longer period is attributed either to the flow timescales of giant convective cells (Stothers 2010), which López Ariste et al. (2022) found some evidence for through spectropolarimetry imaging. It could also be attributed to processes that drive a similar mode of variability in AGB stars, where it is known as Long Secondary Period (LSP), most likely caused by non-radial low-degree oscillations due to gravity modes, but other mechanisms were also proposed, e.g., magnetic activity (Wood 2000; Wood et al. 2004). In many RSGs, Kiss et al. (2006); Chatys et al. (2019) also found higher overtones of the fundamental mode, primarily the first overtone. Joyce et al. (2020) also detected a photometric period of about 185 days in Betelgeuse, which is likely the first overtone mode. Granzer et al. (2022) found a period of about 216 days based on radial velocities as well as evidence for the second overtone. However, for all the modes of variability, the length and amplitude of each cycle is not constant (Kiss et al. 2006).

Betelgeuse underwent an unprecedented historical minimum of brightness, the so-called Great Dimming, that culminated in February 2020 when its brightness dropped by $V \sim 1.6$ mag (Guinan et al. 2020). The interferometric observations by Montargès et al. (2021) revealed that the star dimmed asymmetrically, as the southern hemisphere of Betelgeuse was much darker than its northern counterpart. Many theories have been put forward to explain the Great Dimming, such as significant decrease in temperature or formation of star spots (Dharmawardena et al. 2020), a surface mass loss event (Dupree et al. 2020, 2022), an increase of molecular opacity (Kravchenko et al. 2021) or a dust

clump above the photosphere (Montargès et al. 2021; Cannon et al. 2023).

In the detailed study combining the previous findings, Dupree et al. (2022) suggested that the Great Dimming was caused by a shock wave, reported by Kravchenko et al. (2021), that formed in the photosphere and resulted in substantial surface mass ejection of matter by the September-Novemeber of 2019. The ejected material reached the outer atmosphere in about 6 months, eventually creating the molecules and dust as it reached cooler regions. Dupree et al. (2022) also observed that following the Great Dimming, the star pulsated with shorter periods than 400 days.

Based on new models by Davies & Plez (2021), which successfully incorporated stellar wind and, for the first time, reproduced extended atmospheres and related observed spectral features of red supergiants, they generally support the scenario proposed by Dupree et al. (2022), although they show that the Dimming can be explained by TiO molecules absorption, without the need for dust condensation in the ejected material. Harper et al. (2020) also showed that the Dimming could be explained by a decrease of temperature and no additional dust was required.

In the present paper, we intend to reveal long-term atmospheric motions of Betelgeuse and its variability by applying the tomographic method by Alvarez et al. (2001a); Kravchenko et al. (2018) to time-eries of high-resolution spectra of Betelgeuse. In the following sections, we first describe our data set and then the application of the tomographic method to it. Afterwards, we present the results and discuss the shocks, higher overtones and the Great Dimming event, followed by the conclusions.

2. Observations and Methodology

2.1. Observations

We employ echelle spectra observed with the STELLA echelle spectrograph (SES) mounted on the robotic 1.2 m STELLA-II telescope at the Izanã Observatory in Tenerife, operated by AIP (Strassmeier et al. 2004, 2010). The resolving power is $R \approx 55\,000$ with a 3-pixel sampling per resolution element. The spectra have signal-to-noise ratios (S/N) of 100 − 600. Exposure times range from 5 to 20 seconds. The spectra cover the wavelength range 390−880 nm. To this date, the full time series of Betelgeuse unprecedentedly consists of about 2450 spectra (4500 exposures in total) obtained during the years 2008–2023, that is, spanning nearly 15 years. Most of these observations were originally presented by Granzer et al. (2021, 2022), where the telescope, observations and methodology is also briefly described.

The data were reduced using the IRAF-based pipeline SESDR in its version 4.0 (Weber et al. 2008, 2012). All spectra were corrected for echelle blaze and were wavelength calibrated with consecutively recorded Th-Ar spectra. The radial velocity (RV) of each stellar spectrum was derived using 62 of the 82 echelle orders. In order to improve the RV results, some wavelength regions with weak S/N (e.g., the order edges) were excluded, as well as some regions containing very strong lines (e.g., the Balmer lines and telluric line regions in the red parts of the spectrum).

2.2. Methodology

2.2.1. Envelope tomography

The tomographic method was first introduced by Alvarez et al. (2000, 2001a). The method allows us to probe different layers in the stellar atmosphere and recover the corresponding velocity fields. That is accomplished by sorting spectral lines into groups (masks) based on their formation depth. The masks are cross-correlated with observed or synthetic stellar spectra and provide velocity fields within different atmospheric layers.

Cross-correlation (CCF) functions of some Mira-type stars appear double-peaked during the maximum brightness (Alvarez et al. 2000). One of the main goals of using the tomographic method was to show this feature can be explained by passing of shock waves through the atmosphere, called Schwarzschild scenario (Schwarzschild 1952), i.e., the second peak would correspond to the rising shock front. Alvarez et al. (2000, 2001a,b) successfully applied the method and recovered Schwarzschild scenario on spatial and temporal scales in several Mira-type stars. The only limitation of the method was that it assumed the line depression originates in layers where optical depth τ is 2/3. But that was shown to not be the case for weak lines (Albrow & Cottrell 1996). It was also difficult to make quantitative predictions as the geometric radius associated with each mask was not known.

Kravchenko et al. (2018) improved the method by including the computation of the contribution function to calculate the formation depth of spectral lines. The method was then validated on a 3D radiative-hydrodynamics simulation of a RSG atmosphere. Kravchenko et al. (2019) applied the tomographic method to high-resolution spectroscopic time-series observations of a RSG star μ Cep to interpret its photometric variability. Finally, Kravchenko et al. (2020) validated the tomographic method on spectro-interferometric VLTI/AMBER observations by recovering a link between optical and geometrical depth scales, based on comparison to dynamical model atmospheres.

Afterwards, Kravchenko et al. (2021) also applied the tomographic method to high-resolution spectroscopic time-series observations of Betelgeuse taken with HERMES spectrograph during years 2015-2020 to interpret its photometric variability, including the Great Dimming event. The resolution of HERMES is 86 000, which is larger than resolution of STELLA, and their dataset included about 30 spectra. They found two shock waves preceding the Dimming (in February 2018 and January 2019), the latter one amplifying the former one. They proposed that succession of these two shocks resulted in an outflow (as shown by velocity gradients) and an increase of molecular opacities as interpretation of the Dimming. They did not rule out the dust scenario, but could not confirm it based on spectroscopic observations.

To apply the tomographic method in this paper, we used a spectral template ($T_{\rm eff}$ = 3500 K, $\log g = 0$, $v_{\rm microturb} = 2\,{\rm km\,s^{-1}}$ and solar metallicity) calculated with the Turbospectrum synthesis code (Plez 2012) with MARCS models (Gustafsson et al. 2008) and VALD3 atomic and molecular line lists (Ryabchikova et al. 2015). Furthermore, to be able to analyse different layers of Betelgeuse's photosphere, we used the line lists from Kravchenko et al. (2021) to create the tomographic masks, based on our template. Therefore, for each of the 5 groups in the line list, the original template for Betelgeuse was modified to include only the lines from one of the groups in the list, i.e, we created 5 new templates with selected lines. This was achieved by removing all the lines from the template that were not included in the

Table 1. Lists of spectral lines from Kravchenko et al. (2019) used in each mask and numbers of spectra, which were left from the original dataset after successful cross-correlations and subsequent cleaning.

Mask	$\log \tau_0$ limits	N. of lines	N. of spectra
C1	$-1.0 < \log \tau_0 \leq 0.0$	419	1111
C2	$-2.0 < \log \tau_0 \leq -1.0$	1750	1489
C3	$-3.0 < \log \tau_0 \leq -2.0$	1199	1541
C4	$-4.0 < \log \tau_0 \leq -3.0$	433	1549
C5	$-4.6 < \log \tau_0 \leq -4.0$	378	1524

masks (for each mask). This is done unlike in Kravchenko et al. (2021), who used Dirac distribution as line profiles.

Table 1 lists the masks used in this paper. Lines in mask C1 have the highest optical depths, while each following mask has lower values of optical depths than the one before it, all relative to a reference optical depth τ_0 computed at 5000 Å, as described in Kravchenko et al. (2018). Therefore, mask C1 corresponds to the innermost layer of the probed photosphere and mask C5 corresponds to the outermost layer.

2.2.2. Cross-correlation functions

To derive cross-correlation functions (CCFs), the radial velocity determination is done order-by-order, i.e., each echelle order is cross-correlated with the mask separately. Afterwards, the cross-correlation functions are summed up and the radial velocity is determined by a gaussian fit (for a single observation). From the fit, we also extract parameters of the peak.

Amongst other reasons, the order-by-order approach turned out to be very useful for determining radial velocity with mask C1, because the quality of signal was low when using all 62 orders. That is likely due to the fact that many lines in this mask are weak, while many of the lines are also farther in the red region, where the telluric lines contamination was an issue for some orders. To obtain the most precise results of radial velocity for C1, we had to leave most of orders unused, except 2 orders (733.4-754.8 nm), as otherwise the results were quite noisy. For the other 4 masks, 62 echelle orders were used as normally. However, to plot CCFs of mask 1 we used all 62 orders again (Figs. 1 and A.1), in order to be able to analyse all lines contributing to an atmospheric layer.

Many of the spectra were removed due to failed guiding of the telescope or other various instrument related issues. Only spectra with signal-to-noise ratio higher than 100 were used (higher than 25 for the interval from mid 2011 to the last major maintenance in 2014). And finally, only results of radial velocity with error lower than 0.05km s^{-1} were used (except for masks C1 and C5, where the error limits were 0.1 km s^{-1} and 0.07 km s^{-1}, respectively). The numbers of spectra left after the cleaning are listed in Table 1.

The spectrograph underwent following maintenance, which affected quality of the data: exchange of the camera (23 December 2011), new cross-disperser (4 June 2012) and lastly, introduction of beam-splitter (7 June 2014).

3. Results

The results are plotted in two Figs. 2 and 3, each covering approximately one LSP cycle (hereafter referred to as first and second LSP cycles, respectively). Figure A.1 in Appendix shows the monthly averages of CCFs for each mask, while Fig. 1 shows a preview of CCFs during the most interesting part of the data. This section is focused on characterizing the overall variability of the star in our dataset. The Great Dimming (and what has followed it) as well as other discussion is described specifically in the next section.

3.1. Brightness

The first panels of Figs. 2 and 3 show evolution of brightness adopted from AAVSO, SMEI (Jackson et al. 2004; Hick et al. 2007), BRITE (Pigulski 2018) and Ogane Hikari Observatory (Ogane et al. 2022). The first two datasets consists of more data than plotted in the figures. For SMEI and BRITE, cleaning algorithm as described in Paunzen et al. (2021); Jadlovský et al. (2023) was applied. The combination of these datasets covers well the photometric variability of the star, including the Great Dimming.

We also label photometric cycles in the panels, based on times between two (major) photometric minima. These cycles are intended solely for plotting hysteresis loops in Sect. 3.6 rather than trying to precisely define a physical cycle of the star, which would be very difficult given the complex variability.

3.2. Relative temperature changes

Line-depth ratio of V I (6251.83 Å) and Fe I (6252.57 Å) is sensitive to temperature changes due to its excitation potentials, therefore, it can be used as a proxy for temperature. The ratio becomes larger for decreasing temperature in the photosphere (Gray 2008). Calibration of these ratios to absolute values of temperature would be problematic, however the relative variability of temperature is sufficient for us, as we primarily use it for plotting hysteresis loops in Sect. 3.6.

The ratios are plotted alongside the brightness in the upper panel of Figs. 2 and 3.

3.3. Radial velocities

The second panels of the Figs. 2 and 3 reveal kinematics of different layers of photosphere, using 5 cross-correlation masks from Table 1, representing 5 different layers of photosphere. Due to the great abundance of observations, we are able to see the long-term evolution of different layers of Betelgeuse, for the first time in such a detail. The zero-point is set at 20.7 km s^{-1} corresponding to center-of-mass (CoM) of Betelgeuse (the average value between Harper et al. (2017) and Kervella et al. (2018)).

In the majority of times, the radial curves follow a scenario that we would expect. When a rising material starts to propagate through the photosphere, the innermost layer (C1) is the first one to be affected. It starts to increase its velocity as the layer is moving outwards. The innermost layer seems to always be the first layer to reach its local maximum of velocity, but the time delays between the layers are considerably smaller than during the minima (all line shifts between individual radial velocity curves are estimated just approximately). The values of velocity during the maxima are quite similar to each other for most masks, except mask C5. The outermost layer C5 usually has the lowest velocity compared to other layers during maxima (between years 2009 and 2012 it is also rather surprisingly accompanied by layer C1). Whereas, during the minima, the different layers are considerably easier to distinguish, as the differences in time shifts and velocity amplitudes are greater. But for both cases, the

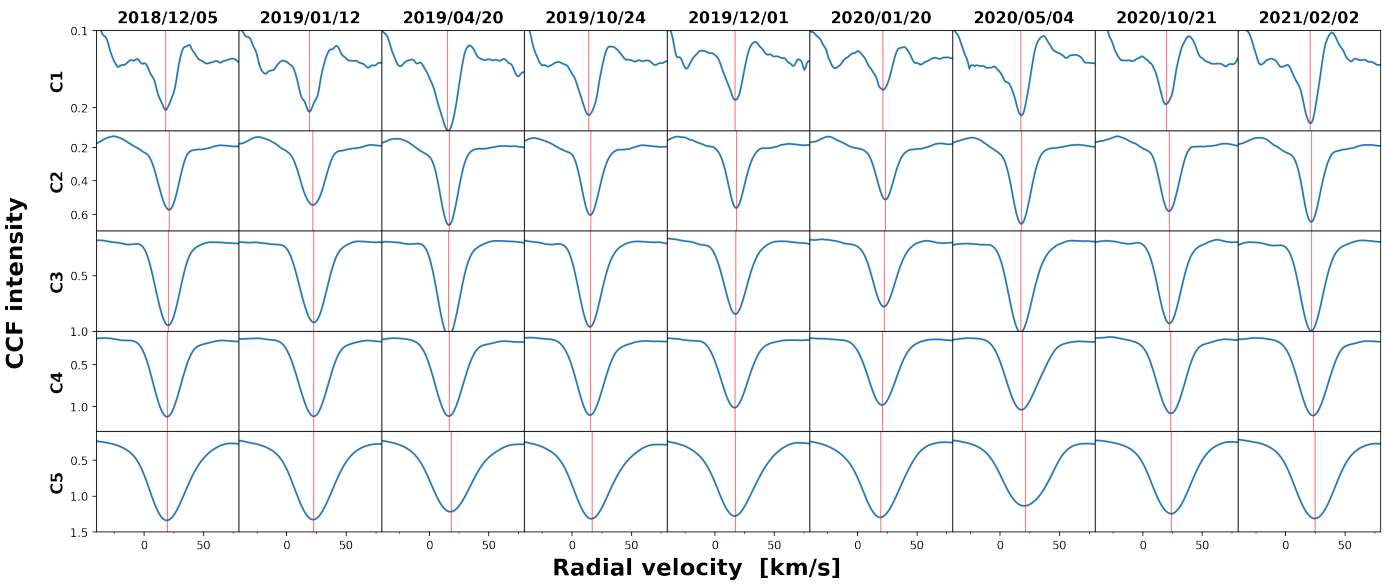

Fig. 1. A preview of the CCFs, sampled during cycles related to the Dimming. Vertical red lines show peaks of the CCFs. In CCFs of mask C1 we can often clearly see that the central peaks are asymmetric, suggesting a secondary component. Masks C2, possibly also C3, sometimes also appear slightly asymmetric. All the CCFs from the data are plotted in Fig. A.1.

minima and maxima, there are some cycles when the overall differences are much lower (such as during the first LSP cycle in Fig. 2), likely proportionally to the local amplitude of velocity.

While the minima of velocity of innermost layer C1 usually appear in nearly the same time as the minima of brightness V, each following layer is more delayed. The time shift of velocity minima between the innermost and outermost layer can be up to about 50 d (10 d between neighboring layers), which is quite common in the second LSP cycle (Fig. 3), especially so during and after the Great Dimming. However, during the first LSP cycle (Fig. 2), the time shifts are almost negligible, only up to about 10 d. Nonetheless, we have less minima covered by the data in this time period.

The maxima caused by the FM period (about 400 d) usually have values of about 5 km s^{-1} (estimated), relative to the previous minimum (following values of maxima in the article are given in the same manner). Sometimes there can be smaller maxima of shorter periods in range of $1 - 3$ km s^{-1}. All these modes of variability are also modulated by the LSP period, which has a similar amplitude as the FM period.

The shorter periods of variability, i.e., likely the higher overtones of the fundamental mode, seem to appear more frequently (and significantly) when the velocity due to the LSP cycle reaches a minimum, i.e., when the velocities are below the velocity of CoM of the star for several cycles of the FM period. This is shown in 2 during 2008-2010 and in 3 during 2020-2023.

3.4. Velocity gradients

The third panels of Figs. 2 and 3 show curves of velocity gradients, i.e., the evolution of velocities relative to the outermost layer C5. The gradients are calculated in the same manner as in Kravchenko et al. (2021), i.e., we defined gradients for layers C1-C4 as $v_{C_5} - v_{C_i}$, where $i = 1, 2, 3, 4$. Thus, when the gradients are negative ($v_{C_5} - v_{C_i} < 0$), they signify expansion of regions over which the gradient was taken, whereas when the gradients are positive ($v_{C_5} - v_{C_i} > 0$), they signify contraction.

The gradients are quite small in most times (typically positive), within 2 km s^{-1} from the zero point, and quite often even at the zero point. In other words, during most times all the layers are moving with nearly the same velocity, such as between the years 2014 and 2017, or they are being slightly contracted (due to data sampling, we are simply likely missing the instances, when the layers are being slightly expanded).

In cycles when the velocity variability is stronger, the gradients reveal to us that when the material is rising, the inner layers of the photosphere are typically being contracted (primarily C1-C3, C4 usually considerably less so). On the other hand, when the material in the layers is in-falling, all the layers usually move with a similar velocity. We can see a significant expansion or contraction of the atmospheric layers only rarely.

3.5. CCF widths

The bottom panel of Figs. 2 and 3 shows the widths of CCFs. Figure A.1 in Appendix shows all CCFs for all masks, in form of monthly averages, while Fig. 1 shows a preview of single CCFs.

When a shock wave is passing through an atmosphere, a secondary component representing the rising material would appear in CCF (as described in Sect. 2.2.1), causing the function to appear asymmetric and increasing its width. Nonetheless, some other processes can also affect the shape of a line, such as convective motions (Josselin & Plez 2007). Kravchenko et al. (2021) reported secondary components of CCF maxima shifted by $10 - 15$ km s^{-1}. Through spectropolarimetry, López Ariste et al. (2018, 2022) report even higher velocities, about 40 km s^{-1}, which is much higher than adiabatic estimates, and in some cases the velocity of rising plasma can reach up to about 60 km s^{-1}.

In general, shapes of our CCFs appear similar to those by Kravchenko et al. (2021) and we have also found many asymmetries in shapes of CCFs of mask 1, suggesting similar motions as they described. A sample of CCFs is plotted in Fig. 1.

Regardless, we find the width of CCF to be a reliable indicator of a passing shock wave. We can see an unprecedented increase in CCF widths in the beginning of 2019 (Fig. 3), followed by an even stronger increase a year later, in the beginning of 2020. Meanwhile, in the rest of the data, the variability of the CCF widths is considerably smaller. Therefore this makes

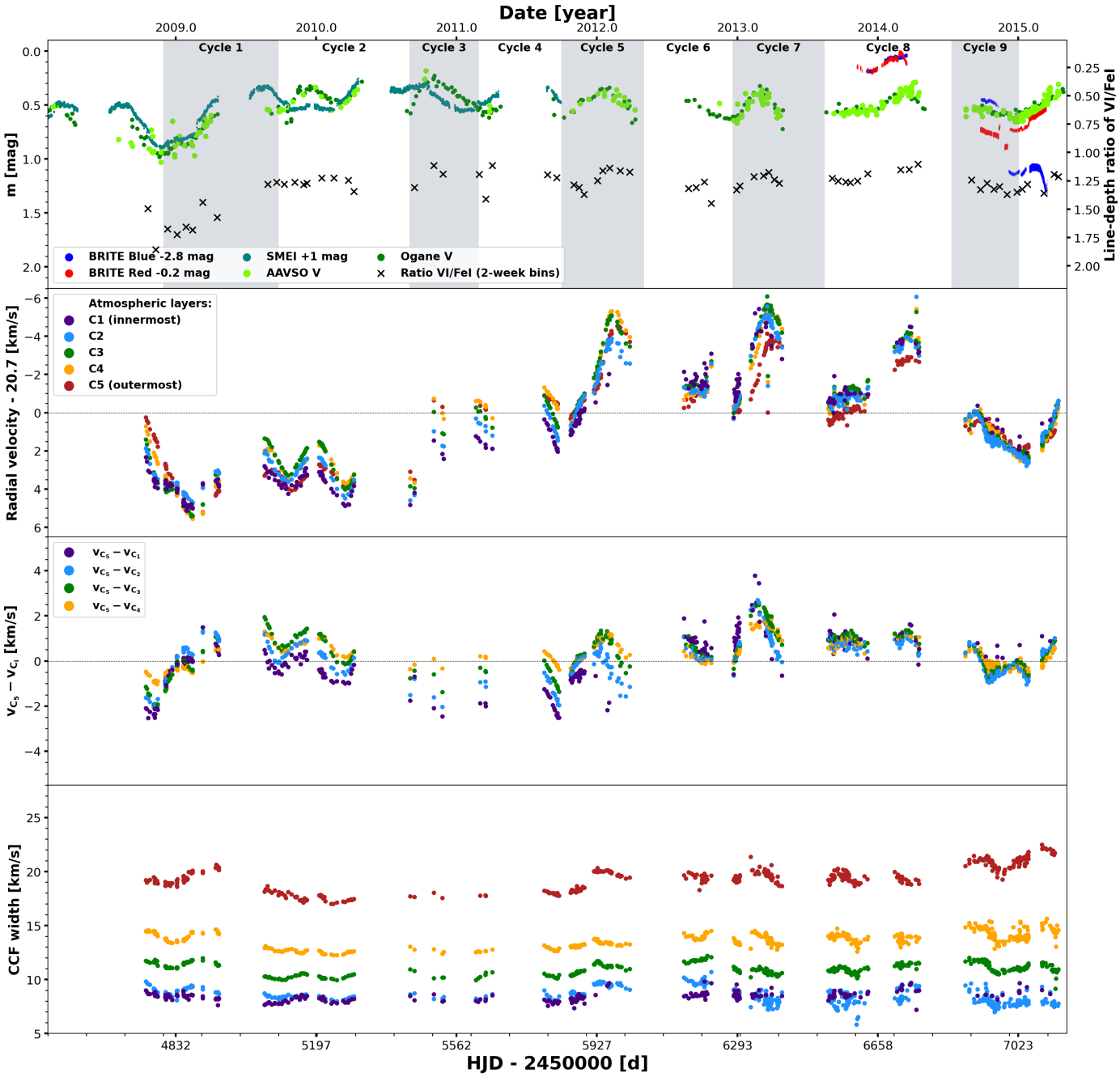

Fig. 2. First LSP cycle (2008-2015) *First panel:* Light curve, comprising of data from AAVSO, BRITE, Ogane and SMEI. Temperature is also included via the line-depth ratio. *Second panel:* Radial velocity plot determined from STELLA spectra. The spectra were cross correlated with 5 different masks, corresponding to 5 different layers of photosphere. The same color coding is applied in the 4th panel. The velocity of the center-of-mass (20.7 km s^{-1}) was subtracted. We can see the presence of higher overtones of the FM period between years 2009 and 2010. *Third panel:* Gradients of the radial velocity from masks in the second panel. We can see that at most times the gradients are not very high. *Fourth panel:* Widths of CCFs. We can see the variability is correlated with both main periods, to a certain extent.

it clear that the Great Dimming was truly an extraordinary and unprecedented event. While the first shock wave in 2019 has already been reported by Kravchenko et al. (2021), the stronger shock wave in 2020 has not yet been reported in any study.

The shock wave in 2018 reported by Kravchenko et al. (2021) does not seem to be represented in our data by any significant CCF width peak (at least not one comparable to the two main peaks), although there definitely is a small increase of CCF width in 2018. That suggests that this shock wave was of a much smaller amplitude than the two that accompanied the Dimming. Supposing this was indeed a shock of a smaller scale, then similar shocks of weaker amplitudes are quite frequent, as in Figs. 2 and 3 we can see many peaks at this variability scale.

Additionally, we also have to remark that resolution of HERMES is about 86 000, which is much higher than that of STELLA and we also did not use the same CCF computation process, therefore that may be the cause of several differences in shapes of our CCFs.

For both shock waves we can see a time shift of the emergence of a shock wave in a similar manner as we can see in the

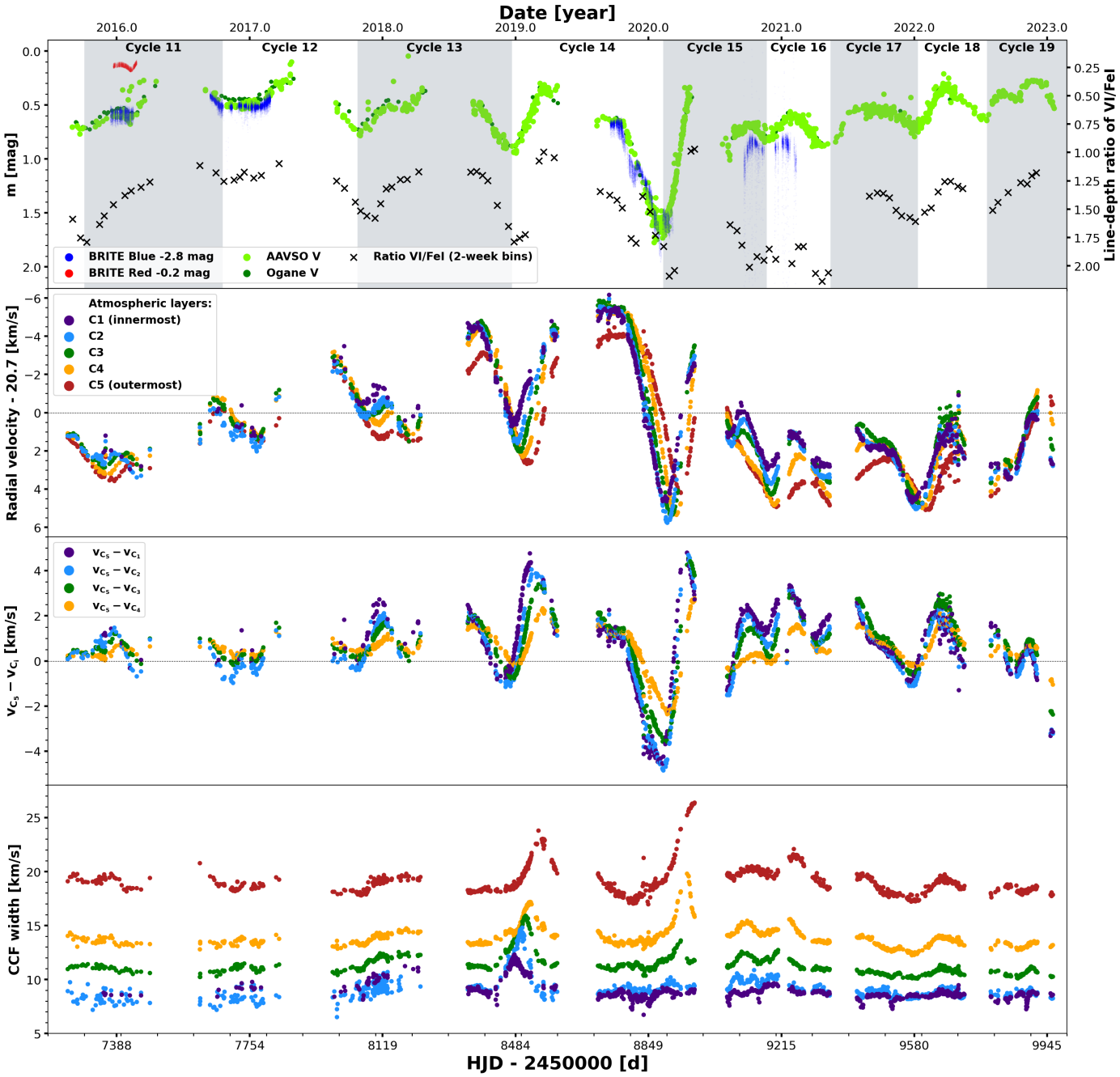

Fig. 3. Same as Fig. 2, but for the second LSP cycle (2015-2023). *Second panel: Third panel:* During the Great Dimming the gradients were uniquely negative, suggesting a strong expansion of the inner layers. *Fourth panel:* There are two significant peaks in the CCFs widths before and during the Dimming, while the latter peak was much stronger. Both peaks are caused by a passing shock wave.

RVs, i.e., the shock wave is moving from the innermost mask to the uppermost mask. However, there are some differences between the shock waves in 2019 and 2020. During the first shock wave the CCF width peak of the innermost mask arises in a similar time as in RVs and the peaks of outer masks are increasingly more delayed, most significantly for mask C5. In total, the time shift between C1 and C5 is about 75 d. Likewise, we can see a similar time effect during the shock wave in 2020, even though the CCF width peaks are larger in outermost masks, compared to the previous shock wave, while in the innermost masks (C1 and C2) the peaks are barely visible at all.

3.6. Hysteresis loops

As shown in Gray (2008), during a regular pulsation cycle the material starts heating (for a beginning of a cycle defined in last temperature minimum), while the velocity is constant. Eventually, once the temperature is high enough, the material starts to rise up in the atmosphere. When the material is rising it begins to cool and hence it starts to in-fall again after some time.

We constructed hysteresis loops, i.e., evolution of velocity and temperature, for Betelgeuse and it indeed shows that such a behavior can generally be observed in many of the cycles, even though the exact shapes and amplitudes of each loop are often quite different from each other. The results are available in Figs.

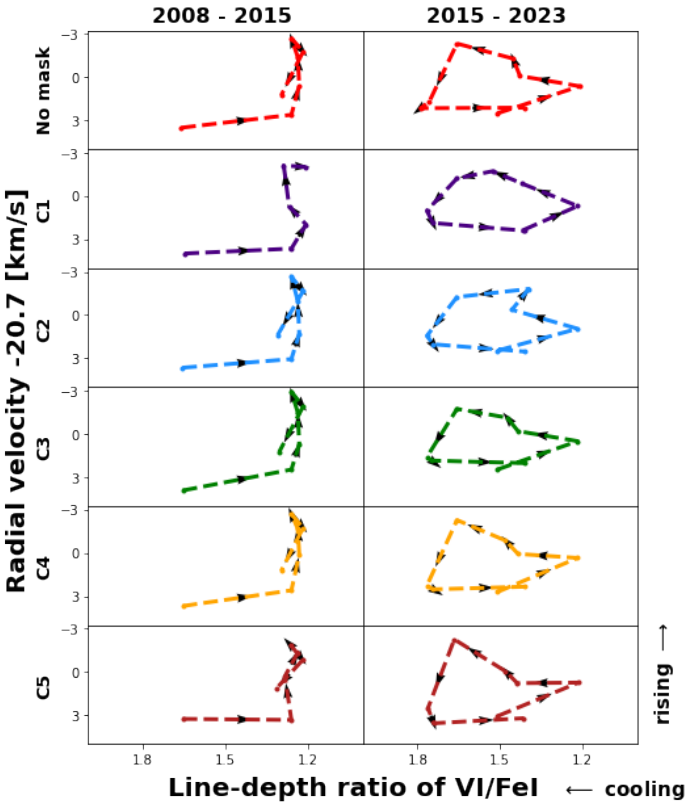

Fig. 4. Hysteresis loops for approximate LSP cycles and plotted for different layers of the photosphere. The values were binned in 250-d intervals. The shape of the loop of the first cycle (left panels) may be affected by data sampling, as during this period, we usually had data only during the rising of hot material. But nonetheless, the first cycle also shows that material is returning to its starting position, except in layer C1.

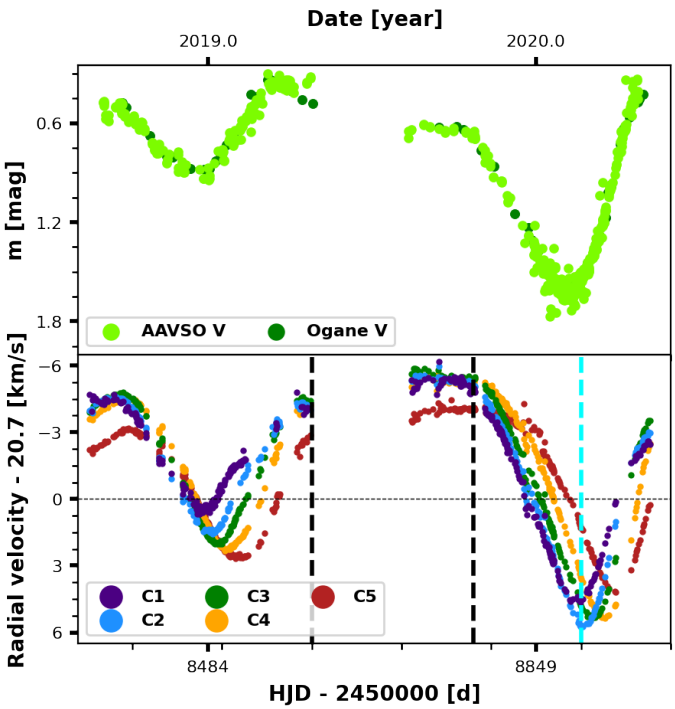

Fig. 5. Detailed look on the Great Dimming from Fig. 3. The first shock emerged in the beginning of 2019. Shortly after, the layers start to rise, orderly one by one, driven by the shock. The black vertical lines denote the unusual outflow that lasted nearly 200, which is quite unprecedented in the data, as normally the maxima are very short. During this outflow the ejection of material as proposed by Dupree et al. (2022) could easily happen. This outflow, or rather the shock, changed the mode of pulsations, as also reported by Granzer et al. (2022). What followed were extreme in-falling velocities, leading to an expansion of the atmospheric layers (as shown in Fig. 3), while the minima of inner layers were deeper than those of upper layers, which is also unprecedented in the data.

B.1, B.2, and B.3 in appendix. In cases when it is not possible to clearly determine the shape of a loop, it is usually due to the lack of data (significantly in older cycles). Data sampling also plays a significant role, especially so in the first half of the data, where the loops usually display only the part when the hot material was rising. Additionally, the determination of cycles (based on photometric minima) is not very precise due to the complex variability of the star.

Notwithstanding all these issues, it is quite apparent from the data that the oscillations shorter than the FM period rarely form full hysteresis loops. Usually the curves seem to cover about a half of a loop. On the other hand, the FM cycles seem to form full loops.

Furthermore, in Fig. 4 we show the evolution of velocity and temperature for the LSP cycle. Quite surprisingly, the material in the photosphere also quite clearly forms hysteresis loops, superimposed over the shorter loops. These longer loops could correspond to the turnover of material in giant convection cells on the surface.

4. Great Dimming

We revealed several unique features that appeared during the Great Dimming (a closer look in Fig. 5). Firstly, there was the powerful shock wave, which first appeared in the innermost layer C1 in the beginning of 2019 and then continued to propagate upwards. Simultaneously, it caused a strong outflow of rising material (or enhanced it) that reached its maximum by the middle of 2019, with an amplitude of about 7 km s^{-1} in some masks. Although the velocity during the peak was quite similar to some of the preceding maxima, what made this outflow special was that the velocity stayed at near maximum values for a very long time (other velocity maxima in the data are quite narrow), lasting nearly 200 d (between the dashed black lines in Fig. 5), probably extended by the passing shock wave. Furthermore, the gradients show the inner layers were mildly contracted, due to the material rising from the interior of the star. This is when material of higher density would be ejected from the atmosphere as reported by Dupree et al. (2020, 2022). During this peak, the velocity of the outermost layer C5 was lower compared to inner layers by about 1.5 km s^{-1} (it is typically lower during almost all velocity peaks). Granzer et al. (2022) reports the FM was already being excited to higher overtones during this.

What followed was a massive decrease of velocity, when the velocity of layers C1-C4 quite abruptly changed by about 10 km s^{-1}, while for layer C5 by about 8 km s^{-1}. When the inner layers started to fall down, the layer C5 was still rising up. Most importantly, the velocities of inner layers were in-falling much faster and stronger than the layer C5, causing the inner layers to expand dramatically, turning the gradients the lowest (and negative) in all the data. When the minimum velocity was reached by the April 2020, the inner layers, especially C2-C4, abnormally had a deeper minimum of velocity than layer C5 (cyan line in

Fig. 5). However, as usually the innermost layer C1 was still the first to reach the minimum, orderly followed by the upper layers.

In summary, the brightness reached its historical minimum in February 2020 (Guinan et al. 2020), followed by minima of photospheric velocities in April 2020 (Granzer et al. 2021) and then also by a maximum velocity of outflowing wind during the end of spring (Jadlovský et al. 2023). Meanwhile, the brightness of Betelgeuse quickly begun to restore its normal values. Regardless, the events that followed the Dimming have continued to be unprecedented as well.

4.1. Aftermath

The moment the innermost layers reached its minima of velocity during the Great Dimming (cyan line in Fig. 5), a rather small peak appeared in the widths of C1-C2 CCFs, possibly being the origin of next shock wave, which was even stronger than the first one (based on CCF widths behavior). By the time mask C5 reached its minimum of velocity, the shock wave already appeared to be passing through mask C3, but the height of the CCFs widths peak was still smaller than in the same mask during the previous shock wave. Simultaneously, the layers were starting to contract itself again. By the time the velocities of all layers were rising again, the shock wave passed through layers C4 and C5. In these two layers, the shock wave was much stronger than the previous one, and the strongest in the entire dataset.

Either way, the resulting outflow seems to have the highest velocity in the data. The amplitude of the peak cannot be determined precisely, as the peak happened some time during the summer 2020, which was not covered by our observations. Fortunately, the photometric data by Taniguchi et al. (2022) reveal that the maximum of brightness was reached approximately the moment our data coverage ends just before the beginning of summer 2020. Thus, the maximum velocity was probably reached by the middle of summer gap, which suggests that by that time the rising material was able to reach quite high values of velocity, at the very least comparable to the outflow that preceded the Dimming. The passing shock wave appears to reach its maximum of velocity in layer C5 in the same time the data coverage ends (it already had its maxima in the other layers). The outflow could have reached up to 10 km s^{-1} for masks C1-C4. The gradients were the highest observed, i.e., the shock wave caused an extreme contraction of layers C1-C3 (the largest in the data once again). It seems this velocity maximum followed about 250 d after the previous one, thus the FM pulsations were indeed likely already excited to higher overtones.

This extreme outflow leads to a remarkable divergence of the inner (C1-C3) and outer (C4-C5) layers of the atmosphere, which is is shown in detailed look in Fig. 6. The outer layers continued their previous movement (red lines in 6), while the inner layers were oscillating with shorter modes of variability of 100 – 200 d (additional minima for inner layers shown as blue lines in Fig. 6), likely first or some other low-order overtones. This unprecedented dissonance continued for about a year and half. By 2022, all the layers of the photopshere were finally synchronized again, however this time following the shorter mode of pulsations. As we can see during the minimum of velocity in the beginning of 2022, the layers seem to indeed behave similarly to each other again, in the same way as before the Dimming, although now pulsating with the shorter mode of variability of about 200 d (Dupree et al. 2022; Jadlovský et al. 2023; Granzer et al. 2022), which very likely is the first overtone. The LSP of about 2100 d appears to remain active, but whether the FM period regains its dominance is to be seen. Based on the previous behavior of the star it seems likely that the FM shall indeed return.

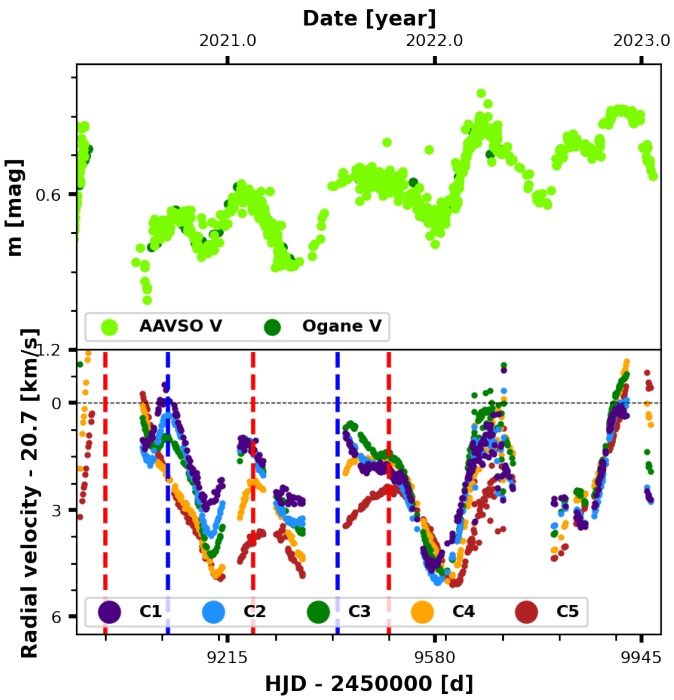

Fig. 6. A detailed look on the aftermath of the Dimming from Fig. 3. The blue vertical lines indicate approximate times of velocity minima for the inner layers, while the red vertical lines denote the maxima shared for all layers (or also the maxima of outer layers). The outer layers continued their movement unaffected, apparently still following the FM of pulsations, while the inner layers were likely already excited to higher overtones. Following the last red vertical line, the layers appear more synchronized with each other again, but the dominant mode of pulsations is now the first overtone.

After the outflow in summer 2020 the velocity gradients returned to similar values as before the Dimming. However, since the beginning of 2023, the gradients have been nearly as low as during the Dimming (and in the entire dataset), suggesting that the inner layers are being significantly expanded. Therefore, another major event might be underway.

5. Discussion

5.1. Shock waves

The lines considered here come from higher up in the photosphere where the optical depth is smaller than one. In these layers of RSGs the photospheric activity is characterized by interactions between non-radial pulsations and shock waves (Chiavassa et al. 2010). The shock waves originate from sounds waves produced in stellar interior by convection. As the wave hits the surface, it is slowed down and compressed due to the drop in temperature and sound speed. It increases its amplitude due to the decrease in density and thus turns into a shock, propagating to the outer atmosphere (Freytag et al. 2017; Liljegren et al. 2017; Kravchenko et al. 2019). The density and pressure scale heights are lower in outer layers, which causes the shock waves to become even stronger, accompanied by larger pressure fluctuations. Consequently, the influence on the photosphere would also become more significant (Chiavassa et al. 2011). As we can

see in the Fig. 3, the shock waves indeed become stronger as they reach the upper layers.

Alvarez et al. (2000) showed that Mira-type stars clearly follow the Schwarzschild scenario, revealing the upward motion of the shock front, whereas Josselin & Plez (2007); Kravchenko et al. (2019) showed it is not clearly seen from the CCFs profiles of RSGs, as in these stars the motions within the atmosphere are more complex. Similarly, as we can seen in our data, even during the Dimming event there is no obvious hint of Schwarzschild scenario in Betelgeuse and rather than visible line-doubling events we just observe asymmetries, which may be due to resolution. Nonetheless, our CCFs width data shows that two powerful shock waves appeared in Betelgeuse before and after the Dimming, while the first one is likely responsible for the Dimming itself.

5.2. Excitation and damping of higher overtones

As we shown in Sect. 3, the higher overtones of the FM period are not observed only after the Dimming, but occasionally even before, in similar times like observed in brightness, usually most significantly during the minima of LSP cycle when the velocities are long-term in-falling, as is shown in Fig. 7. Furthermore, as it appears from the hysteresis loops, the higher overtones do not form full hysteresis loops.

A minimum of radial velocity should follow approximately a quarter of phase after the minimum radius (for a usual radial oscillator). Therefore, it appears that oscillations of higher overtones are being excited during or shortly after the maximum contraction of a star, i.e. the minimum radius. Afterwards, as the overall radius increases, these higher overtones seems to be damped by the FM oscillation which dominates and the movement of material is driven by this mode (based on the hysteresis loops).

This perhaps suggests that different processes from beneath the photosphere are able to excite the motion of photospheric material to higher overtones, when the material is long-term contracted. Or rather, as Joyce et al. (2020) proposes, a non-linear excitation may occur, i.e., the layers would eventually accumulate enough energy and momentum to compress the material beneath the photosphere. The compressed material would heat and thus impact convective structure near the surface, altering the energy flow beneath the surface.

Possibly, assuming the strength of the two shocks during the Dimming is not that unique, the shocks could provide the source of additional energy or heat that dissipates into the atmosphere. As Granzer et al. (2022) shows, the mode of pulsations begun to change shortly before the Dimming, in a similar time as the first powerful shock wave emerges in our data (Fig.3), while after the second shock wave the change of pulsations became even more apparent. However, the first LSP cycle (Fig.2) does not show any such a powerful shock wave. Although it is not impossible that such a shock may have occurred in a time gap in the data, or before the STELLA data collection begun.

6. Conclusions

Thanks to the enormous dataset of spectral observations by STELLA-SES combined with the tomographic method, we were able to analyse the long-term evolution of different layers of Betelgeuse's photosphere in an unprecedented detail, revealing many insights into the variability of the RSG photospheres, pulsations, formation of shock waves, its passing through the photosphere and a correlation of different layers of photosphere with the brightness variability and properties of CCFs.

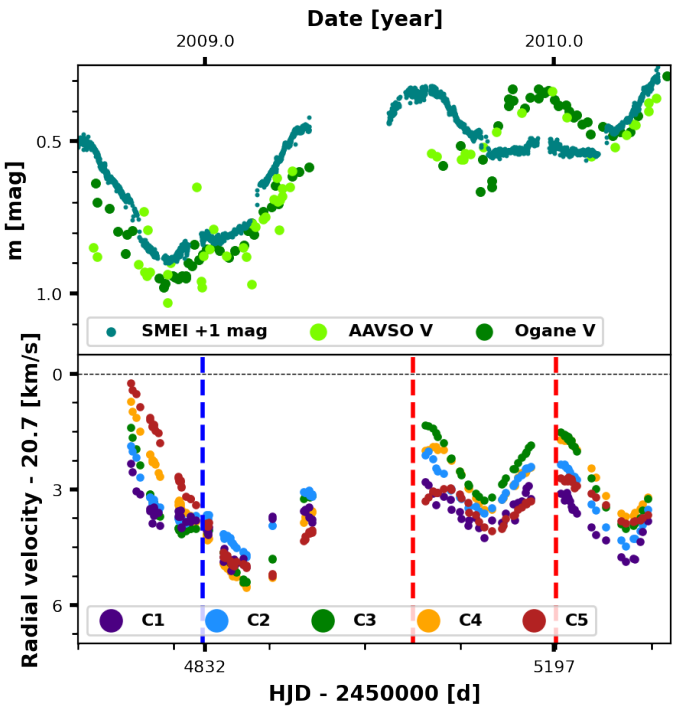

Fig. 7. Detail from Fig. 2 showing a presence of low-order overtones long ago before the Dimming, during a minimum due to LSP cycle. The red broken lines denote the estimated times of maxima, which are delayed only by about 150 days from each other. The behavior of the atmospheric layers also slightly resembles the aftermath of Dimming (Fig. 6), as the velocities are more interwoven than usually. The blue line denotes a possible small local maximum of velocity of inner layers, while the two outermost masks appear to not have a local maximum of velocity. If we had more data, we could see for how long the low-order overtones remained prominent.

Typically, the innermost layer reaches its minimum of velocity approximately in the same moment the star reaches its minimum of brightness (in filter V at least). The outer layers follow with a time shift, reaching up to 50 days for the outermost layer (but usually it is less), while the minima of velocity are slightly deeper for each mask that follows. For shock waves, the time shifts seem to be longer, up to 75 days until it reaches the outermost layer, while the shock is increasing its strength as it is rising. During the maxima of velocity, the situation is quite different. The time shifts of velocity maxima between the atmospheric layers are much smaller, nearly negligible in some cycles, while the values of velocity peaks are typically quite similar for all masks except the outermost one, which is usually considerably lower compared to the inner layers. The gradients show that when the material is rising the inner layers of the photosphere are typically being contracted, whereas when the material is in-falling, all the layers usually move with a similar velocity.

Similarly as in Granzer et al. (2022), we find that the photospheric velocity is indeed variable on two primary timescales, the LSP of about 2100 d and FM of about 400 d, while during some cycles the low-order overtones become considerably more significant, especially after the Dimming. The low-order overtones seem to be more prominent when the atmospheric velocities are long-term in-falling due to the LSP cycle, during or following the minimum overall radius of the star. This possibly

suggests that the mode of pulsations may be excited to higher overtones by processes that take place deeper in the atmosphere.

The hysteresis loops indicate that the motion of material is primarily being driven by the pulsations due to the FM period, while the oscillations of higher overtones appear to fail to form complete loops, which may be a clue for why the higher overtones are being damped. Curiously, the LSP also appear to form a hysteresis loop. This could be used as evidence that LSP period is indeed due to motion of material in giant convection cells.

We revealed two powerful shock waves related to the Great Dimming. The first one (reported by Kravchenko et al. (2021)) likely is the major progenitor of the Dimming, causing a major long-lasting outflow of material (Granzer et al. 2021; Dupree et al. 2022), while the second shock wave emerged after the Dimming and contributed to the changes of the atmosphere. The outflow caused by the first shock wave was followed by an extreme decrease of velocity of all layers, while the inner layers were in-falling faster than the outermost layer, uniquely causing the inner layers to expand. By the end of this minimum of velocity a second shock wave emerged, being even more powerful than the first, at least in the outer layers. The second shock wave lead to another extreme velocity of rising material in the atmosphere, possibly the highest in the data, while in turn it caused an extreme contraction of the atmospheric layers. These events resulted into major changes to the structure of the atmosphere. However, these changes did not take effect in all the layers in the same time. For about a year and half, the pulsation mode of inner layers was already excited to the first overtone, or some other low-order overtone, while outer layers remained less affected, continuing their previous movement with the FM of pulsations, until the dissonance ended by the beginning of 2022. Two years after the Dimming, the rearrangement of the photosphere appeared complete. Based on the previous behavior of the star, we expect the FM will eventually regain its dominance. Furthermore, since the beginning of 2023 the inner layers are being extremely expanded again, nearly as much as during the Dimming, suggesting that we might be on a precipice of another unprecedented event.

Similarly as Kravchenko et al. (2021), we were not able to clearly recover Schwarzchild scenario in the spectra of Betelgeuse, but instead there are many asymmetries in shapes of CCFs, caused by convective motions or passing shock waves. Nonetheless, we conclude that the width of CCFs is a reliable indicator for detecting strong shocks. Using the widths, we were able to reveal two powerful shock waves during the Dimming, which are clearly quite unprecedented in Betelgeuse (based on the rest of our data). The CCF widths also show variability of a smaller scale, which could be related to shocks of lower amplitudes or convective motions.

This study further validates the potential of the tomographic method. Most importantly, it reveals many new major insights into the nature of RSGs. We intend to follow up on these results in upcoming papers, where will compare the results to 3D radiative-hydrodynamics simulations.

Acknowledgements. Based on data obtained with the STELLA robotic telescopes in Tenerife, an AIP facility jointly operated by AIP and IAC. Based on data collected by the BRITE Constellation satellite mission, designed, built, launched, operated and supported by the Austrian Research Promotion Agency (FFG), the University of Vienna, the Technical University of Graz, the University of Innsbruck, the Canadian Space Agency (CSA), the University of Toronto Institute for Aerospace Studies (UTIAS), the Foundation for Polish Science and Technology (FNiTP MNiSW), and National Science Centre (NCN). KP acknowledges funding from the German *Leibniz Community* under project P67/2018. AC acknowledges support from the French National Research Agency (ANR) funded project PEPPER (ANR-20-CE31-0002)

References

Albrow, M. D. & Cottrell, P. L. 1996, MNRAS, 278, 337
Alvarez, R., Jorissen, A., Plez, B., Gillet, D., & Fokin, A. 2000, A&A, 362, 655
Alvarez, R., Jorissen, A., Plez, B., et al. 2001a, A&A, 379, 288
Alvarez, R., Jorissen, A., Plez, B., et al. 2001b, A&A, 379, 305
Cannon, E., Montargès, M., de Koter, A., et al. 2023, arXiv e-prints, arXiv:2303.08892
Chatys, F. W., Bedding, T. R., Murphy, S. J., et al. 2019, MNRAS, 487, 4832
Chiavassa, A., Freytag, B., Masseron, T., & Plez, B. 2011, A&A, 535, A22
Chiavassa, A., Haubois, X., Young, J. S., et al. 2010, A&A, 515, A12
Davies, B. & Plez, B. 2021, MNRAS, 508, 5757
Dharmawardena, T. E., Mairs, S., Scicluna, P., et al. 2020, ApJ, 897, L9
Dupree, A. K., Strassmeier, K. G., Calderwood, T., et al. 2022, ApJ, 936, 18
Dupree, A. K., Strassmeier, K. G., Matthews, L. D., et al. 2020, ApJ, 899, 68
Freytag, B., Liljegren, S., & Höfner, S. 2017, A&A, 600, A137
Granzer, T., Weber, M., Strassmeier, K. G., & Dupree, A. 2021, in The 20.5th Cambridge Workshop on Cool Stars, Stellar Systems, and the Sun (CS20.5), Cambridge Workshop on Cool Stars, Stellar Systems, and the Sun, 41
Granzer, T., Weber, M., Strassmeier, K. G., & Dupree, A. 2022, in Cambridge Workshop on Cool Stars, Stellar Systems, and the Sun, Cambridge Workshop on Cool Stars, Stellar Systems, and the Sun, 185
Gray, D. F. 2008, AJ, 135, 1450
Guinan, E., Wasatonic, R., Calderwood, T., & Carona, D. 2020, The Astronomer's Telegram, 13512, 1
Gustafsson, B., Edvardsson, B., Eriksson, K., et al. 2008, A&A, 486, 951
Harper, G. M., DeWitt, C., Richter, M. J., et al. 2017, ApJ, 836, 22
Harper, G. M., Guinan, E. F., Wasatonic, R., & Ryde, N. 2020, ApJ, 905, 34
Hick, P., Buffington, A., & Jackson, B. V. 2007, in Society of Photo-Optical Instrumentation Engineers (SPIE) Conference Series, Vol. 6689, Solar Physics and Space Weather Instrumentation II, ed. S. Fineschi & R. A. Viereck, 66890C
Jackson, B., Buffington, A., Hick, P., et al. 2004, Solar Physics, 225, 177
Jadlovský, D., Krtička, J., Paunzen, E., & Štefl, V. 2023, New Astronomy, 99, 101962
Josselin, E. & Plez, B. 2007, A&A, 469, 671
Joyce, M., Leung, S.-C., Molnár, L., et al. 2020, ApJ, 902, 63
Kervella, P., Decin, L., Richards, A. M. S., et al. 2018, A&A, 609, A67
Kiss, L. L., Szabó, G. M., & Bedding, T. R. 2006, MNRAS, 372, 1721
Kravchenko, K., Chiavassa, A., Van Eck, S., et al. 2019, A&A, 632, A28
Kravchenko, K., Jorissen, A., Van Eck, S., et al. 2021, A&A, 650, L17
Kravchenko, K., Van Eck, S., Chiavassa, A., et al. 2018, A&A, 610, A29
Kravchenko, K., Wittkowski, M., Jorissen, A., et al. 2020, A&A, 642, A235
Liljegren, S., Höfner, S., Eriksson, K., & Nowotny, W. 2017, A&A, 606, A6
López Ariste, A., Georgiev, S., Mathias, P., et al. 2022, A&A, 661, A91
López Ariste, A., Mathias, P., Tessore, B., et al. 2018, A&A, 620, A199
Montargès, M., Cannon, E., Lagadec, E., et al. 2021, Nature, 594, 365
Ogane, Y., Ohshima, O., Taniguchi, D., & Takanashi, N. 2022, Open European Journal on Variable Stars, 233, 1
Paunzen, E., Supíková, J., Bernhard, K., Hümmerich, S., & Prišegen, M. 2021, MNRAS, 504, 3758
Pigulski, A. 2018, in 3rd BRITE Science Conference, ed. G. A. Wade, D. Baade, J. A. Guzik, & R. Smolec, Vol. 8, 175–192
Plez, B. 2012, Turbospectrum: Code for spectral synthesis, Astrophysics Source Code Library, record ascl:1205.004
Ryabchikova, T., Piskunov, N., Kurucz, R. L., et al. 2015, Phys. Scr, 90, 054005
Schwarzschild, M. 1952, in Shock waves in the atmospheres of pulsating stars, Vol. 8 (Cambridge University Press), 811–812
Stothers, R. B. 2010, ApJ, 725, 1170
Strassmeier, K. G., Granzer, T., Weber, M., et al. 2004, Astronomische Nachrichten, 325, 527
Strassmeier, K. G., Granzer, T., Weber, M., et al. 2010, Advances in Astronomy, 2010, 970306
Taniguchi, D., Yamazaki, K., & Uno, S. 2022, Nature Astronomy, 6, 930
Weber, M., Granzer, T., & Strassmeier, K. G. 2012, in Society of Photo-Optical Instrumentation Engineers (SPIE) Conference Series, Vol. 8451, Software and Cyberinfrastructure for Astronomy II, ed. N. M. Radziwill & G. Chiozzi, 84510K
Weber, M., Granzer, T., Strassmeier, K. G., & Woche, M. 2008, in Society of Photo-Optical Instrumentation Engineers (SPIE) Conference Series, Vol. 7019, Advanced Software and Control for Astronomy II, ed. A. Bridger & N. M. Radziwill, 70190L
Wood, P. R. 2000, PASA, 17, 18
Wood, P. R., Olivier, E. A., & Kawaler, S. D. 2004, ApJ, 604, 800

Appendix A: Cross-correlation Functions

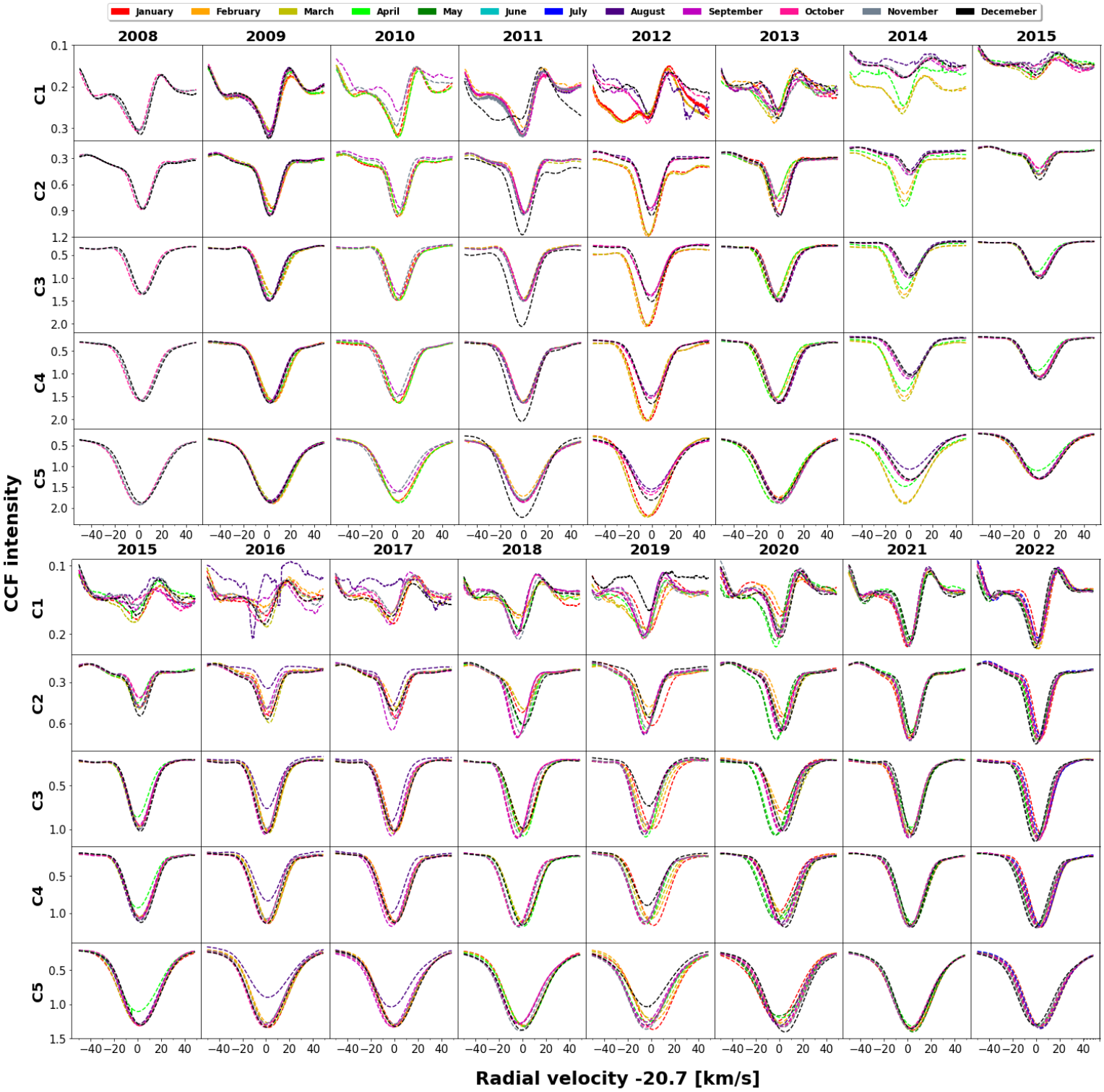

Fig. A.1. Monthly averages of CCFs. Only the CCFs of mask 1 show significant changes to the peak profile. The difference in CCF intensities between the first and second half of the data is caused by the instrument changes described in Sect. 2.

Appendix B: Hysteresis Loops

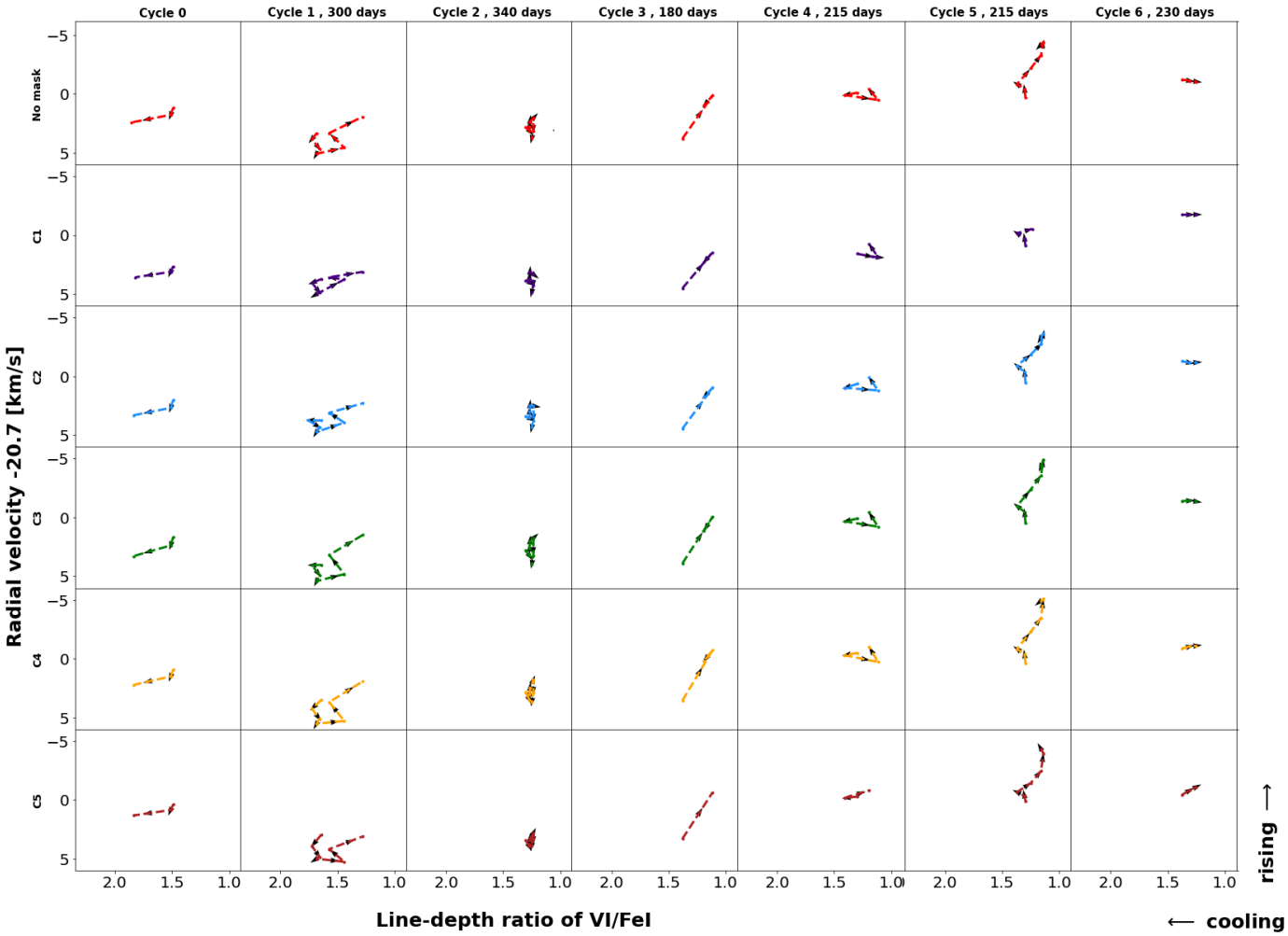

Fig. B.1. Hysteresis loops for photometric cycles shown in Figs. 2 and 3. In order to more clearly demonstrate the evolution of material in atmospheric layers, the values were binned in 2-week intervals. Most cycles lack significant parts of the loops due to not enough measurements (especially in the first half of the data) and summer gaps. Continued in Fig. B.2. The black arrows indicate the direction of a loop, which almost always is as we would expect, i.e., a loop from right to left.

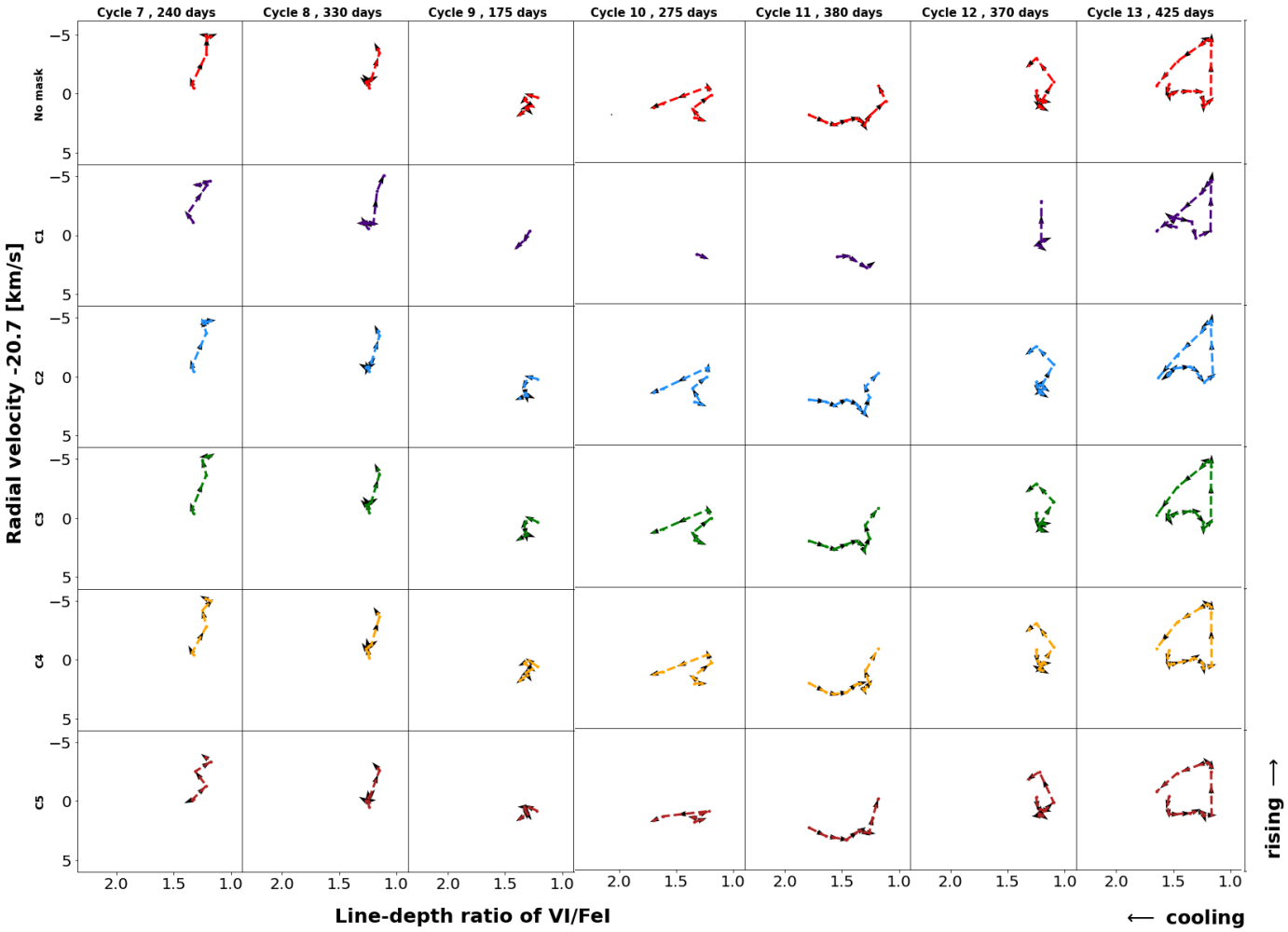

Fig. B.2. Hysteresis loops for photometric cycles, continuing from Fig. B.1.

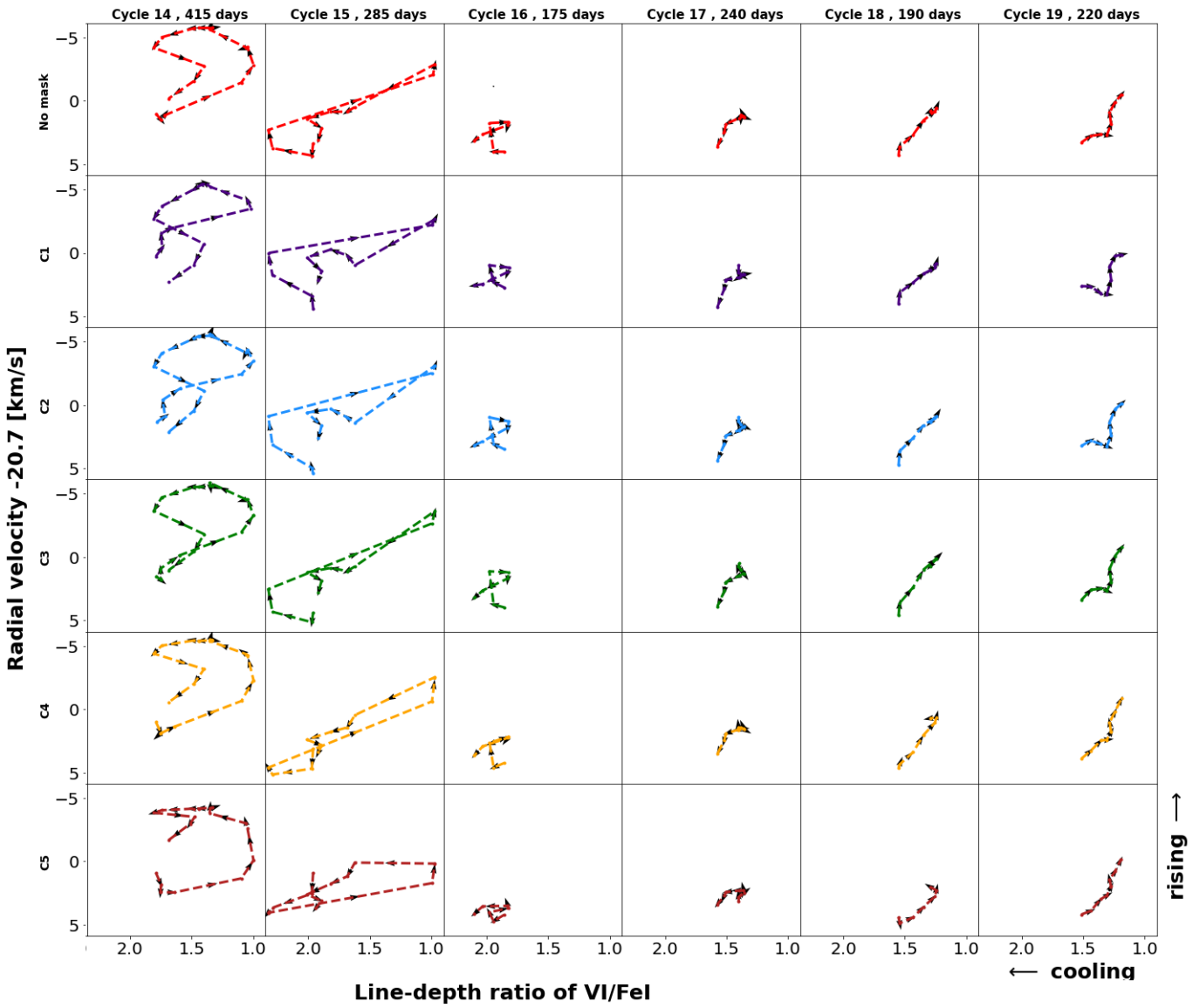

Fig. B.3. Hysteresis loops for photometric cycles, continuing from Fig. B.2.

Bibliography

Agrawal, P., Stevenson, S., Szécsi, D., & Hurley, J. 2022, A systematic study of super-Eddington layers in the envelopes of massive stars, A&A, 668, A90

Albrow, M. D. & Cottrell, P. L. 1996, Contribution functions and the depths of formation of spectral lines in Cepheids, MNRAS, 278, 337

Allende Prieto, C. 2007, Velocities from Cross-Correlation: A Guide for Self-Improvement, AJ, 134, 1843

Alvarez, R., Jorissen, A., Plez, B., Gillet, D., & Fokin, A. 2000, Envelope tomography of long-period variable stars. I. The Schwarzschild mechanism and the Balmer emission lines, A&A, 362, 655

Alvarez, R., Jorissen, A., Plez, B., et al. 2001a, Envelope tomography of long-period variable stars II. Method, A&A, 379, 288

Alvarez, R., Jorissen, A., Plez, B., et al. 2001b, Envelope tomography of long-period variable stars III. Line-doubling frequency among Mira stars, A&A, 379, 305

Alvarez, R. & Plez, B. 1998, Near-infrared narrow-band photometry of M-giant and Mira stars: models meet observations, A&A, 330, 1109

Arroyo-Torres, B., Wittkowski, M., Chiavassa, A., et al. 2015, What causes the large extensions of red supergiant atmospheres?. Comparisons of interferometric observations with 1D hydrostatic, 3D convection, and 1D pulsating model atmospheres, A&A, 575, A50

Arroyo-Torres, B., Wittkowski, M., Marcaide, J. M., & Hauschildt, P. H. 2013, The atmospheric structure and fundamental parameters of the red supergiants AH Scorpii, UY Scuti, and KW Sagittarii, A&A, 554, A76

Ayres, T. R. 2014, in Astronomical Society of India Conference Series, Vol. 11, Astronomical Society of India Conference Series, 1

Bedding, T. R. 2003, Solar-like Oscillations in Semiregular Variables, Ap&SS, 284, 61

Bennett, P. D. 2010, in Astronomical Society of the Pacific Conference Series, Vol. 425, Hot and Cool: Bridging Gaps in Massive Star Evolution, ed. C. Leitherer, P. D. Bennett, P. W. Morris, & J. T. Van Loon, 181

Böhm-Vitense, E. 1958, Über die Wasserstoffkonvektionszone in Sternen verschiedener Effektivtemperaturen und Leuchtkräfte. Mit 5 Textabbildungen, ZAp, 46, 108

Cannon, E., Montargès, M., de Koter, A., et al. 2021, The inner circumstellar dust of the red supergiant Antares as seen with VLT/SPHERE/ZIMPOL, MNRAS, 502, 369

Cardelli, J. A., Clayton, G. C., & Mathis, J. S. 1989, The Relationship between Infrared, Optical, and Ultraviolet Extinction, ApJ, 345, 245

Chatys, F. W., Bedding, T. R., Murphy, S. J., et al. 2019, The period-luminosity relation of red supergiants with Gaia DR2, MNRAS, 487, 4832

Chiavassa, A. & Freytag, B. 2015, in Astronomical Society of the Pacific Conference Series, Vol. 497, Why Galaxies Care about AGB Stars III: A Closer Look in Space and Time, ed. F. Kerschbaum, R. F. Wing, & J. Hron, 11

Chiavassa, A., Freytag, B., Masseron, T., & Plez, B. 2011, Radiative hydrodynamics simulations of red supergiant stars. IV. Gray versus non-gray opacities, A&A, 535, A22

Chiavassa, A., Haubois, X., Young, J. S., et al. 2010, Radiative hydrodynamics simulations of red supergiant stars. II. Simulations of convection on Betelgeuse match interferometric observations, A&A, 515, A12

Chiavassa, A., Kravchenko, K., Montargès, M., et al. 2022, The extended atmosphere and circumstellar environment of the cool evolved star VX Sagittarii as seen by MATISSE, A&A, 658, A185

Chiavassa, A., Plez, B., Josselin, E., & Freytag, B. 2009, Radiative hydrodynamics simulations of red supergiant stars. I. interpretation of interferometric observations, A&A, 506, 1351

Climent, J. B., Wittkowski, M., Chiavassa, A., et al. 2020, VLTI-PIONIER imaging of the red supergiant V602 Carinae, A&A, 635, A160

Danchi, W. C., Bester, M., Degiacomi, C. G., Greenhill, L. J., & Townes, C. H. 1994, Characteristics of dust shells around 13 late-type stars., AJ, 107, 1469

Davies, B. & Plez, B. 2021, The impact of winds on the spectral appearance of red supergiants, MNRAS, 508, 5757

de Jager, C. 1984, The stability limit of hypergiant photospheres., A&A, 138, 246

de Jager, C., Nieuwenhuijzen, H., & van der Hucht, K. A. 1988, Mass loss rates in the Hertzsprung-Russell diagram., A&AS, 72, 259

Dolan, M. M., Mathews, G. J., Lam, D. D., et al. 2016, Evolutionary Tracks for Betelgeuse, ApJ, 819, 7

Dupree, A. K., Strassmeier, K. G., Calderwood, T., et al. 2022, The Great Dimming of Betelgeuse: A Surface Mass Ejection and Its Consequences, ApJ, 936, 18

Dupree, A. K., Strassmeier, K. G., Matthews, L. D., et al. 2020, Spatially Resolved Ultraviolet Spectroscopy of the Great Dimming of Betelgeuse, ApJ, 899, 68

Ekström, S., Georgy, C., Eggenberger, P., et al. 2012, Grids of stellar models with rotation. I. Models from 0.8 to 120 $M_\odot$ at solar metallicity (Z = 0.014), A&A, 537, A146

Ekström, S., Meynet, G., Georgy, C., et al. 2020, in Stars and their Variability Observed from Space, ed. C. Neiner, W. W. Weiss, D. Baade, R. E. Griffin, C. C. Lovekin, & A. F. J. Moffat, 223–228

Elias, J. H., Frogel, J. A., & Humphreys, R. M. 1985, M supergiants in the Milky Way and the Magellanic Clouds :colors, spectral types, and luminosities., ApJS, 57, 91

Freytag, B. & Höfner, S. 2023, Global 3D radiation-hydrodynamical models of AGB stars with dust-driven winds, A&A, 669, A155

Freytag, B., Liljegren, S., & Höfner, S. 2017, Global 3D radiation-hydrodynamics models of AGB stars. Effects of convection and radial pulsations on atmospheric structures, A&A, 600, A137

Freytag, B., Steffen, M., & Dorch, B. 2002, Spots on the surface of Betelgeuse – Results from new 3D stellar convection models, Astronomische Nachrichten, 323, 213

Gail, H.-P., Tamanai, A., Pucci, A., & Dohmen, R. 2020, Non-stoichiometric amorphous magnesium-iron silicates in circumstellar dust shells. Dust growth in outflows from supergiants, A&A, 644, A139

Gilman, R. C. 1969, On the Composition of Circumstellar Grains, ApJ, 155, L185

González-Torà, G., Wittkowski, M., Davies, B., Plez, B., & Kravchenko, K. 2023, The effect of winds on atmospheric layers of red supergiants. I. Modelling for interferometric observations, A&A, 669, A76

Granzer, T., Weber, M., Strassmeier, K. G., & Dupree, A. 2021, in The 20.5th Cambridge Workshop on Cool Stars, Stellar Systems, and the Sun, 41

Granzer, T., Weber, M., Strassmeier, K. G., & Dupree, A. 2022, in Cambridge Workshop on Cool Stars, Stellar Systems, and the Sun, 185

Gray, D. F. 2008, Mass Motions in the Photosphere of Betelgeuse, AJ, 135, 1450

Guo, J. H. & Li, Y. 2002, Evolution and Pulsation of Red Supergiants at Different Metallicities, ApJ, 565, 559

Gustafsson, B., Edvardsson, B., Eriksson, K., et al. 2008, A grid of MARCS model atmospheres for late-type stars. I. Methods and general properties, A&A, 486, 951

Hagen, W. 1978, Circumstellar gas and dust shells of M giants and supergiants., ApJS, 38, 1

Hagen, W., Stencel, R. E., & Dickinson, D. F. 1983, The circumstellar envelopes and chromospheres of cool giants and supergiants., ApJ, 274, 286

Haubois, X., Perrin, G., Lacour, S., et al. 2009, Imaging the spotty surface of Betelgeuse in the H band, A&A, 508, 923

Hayashi, C. & Hoshi, R. 1961, The Outer Envelope of Giant Stars with Surface Convection Zone, PASJ, 13, 442

Höfner, S. 2008, Winds of M-type AGB stars driven by micron-sized grains, A&A, 491, L1

Hubeny, I. & Mihalas, D. 2014, Theory of Stellar Atmospheres

Humphreys, R. M. 1978, Studies of luminous stars in nearby galaxies. I. Supergiants and O stars in the Milky Way., ApJS, 38, 309

Humphreys, R. M. & Davidson, K. 1979, Studies of luminous stars in nearby galaxies. III. Comments on the evolution of the most massive stars in the Milky Way and the Large Magellanic Cloud., ApJ, 232, 409

Humphreys, R. M., Davidson, K., Richards, A. M. S., et al. 2021, The Mass-loss History of the Red Hypergiant VY CMa, AJ, 161, 98

Humphreys, R. M., Helmel, G., Jones, T. J., & Gordon, M. S. 2020, Exploring the Mass-loss Histories of the Red Supergiants, AJ, 160, 145

Humphreys, R. M. & Jones, T. J. 2022, Episodic Gaseous Outflows and Mass Loss from Red Supergiants, AJ, 163, 103

Humphreys, R. M. & McElroy, D. B. 1984, The initial mass function for massive stars in the galaxy and the Magellanic clouds., ApJ, 284, 565

Hyland, A. R., Becklin, E. E., Neugebauer, G., & Wallerstein, G. 1969, Observations of the Infrared Object, VY Canis Majoris, ApJ, 158, 619

Ireland, M. J., Scholz, M., & Wood, P. R. 2008, Dynamical opacity-sampling models of Mira variables - I. Modelling description and analysis of approximations, MNRAS, 391, 1994

Ireland, M. J., Scholz, M., & Wood, P. R. 2011, Dynamical opacity-sampling models of Mira variables - II. Time-dependent atmospheric structure and observable properties of four M-type model series, MNRAS, 418, 114

Jadlovský, D. 2021, Photometric and spectroscopic characteristics of red supergiant Betelgeuse, bachelor's thesis, Masaryk University

Jadlovský, D., Krtička, J., Paunzen, E., & Štefl, V. 2023, Analysis of photometric and spectroscopic variability of red supergiant Betelgeuse, New Astronomy, 99, 101962

Johnson, H. L. 1968, The Infrared Spectrum of the NML Cygnus Object, ApJ, 154, L125

Josselin, E., Blommaert, J. A. D. L., Groenewegen, M. A. T., Omont, A., & Li, F. L. 2000, Observational investigation of mass loss of M supergiants, A&A, 357, 225

Josselin, E. & Plez, B. 2007, Atmospheric dynamics and the mass loss process in red supergiant stars, A&A, 469, 671

Joyce, M., Leung, S.-C., Molnár, L., et al. 2020, Standing on the Shoulders of Giants: New Mass and Distance Estimates for Betelgeuse through Combined Evolutionary, Asteroseismic, and Hydrodynamic Simulations with MESA, ApJ, 902, 63

Kervella, P., Decin, L., Richards, A. M. S., et al. 2018, The close circumstellar environment of Betelgeuse. V. Rotation velocity and molecular envelope properties from ALMA, A&A, 609, A67

Kervella, P., Perrin, G., Chiavassa, A., et al. 2011, The close circumstellar environment of Betelgeuse. II. Diffraction-limited spectro-imaging from 7.76 to 19.50 μm with VLT/VISIR, A&A, 531, A117

Kervella, P., Verhoelst, T., Ridgway, S. T., et al. 2009, The close circumstellar environment of Betelgeuse. Adaptive optics spectro-imaging in the near-IR with VLT/NACO, A&A, 504, 115

Kippenhahn, R., Weigert, A., & Weiss, A. 2013, Stellar Structure and Evolution

Kiss, L. L., Szabó, G. M., & Bedding, T. R. 2006, Variability in red supergiant stars: pulsations, long secondary periods and convection noise, MNRAS, 372, 1721

Kravchenko, K., Chiavassa, A., Van Eck, S., et al. 2019, Tomography of cool giant and supergiant star atmospheres. II. Signature of convection in the atmosphere of the red supergiant star μ Cep, A&A, 632, A28

Kravchenko, K., Jorissen, A., Van Eck, S., et al. 2021, Atmosphere of Betelgeuse before and during the Great Dimming event revealed by tomography, A&A, 650, L17

Kravchenko, K., Van Eck, S., Chiavassa, A., et al. 2018, Tomography of cool giant and supergiant star atmospheres. I. Validation of the method, A&A, 610, A29

Kravchenko, K., Wittkowski, M., Jorissen, A., et al. 2020, Tomography of cool giant and supergiant star atmospheres. III. Validation of the method on VLTI/AMBER observations of the Mira star S Ori, A&A, 642, A235

Lamers, H. J. G. L. M. & Cassinelli, J. P. 1999, Introduction to Stellar Winds

Lamers, H. J. G. L. M. & Levesque, E. M. 2017, Understanding Stellar Evolution

Lançon, A., Hauschildt, P. H., Ladjal, D., & Mouhcine, M. 2007, Near-IR spectra of red supergiants and giants. I. Models with solar and with mixing-induced surface abundance ratios, A&A, 468, 205

Levesque, E. M. 2010, in Astronomical Society of the Pacific Conference Series, Vol. 425, Hot and Cool: Bridging Gaps in Massive Star Evolution, ed. C. Leitherer, P. D. Bennett, P. W. Morris, & J. T. Van Loon, 103

Levesque, E. M. 2017, Astrophysics of Red Supergiants, 2514-3433 (IOP Publishing)

Levesque, E. M., Massey, P., Olsen, K. A. G., et al. 2005, The Effective Temperature Scale of Galactic Red Supergiants: Cool, but Not As Cool As We Thought, ApJ, 628, 973

Levesque, E. M., Massey, P., Olsen, K. A. G., et al. 2006, The Effective Temperatures and Physical Properties of Magellanic Cloud Red Supergiants: The Effects of Metallicity, ApJ, 645, 1102

Levesque, E. M., Massey, P., Plez, B., & Olsen, K. A. G. 2009, The Physical Properties of the Red Supergiant WOH G64: The Largest Star Known?, AJ, 137, 4744

Lion, S., Van Eck, S., Chiavassa, A., Plez, B., & Jorissen, A. 2013, in EAS Publications Series, Vol. 60, EAS Publications Series, ed. P. Kervella, T. Le Bertre, & G. Perrin, 85–92

Lobel, A. 2010, in Astronomical Society of the Pacific Conference Series, Vol. 425, Hot and Cool: Bridging Gaps in Massive Star Evolution, ed. C. Leitherer, P. D. Bennett, P. W. Morris, & J. T. Van Loon, 162

Lobel, A. & Dupree, A. K. 2000, Modeling the Variable Chromosphere of α Orionis, ApJ, 545, 454

López Ariste, A., Georgiev, S., Mathias, P., et al. 2022, Three-dimensional imaging of convective cells in the photosphere of Betelgeuse, A&A, 661, A91

López Ariste, A., Mathias, P., Tessore, B., et al. 2018, Convective cells in Betelgeuse: imaging through spectropolarimetry, A&A, 620, A199

López Ariste, A., Wavasseur, M., Mathias, P., et al. 2023, The height of convective plumes in the red supergiant μ Cep, A&A, 670, A62

Maeder, A. 2009, Physics, Formation and Evolution of Rotating Stars

Maeder, A. & Meynet, G. 1987, Grids of evolutionary models of massive stars with mass loss and overshooting - Properties of Wolf-Rayet stars sensitive to overshooting., A&A, 182, 243

Maeder, A. & Meynet, G. 2001, Stellar evolution with rotation. VII. . Low metallicity models and the blue to red supergiant ratio in the SMC, A&A, 373, 555

Magain, P. 1986, Contribution functions and the depths of formation of spectral lines, A&A, 163, 135

Massey, P. 1998, Evolved Massive Stars in the Local Group. I. Identification of Red Supergiants in NGC 6822, M31, and M33, ApJ, 501, 153

Massey, P. 2003, MASSIVE STARS IN THE LOCAL GROUP: Implications for Stellar Evolution and Star Formation, ARA&A, 41, 15

Massey, P. & Olsen, K. A. G. 2003, The Evolution of Massive Stars. I. Red Supergiants in the Magellanic Clouds, AJ, 126, 2867

Massey, P., Plez, B., Levesque, E. M., et al. 2005, The Reddening of Red Supergiants: When Smoke Gets in Your Eyes, ApJ, 634, 1286

Massey, P., Silva, D. R., Levesque, E. M., et al. 2009, Red Supergiants in the Andromeda Galaxy (M31), ApJ, 703, 420

Mauron, N. & Josselin, E. 2011, The mass-loss rates of red supergiants and the de Jager prescription, A&A, 526, A156

Meynet, G., Chomienne, V., Ekström, S., et al. 2015, Impact of mass-loss on the evolution and pre-supernova properties of red supergiants, A&A, 575, A60

Meynet, G. & Maeder, A. 2003, Stellar evolution with rotation. X. Wolf-Rayet star populations at solar metallicity, A&A, 404, 975

Meynet, G., Maeder, A., Schaller, G., Schaerer, D., & Charbonnel, C. 1994, Grids of massive stars with high mass loss rates. V. From 12 to 120 M_{sun-} at Z=0.001, 0.004, 0.008, 0.020 and 0.040, A&AS, 103, 97

Montargès, M., Cannon, E., Lagadec, E., et al. 2021, A dusty veil shading Betelgeuse during its Great Dimming, Nature, 594, 365

Nazé, Y., Che, X., Cox, N. L. J., et al. 2015, SpS5 - III. Matter ejection and feedback, Highlights of Astronomy, 16, 429

Neuhäuser, R., Torres, G., Mugrauer, M., et al. 2022, Colour evolution of Betelgeuse and Antares over two millennia, derived from historical records, as a new constraint on mass and age, MNRAS, 516, 693

Nieuwenhuijzen, H. & de Jager, C. 1990, Parametrization of stellar rates of mass loss as functions of the fundamental stellar parameters M, L, and R., A&A, 231, 134

Ohnaka, K. 2014, Imaging the outward motions of clumpy dust clouds around the red supergiant Antares with VLT/VISIR, A&A, 568, A17

Ohnaka, K., Weigelt, G., Millour, F., et al. 2011, Imaging the dynamical atmosphere of the red supergiant Betelgeuse in the CO first overtone lines with VLTI/AMBER, A&A, 529, A163

Plez, B. 2012, Turbospectrum: Code for spectral synthesis, Astrophysics Source Code Library, record ascl:1205.004

Plez, B., Brett, J. M., & Nordlund, A. 1992, Spherical opacity sampling model atmospheres for M-giants. I. Techniques,data and discussion., A&A, 256, 551

Ramachandran, V., Hamann, W. R., Oskinova, L. M., et al. 2019, Testing massive star evolution, star formation history, and feedback at low metallicity. Spectroscopic analysis of OB stars in the SMC Wing, A&A, 625, A104

Reimers, D. 1975, Circumstellar absorption lines and mass loss from red giants., Memoires of the Societe Royale des Sciences de Liege, 8, 369

Salasnich, B., Bressan, A., & Chiosi, C. 1999, Evolution of massive stars under new mass-loss rates for RSG: is the mystery of the missing blue gap solved?, A&A, 342, 131

Schaller, G., Schaerer, D., Meynet, G., & Maeder, A. 1992, New Grids of Stellar Models from 0.8-SOLAR-MASS to 120-SOLAR-MASSES at Z=0.020 and Z=0.001, A&AS, 96, 269

Schwarzschild, M. 1952, in Shock waves in the atmospheres of pulsating stars, Vol. 8 (Cambridge University Press), 811–812

Schwarzschild, M. 1975, On the scale of photospheric convection in red giants and supergiants., ApJ, 195, 137

Schwarzschild, M., Schwarzschild, B., & Adams, W. S. 1948, On the Pulsation in the Atmosphere of η Aquilae., ApJ, 108, 207

Scicluna, P., Siebenmorgen, R., Wesson, R., et al. 2015, Large dust grains in the wind of VY Canis Majoris, A&A, 584, L10

Simkin, S. M. 1974, Measurements of Velocity Dispersions and Doppler Shifts from Digitized Optical Spectra, A&A, 31, 129

Snow, Theodore P., J., Buss, Richard H., J., Gilra, D. P., & Swings, J. P. 1987, Extinction and Abundance Properties of Alpha Scorpii Circumstellar Grains, ApJ, 321, 921

Speck, A. K., Barlow, M. J., Sylvester, R. J., & Hofmeister, A. M. 2000, Dust features in the 10-mu m infrared spectra of oxygen-rich evolved stars, A&AS, 146, 437

Stencel, R. E., Pesce, J. E., & Bauer, W. H. 1989, Infrared Circumstellar Shells: Origins, and Clues to the Evolution of Massive Stars, AJ, 97, 1120

Stencel, R. E., Pesce, J. E., & Hagen Bauer, W. 1988, Far-Infrared Circumstellar "Debris" Shells of Red Supergiant Stars, AJ, 95, 141

Stothers, R. B. 2010, Giant Convection Cell Turnover as an Explanation of the Long Secondary Periods in Semiregular Red Variable Stars, ApJ, 725, 1170

Stothers, R. B. & Chin, C.-W. 1996, Evolution of Massive Stars into Luminous Blue Variables and Wolf-Rayet Stars for a Range of Metallicities: Theory versus Observation, ApJ, 468, 842

Strassmeier, K. G., Granzer, T., Weber, M., et al. 2004, The STELLA robotic observatory, Astronomische Nachrichten, 325, 527

Tessore, B., Lèbre, A., Morin, J., et al. 2017, Measuring surface magnetic fields of red supergiant stars, A&A, 603, A129

Tonry, J. & Davis, M. 1979, A survey of galaxy redshifts. I. Data reduction techniques., AJ, 84, 1511

Uitenbroek, H., Dupree, A. K., & Gilliland, R. L. 1998, Spatially Resolved Hubble Space Telescope Spectra of the Chromosphere of alpha Orionis, AJ, 116, 2501

Ulmer, A. & Fitzpatrick, E. L. 1998, Revisiting the Modified Eddington Limit for Massive Stars, ApJ, 504, 200

van Loon, J. T. 2013, in EAS Publications Series, Vol. 60, EAS Publications Series, ed. P. Kervella, T. Le Bertre, & G. Perrin, 307–316

van Loon, J. T., Cioni, M. R. L., Zijlstra, A. A., & Loup, C. 2005, An empirical formula for the mass-loss rates of dust-enshrouded red supergiants and oxygen-rich Asymptotic Giant Branch stars, A&A, 438, 273

van Loon, J. T., Marshall, J. R., Cohen, M., et al. 2006, Very Large Telescope three micron spectra of dust-enshrouded red giants in the Large Magellanic Cloud, A&A, 447, 971

Verhoelst, T., van der Zypen, N., Hony, S., et al. 2009, The dust condensation sequence in red supergiant stars, A&A, 498, 127

Wittkowski, M., Arroyo-Torres, B., Marcaide, J. M., et al. 2017, VLTI/AMBER spectro-interferometry of the late-type supergiants V766 Cen (=HR 5171 A), σ Oph, BM Sco, and HD 206859, A&A, 597, A9

Wittkowski, M., Chiavassa, A., Baron, F., et al. 2021, in The 20.5th Cambridge Workshop on Cool Stars, Stellar Systems, and the Sun (CS20.5), Cambridge Workshop on Cool Stars, Stellar Systems, and the Sun, 310

Wittkowski, M., Hauschildt, P. H., Arroyo-Torres, B., & Marcaide, J. M. 2012, Fundamental properties and atmospheric structure of the red supergiant VY Canis Majoris based on VLTI/AMBER spectro-interferometry, A&A, 540, L12

Wood, P. R. 2000, Variable Red Giants in the LMC: Pulsating Stars and Binaries?, PASA, 17, 18

Wood, P. R., Olivier, E. A., & Kawaler, S. D. 2004, Long Secondary Periods in Pulsating Asymptotic Giant Branch Stars: An Investigation of their Origin, ApJ, 604, 800